Studies on Thin Film Protonic Ceramic Fuel Cells

プロトン伝導性セラミックス薄膜燃料電池に関する研究

SeongWoo Jeong

Graduate School of Chemical Sciences and Engineering

Hokkaido University

March 2022

Table of contents

Chapter 1

General Introduction

Chapter 2

Fabrication of porous-anode-support-type fuel cells (PAFCs) with Zr-rich side $BaZr_xCe_{0.8-x}Y_{0.2}O_{3-\delta}$ electrolyte thin films

Chapter 3

Mechanism of power generation in hydrogen-permeable metal-support-type fuel cells (HMFCs): Proton pumping

Chapter 4

Enhancement of proton pumping in hydrogen-permeable metal-support-type fuel cell with highly-oxygen deficient electrolytes

Chapter 5

Development of hydrogen-permeable metal-support-type fuel cell based on Pd-alternative hydrogen permeable anode

Chapter 1

General Introduction

1.1. Climate change and required climate action

Climate change is one of the most serious and urgent issues for human society in the 21st century. Its key driver is global mean surface warming due to anthropogenic greenhouse gas (GHG) emissions such as CO_2, CH_4 and N_2O.[1] The extent of warming hinges on cumulative GHG emissions,[1] which are normally quantified as CO_2-equivalent ones ($GtCO_2$-eq) that includes non-CO_2 contributions. Over the past 800,000 years, the atmospheric concentration of CO_2 that is the major contributor to the warming fluctuated at the levels between 170 and 300 parts per million (ppm), but never exceeded 300 ppm.[2] However, they have started to gradually increase since industrial revolution in around 1750 and sharply risen over the past few decades driven largely by economic and population growth.[1] Consequently, they have reached 419 ppm as of May 2021, as reported by the National Oceanic and Atmospheric Administration,[3] which are higher than at any time in at least 2 million years.[4] Now, we are certainly facing unprecedented events. The international panel on climate change (IPCC) carefully assessed future climate changes, risk and impacts and announced in 2014 that scenarios without additional efforts to reduce GHG emissions estimate the emissions in 2100 at between about 75 $GtCO_2$-eq per year ($GtCO_2$-eq yr^{-1}) and almost 140 $GtCO_2$-eq yr^{-1}, which can induce global mean surface warming by 3.7–4.8 °C in 2100 compared with that in 1850–1900, and this increases the

likelihood of severe, pervasive and irreversible impacts for people and ecosystems through extreme climate events, ocean acidification, sea level rise, etc.[1]

To reduce climate-related risks, the 195 nations and the European Union adopted the Paris Agreement and signed the international legal document at the 2015 United Nations Climate Change Conference, namely the 21st conference of parties (COP21); the goal is to hold global temperature rise to well below 2 °C and preferably limit warming to 1.5 °C, compared to pre-industrial levels. Subsequently, the IPCC published a report in 2018, *Global warming of 1.5 °C*, which is formally approved by the world's government, and this indicated that the 1.5 °C target significantly reduces climate-related risks compared with the 2 °C one;[5] thus, it can avert severe and irreversible impacts on the most fragile ecosystems and the most vulnerable people and societies, and allows more sustainable and resilient future.[5] Thus, to attain the target, the global GHG emissions have to be reduced to 25–30 $GtCO_2$-eq by 2030, which equals a 40–50% reduction from 2010 levels (49 ± 4.5 $GtCO_2$-eq yr^{-1}), and be net zero around 2050.[5]

However, given the present situations, it is extremely hard to attain the 1.5 °C target. The global mean surface temperature has already risen by 1.09 [0.95–1.20] °C in 2011–2020 compared with that in 1850–1900.[4] In addition, the acceptable GHG emissions for the 1.5 °C target are only 420–580 $GtCO_2$-eq as from 2018[5] and they are currently being depleted at the rate of 52.4 $GtCO_2$-eq yr^{-1}, which was the annual GHG emissions in 2019.[6] Further, the world's population continues to grow. The United Nations has predicted that the global population could increase to around 8.5 billion in

2030, 9.7 billion in 2050 and 10.9 billion in 2100,[7] exacerbating GHG emissions. Indeed, the total GHG emission level is estimated to be 54.8 ± 2 $GtCO_2$-eq yr^{-1} in 2025 and 55.1 ± 3.3 $GtCO_2$-eq yr^{-1} in 2030 even if the latest international mitigation ambitions as submitted under the Paris Agreement are totally implemented.[6] If the global GHG emissions continuously increase at the present rates and thus their cumulative ones once exceed the acceptable ones, we could not restore the global mean surface temperature without negative emission technologies such as direct air capture, carbon mineralization and bioenergy with carbon capture and storage; however, their availability has not yet been demonstrated.

The majority of global GHG emissions stem from energy sectors that have been underpinning world economic growth up to now; those include electricity power generation, heat generation and transportation based on fossil fuel combustion. The energy-related GHG emissions from fossil fuel combustion and industrial processes account for about 78% of the total global GHG ones.[1] To tackle the global warming and fulfill the 1.5 °C target, it is unequivocal that we should rapidly implement a transition to decarbonization of energy use through fossil fuels phase-out.

1.2. Growing renewable energy industry and rising hydrogen economy

Renewable energy sources such as solar energy, wind power, hydropower, geothermal and bioenergy will doubtless play a central role in the decarbonized society. The costs of renewable power generation have dropped abruptly and continuously in the past decade.[8] The prices of electricity from solar photovoltaics and onshore wind power decreased by 85% and 56% for the decade from 2010 to 2020 and nowadays reached USD 0.057 kWh^{-1} and USD 0.039 kWh^{-1}, respectively, both of which are comparable or less than the price of the coal-fired electricity, USD 0.055 kWh^{-1}.[8] Therefore, solar and wind power are becoming the least-cost options and thus the default for new capacity.

Solar energy including light and heat is the most abundant in natural energy sources. The earth captures 180,000 TW of solar radiation.[9] The energy of the irradiation in one hour, which equals 648 EJ, exceeds the global total energy supply and final consumption, which were 606 EJ and 418 EJ, respectively, in 2019.[10] Therefore, solar energy is an attractive option to meet the growing energy demand. In fact, the share of renewables in global electricity generation is envisaged to be 70–86% in 2050, [5,11,12] where solar energy is a major contributor, according to the roadmaps for net zero emissions by 2050. However, there still remain a concern regarding energy security owing to their inherently energy density[13] and intermittent power generation. Since solar and wind resources are temporally and seasonally variable, the corresponding electricity gains present significant challenges to grid operators, including intermittent output and a mismatch between peak output and peak demand,[14] which can result in grid instability,[14] negative electricity prices[15] and wasteful

curtailment[16–18]. Therefore, we need a strategy to alleviate the energy security issue and reward flexibility to the world energy system together with cutting-edge technologies. Grid-scale energy storage enables further growth of these low-emissions generating sources by levelling peak load, increasing the capacity factors of wind and solar installations and transforming intermittent generators into grid-dispatchable resources.[14]

A variety of grid-scale storage technologies are available, including pumped hydro,[19] compressed air[20] and various types of battery storage[21,22]. Hydrogen is one of the rising key solutions for grid storage[23,24] because of its high energy density and low rate of self-discharge. Water electrolysis is conducted with surplus power generated from renewable energy and the 'green' hydrogen thus obtained can be used as a fuel for baseload power instead of fossil fuels, resulting in energy storage at grid scale. Green hydrogen can also be converted into more energy-dense, liquefied hydrogen-rich feedstocks based on carbon or nitrogen such as methane, alcohols, ammonia, etc. by means of industrial catalytic processes. They can be categorized to carbon-neutral fuels that can be safely delivered to all over the world, so that hydrogen has the potential to displace fossil fuels throughout energy sector.

Hydrogen is especially attractive to the sectors that have difficulty in electrification, for example cargo transportations[11,25] such as truck, shipping, and aviation and heavy industries[12,26] such as the production of cement, steel, petrochemicals and glass. These sectors will be the key to unlocking the final part of the puzzle for net zero emissions by 2050.[11] The cost of green hydrogen could be

potentially cut down to USD 1.62 kg^{-1} near future based on the current costs of solar photovoltaic and onshore wind-power in Saudi Arabia (~ USD 0.0104 kWh^{-1}), assuming that the running of alkaline electrolyzer system with the efficiency of 65% and a 15 year stack life costs as much as USD 750 kW^{-1}.[8] It might fall further as little as USD ~ 1–1.16 kg^{-1} if the running costs reach 350 kW^{-1} with the efficiency of 65–72.5% and a 15–17.5 year stack life.[8] The costs of 'blue' hydrogen — one produced by natural gas steam methane reforming with today's carbon capture, utilization and storage — are speculated to at least USD 1.45 kg^{-1}.[8] Hence, green hydrogen will be competitive with blue hydrogen in an economical point of view, so that the energy system combining renewable energy and hydrogen would be plausible as next-generation societal system. To make hydrogen economy feasible, we require reliable, cost-effective and scalable technologies for hydrogen production, storage and utilization. In this thesis, I have addressed hydrogen utilization technologies.

1.3. Hydrogen utilization technologies: Fuel cells

1.3.1. Operating principle of fuel cells

Fuel cells are core devices for hydrogen utilization, which enables highly efficient conversion of hydrogen chemical energy to electrical energy through electrochemical reactions, instead of combustion. They harness the Gibbs free energy change of the redox reactions to generate direct current electricity. They consist of three parts: Anode, electrolyte and cathode. Although reactions at electrodes are slightly different depending on pH of the electrolyte, whether it is acid or alkaline, they are essentially same. At each electrode, reactions occur in the case of acid electrolyte, as shown in **Figure 1-1**.

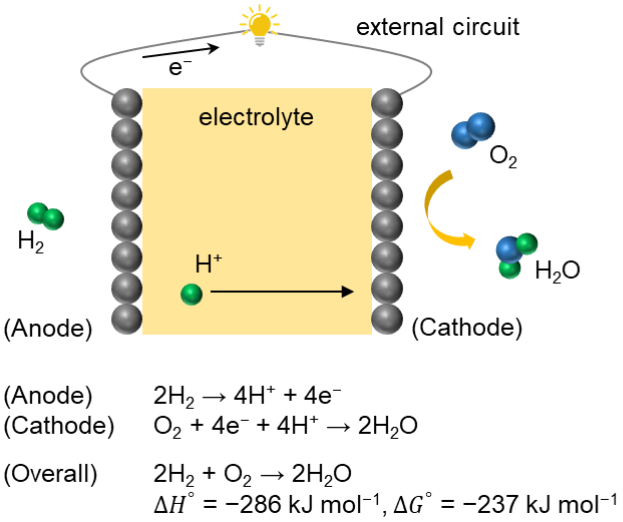

Figure 1-1. An illustration of fuel cells and their operating principle.

At the anode, fuels such as hydrogen are oxidized, so that proton and electron are generated. The proton is transported to the cathode side through the electrolyte and simultaneously the electron is delivered to the cathode along external circuit, yielding direct current electricity. At the cathode,

oxygen is reduced and resultant oxide ion reacts with the proton and the electron transferred from anode side to form water. The cathode reactions give rise to open-circuit potential of 1.23 V vs. normal hydrogen electrode at room temperature. The difference between electrode potentials works driving force to carry electron along the circuit, allowing direct transformation of the Gibbs free energy change into electrical energy. The power generation efficiency theoretically reaches as high as 83% low heating value (LHV) under standard conditions (25 °C, 10^5 Pa) because that of electrochemical process is not limited to Carnot cycle efficiency.

1.3.2. Fuel cell types and their applications

Fuel cells are called “electrochemical engines” and have the potential to replace the conventional Carnot engines in broad range of fields. Many types of fuel cells — for example, proton-exchange membrane fuel cells (PEMFCs), phosphoric acid fuel cells (PAFCs), molten carbonate fuel cells (MCFCs), solid oxide fuel cells (SOFCs) — have been developed. They are classified by their electrolyte types. The electrolytes determine the operating temperatures of fuel cells, which have a great effect on their characteristics. Their characteristics are summarized in **Table 1-1**.

Table 1-1. Characteristics of different types of fuel cells.

Types	PEMFC	PAFC	MCFC	SOFC
Electrolyte	Polymers (solid) (Nafion®, etc.)	H_3PO_4 (liquid)	Molten carbonate salts (liquid)	$Zr_{1.92}Y_{0.08}O_{1.96}$ (YSZ; solid)
Anode	Pt/C or Pt–Ru/C	Pt/C	Ni alloy	Ni-YSZ
Cathode	Pt/C	Pt/C	NiO	O^{2-}/e^- conductor; (La, Sr, Ba)(Mn, Co, Fe)$O_{3-\delta}$
Operating temperatures	60–80 °C	150–200 °C	600–700 °C	800–1000 °C
Charge carrier	H^+	H^+	CO_3^{2-}	O^{2-}
Electric efficiency	40–60%	40–50%	45–60%	50–65%

Many players have been being launched their fuel cell stacks and modules as products and all types of fuel cells listed in **Table 1-1** are commercially available for stationary applications. The products and specifications are summarized in **Table 1-2**.

Table 1-2. Summary of fuel cell products for stationary applications.

PEMFC	PAFC	MCFC	SOFC
Nedstack,[27] PemGen® (48–1000 kW/-/-) Panasonic,[28] Ene-Farm (0.7 kW/40%/97%) Panasonic,[29] H2 KIBOU (5 kW/56%/95%)	Doosan Fuel Cell,[30] PureCell® Model 400 (440 kW/40–50%/90%)	FuelCell Energy,[31] SureSource 1500–4000™ (1.4–3.7 MW/45–60%/-) Scalable to ≥ 100 MW.	Kyosera,[32] Ene-Farm (0.7 kW/55%/87%) Aisin,[33] Ene-Farm (0.7 kW/55%/87%) Kyosera,[34] 3kW-SOFC (3kW/52%/90%) Miura,[35] SteelCell® (4.2kW/50%/90%) Mitsubishi,[36] Solidia® (210 kW/53%/73%) Bloom Energy,[37] Energy Server™ 5 (300 kW/53–65%/-) Ceres Power, SteelCell® Licensing company

※Note: (W/%/%) = (Power/Electric efficiency (LHV)/Overall efficiency (LHV)).

The sub-10-kW-scale products are used for residence, building and business and the products with power more than 100 kW are applied to power plant. Indeed, the Doosan Fuel Cell recently opened 50 MW by-product fuel cell plant.[38] Moreover, the Ceres Power signed up license agreements with Robert Bosch GmbH[39] and the Doosan[40] to build 200 MW and 50 MW stationary SOFC plants in Germany and South Korea, respectively, in 2024. Now, fuel cell technologies are increasingly capable of covering a wide variety of power demand by using all the types of fuel cells.

Meanwhile, the developments for emerging fuel cell markets such as transport vehicles have been

centered around solid-state fuel cells due to the beneficial properties of solid-state electrolytes in comparison with liquid ones: Less reactive, non-volatility, incombustibility and easiness for miniaturization into a thin film with a μm-scale thickness. The solid-state fuel cells are classified into two categories: PEMFCs operating at low temperatures and SOFCs operating at high temperatures. Their advantages and technical issues are summarized in **Table 1-3**.

Table 1-3. Advantages and technical issues of solid-state fuel cells.

	PEMFC	SOFC
Advantages	• Rapid start-up and shutdown • Facile module fabrication • Repeated thermal cycling	• PGM-free electrocatalysts available • Numerous chemical fuels[41,42] available such as hydrocarbon, natural gas and biofuels. • Internal reforming of fuels
Technical issues	• Water management issues due to the existence of dual phase of water[43–45] • Require large radiators[46] to manage waste heat and reduce overall energy efficiency • Require scarce and expensive PGM electrocatalysts[47,48] • Very low CO tolerance[48] (below 10 ppm) • Only ultrapure hydrogen gas for fuel	• Slow start-up and shutdown • Expensive thermal-resistant components such as either a ceramic or an alloy with high Cr or Ni contents[49,50] • Short lifetime[49–51] due to corrosion of metallic components, Cr poisoning on cathode, chemical interdiffusion and catalyst coarsening. • Low thermal cyclability[52]

※Abbreviation: Platinum group metal (PGM).

PEMFC technologies have been intensively developed in the transport sector because of their attractive advantages. GORE-SELECT® Membranes developed W. L. Gore & Associates, Inc.

(USA), a leading supplier of PEMFC technology, helped motor companies to develop fuel cell electric vehicles (FCEVs).[53] Toyota Motor Corp. succeeded in commercializing a FCEV, Mirai, for the first time in the world in 2015;[54] the maximum power of the PEMFC stack is 114 kW. Subsequently, Honda Motor Co., Ltd. also released a FCEV with a 103 kW PEMFC stack, Clarity Fuel Cell in 2016.[55] In 2018, Hyundai Motor Company launched a FCEV SUV equipped with a 95 kW PEMFC stack and a 40 kW battery, Hyundai NEXO.[56] Then, the Hyundai commercialized the fuel cell heavy-duty truck, Hyundai XCIENT Fuel Cell, which is equipped with a 190 kW PEMFC stack, for the first time in 2020.[57] In the same year, the Toyota updated the Mirai to the second-generation one with a 128 kW PEMFC stack.[58] Although the commercialization of FCEVs has been started, their markets are much smaller than those of the electrical vehicles (EVs) based on secondary lithium ion battery technology because FCEVs are still more expensive than EVs and the infrastructures for hydrogen fuels are rare.[59]

On the other hand, SOFCs have some advantages for transportation applications. It can use not only pure hydrogen but also various fuels although PEMFCs can only use highly pure hydrogen because CO_2 impurities of ~ 10's ppm can cause serious poisoning of Pt catalysts.[48] SOFCs thus have been recognized as a promising system for long-haul transportation heavy-duty vehicles.[60] Indeed, the initial design of an FCEV for intercontinental travel, received Approval in Principle from the world's largest classification society of DNV, employs the Bloom Energy's SOFC technology for a main power train with a feed of natural gases and the plans for demonstration are underway by

Samsung Heavy Industries.[61] However, SOFCs have inherent fatal flaws; slow start-up and high running costs due to the high operation temperature, which limits their widespread applications.[60] Therefore, a novel fuel cell technology bridging the gap between PEMFCs and SOFCs are strongly demanded to achieve high specific power, fuel flexibility, rapid start-up, low cost and long-term durability.

1.4. Overview of recent advances in solid-state fuel cell technologies

To tackle the technical issues of conventional solid-state fuel cells, the solid-state communities have strived to develop advanced solid-state fuel cells together with a great push into the operation at intermediate temperatures (100–800 °C); thus, high temperature PEMFCs (HT-PEMFCs), anion-exchange membrane fuel cells (AEMFCs), second generation SOFCs have been developed. Their peak power densities previously reported are summarized in **Figure 1-2**.

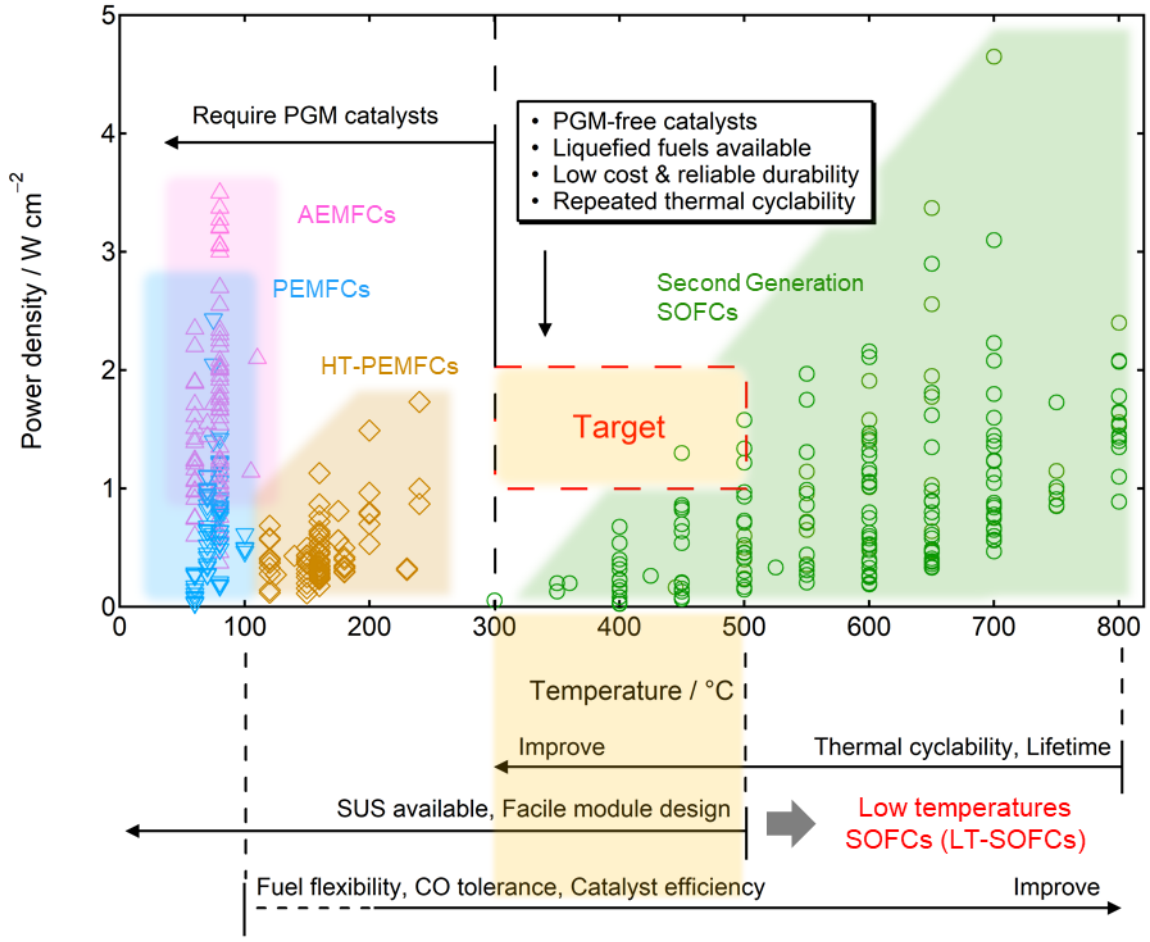

Figure 1-2. Summaries of previously reported peak power densities of advanced solid-state fuel cells along with expected properties depending on operating temperatures (blue: PEMFCs,[62–71] dark-yellow: HT-PEMFCs,[72–86] pink: AEMFCs,[87–100] and green: Second Generation SOFCs[101–147]).

1.4.1. Advanced polymer electrolyte membrane fuel cells

The technical issues of PEMFCs can be solved when the operation temperature increases to above 100 °C. Such HT-PEMFCs can easily manage the exhaust of water and heat because of the existence of a single phase water vapor and large temperature gap to the external environment.[44] Moreover, CO tolerance is dramatically improved at elevated temperatures.[148,149] These merits of HT-PEMFCs have motivated researchers to develop novel polymer electrolyte membranes that can retain high proton conductivity at temperatures above 100 °C. A recent reports for HT-PEMFC[72] has achieved peak power densities of 1.13 W cm^{-2} at 160 °C and 1.74 W cm^{-2} at 240 °C, which are comparable with those of conventional PEMFCs, under H_2/O_2 conditions by using sophisticated phosphonated polymers. However, the performances significantly diminish under H_2/air conditions,[72] and the total PGM loading, (1.1–1.75 mg-PGM cm^{-2})[72] is far larger than the target of the United States Department of Energy (DoE) by 2025[150] (0.125 mg-PGM cm^{-2}; DoE pursues a goal of PGM-free fuel cells by 2030[150]).

Meanwhile, with the aim of reducing the PGM loading, AEMFCs that employ OH^- conducting polymer electrolyte membranes have attracted considerable attentions because their alkaline environment is favorable for oxygen reduction reactions.[151,152] A recent report have succeeded in fabricating AEMFCs with commercial Fe–N–C cathodes paired with low-loading Pt–Ru/C anodes (0.125 mg-Pt–Ru cm^{-2}) and their peak power density exceeds 1 W cm^{-2} under H_2/air.[100] However, AEMFCs face the same technical issues with PEMFCs such as water and heat management and fuel

limitations because they still need PGM catalysts for anode and operate at temperatures below 100 °C. Further, the long-term durability is a big issue in AEMFC community.[153]

1.4.2. Advanced solid oxide fuel cells

On the other hand, SOFC community has desired to eradicate the inherent fatal drawbacks of SOFCs regarding the high temperature operation. Hence, extensive endeavors have been dedicated to developing advanced SOFCs that can operate at far below 800 °C. The SOFCs that operates at low temperatures of 300–500 °C (LT-SOFCs) have outstanding technical benefits, as shown in **Figure 1-2**. They allow us to use low-priced metallic components such as stainless steel,[49,50] and thus significant cost cuts of SOFC systems. In addition, the thermal stress and material degradation are significantly lowered in the temperature region.[50] Thus, LT-SOFCs are expected to satisfy the reliable long-term durability, repeated thermal cyclability and tolerance to thermal shock with rapid start-up. Moreover, they can still conduct fuel cell reactions with PGM-free electrocatalysts because transition metal oxides cathodes outperform Pt cathode at above 300 °C.[147] Therefore, LT-SOFCs have the potential to be an ideal system satisfying reliable durability, high energy efficiency, high power gain and low cost, and thus are applicable to transport vehicles. Hence, they can be a game changer in the fuel cell market and play a key role in broadening the applications of SOFCs by bridging the gap between PEMFCs and SOFCs.

To gain the target power of over 1 W cm^{-2}, the total area-specific resistances (ASRs) of a fuel cell must be smaller than 0.3 Ω cm^2. ASR of conventional SOFCs shoots up with the decrease in

operating temperatures below 800 °C due to the enlarged resistances regarding electrolyte and cathodic reactions. Thus, extensive studies have been focused on the development of second generation SOFCs that minimize the ohmic loss and boost cathodic reactions at low temperatures. This involves two key approaches: i) SOFCs with innovative materials and ii) microstructurally engineered SOFCs (micro-SOFCs). With the development of innovative electrolyte and electrode materials, recent SOFCs[115,116,120,121] have achieved peak power densities of over 0.7 W cm^{-2} at 500 °C. A $Gd_{0.1}Ce_{0.9}O_{1.95}$ (CGO)-based SOFC with a core/shell fiber-structured composite cathode exhibited an impressive power density as high as 1.58 W cm^{-2} at 500 °C;[116] however, the performance sharply dropped with decreases in operating temperatures below than 500 °C.[116] A micro-SOFC was developed using a semiconductor fabrication process, which consist of a corrugated 60-nm-thick composite electrolyte (50-nm-thick YSZ and 10-nm-thick yttria-doped ceria) sandwiched between porous 80-nm-thick Pt electrodes. The cell showed an exceptional peak power density of 1.3 W cm^{-2} at 450 °C, but the performances abruptly decreased to 0.54 W cm^{-2} at 400 °C and rapidly deteriorate due to agglomeration of noble electrodes.[143] Moreover, such ultra-thin free standing structures are mechanically fragile and thus result in catastrophic fracture when they are scaled up.[154,155] Although a large-scale micropatterned SOFC that consists of an about-1-μm-thick composite electrolyte with CGO/YSZ multilayers has recently been developed via polymer-to-ceramic matrix transition, its peak power densities considerably decrease from 0.931 W cm^{-2} at 500 °C to 0.233 W cm^{-2} at 400 °C.[122] Therefore, it is still a great challenge to fabricate high-power LT-SOFCs.

1.5. Protonic ceramic fuel cells

These circumstances have driven interest in protonic ceramic fuel cells (PCFCs). They typically employ acceptor-doped alkaline earth cerates, zirconates and related derivatives for electrolytes. The ceramic oxides possess proton conductivity under humified atmosphere due to their high negative values for the standard enthalpy of hydration reaction, $H_2O + V_O^{\bullet\bullet} + O_O^{\times} \rightleftarrows 2OH_O^{\bullet}$.[156] As is the case with conventional SOFCs, porous-anode-support-type fuel cells are normally applicable; they comprise a porous cathode of an O^{2-}/e^- mixed conductor, a dense protonic electrolyte membrane and a porous anode support of a Ni-electrolyte cermet, as shown in **Figure 1-3**.

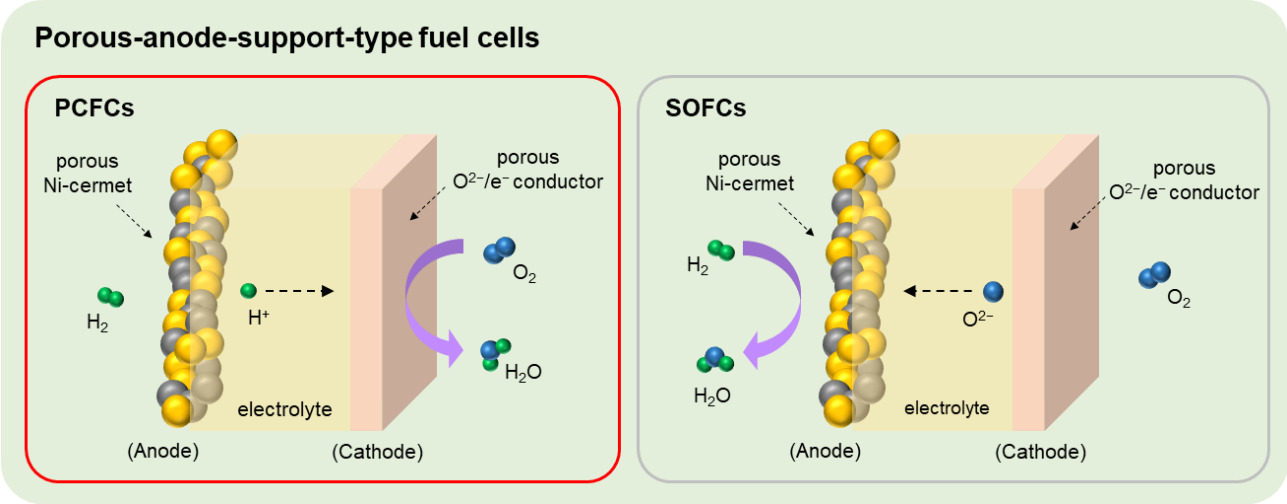

Figure 1-3. Illustration of structure of PCFCs and SOFCs.

PCFCs are alternative candidates to oxide-ion conducing SOFCs. Protonic ceramic electrolytes, e.g., $BaZr_xCe_{1-x-y}M_yO_{3-\delta}$ (M = Y, Yb, etc.), have smaller activation energies for ionic conduction than oxide-ion conductors such as YSZ and CGO, which of the former and the latter are 0.3–0.6 eV and 0.8 eV, respectively,[157] thereby resulting in higher conductivity below 500 °C.[158,159] Hence, PCFCs

are more advantageous to operation at lowered temperatures than SOFCs. In addition, since water formation reactions occur at the cathode in PCFCs, as shown in **Figure 1-3**, they do not suffer fuel dilution and detrimental anode metal oxidation during operation contrary to oxide-ion conducting SOFCs.[160] No fuel dilution allows maintaining high operating voltage with high fuel utilization during operation.[161] Further, PCFCs were demonstrated to show excellent tolerance to notorious carbon coking and sulfur poisoning,[158,162] which are major causes of performance degradation of Ni-based SOFCs,[163] because OH species formed on the surface of protonic ceramics can facilitate carbon/sulfur removal from the Ni surface in the cermet anodes;[162,163] thus, PCFCs can stably operate with a direct feed of carbon/sulfur containing fuels such as iso-butane, propane, methanol and natural gas with/without H_2S at 500 °C for 1,000–8,000 h.[162] Thus, PCFCs are a promising candidate for LT-SOFCs.

1.6. Motivations and objectives of this thesis

It is a critical challenge to fabricate high-power PCFCs. Unfortunately, only a few studies have reported peak power densities of PCFCs exceeding 0.5 W cm^{-2} at 500 °C;[160,164–168] thus, their performance lags far behind that of SOFCs. This is attributed to greater ohmic loss[165] than expected and enlarged cathodic polarization resistance[160]; PCFCs have used the O^{2-}/e^{-} conducting transition metals-base perovskite cathodes as is the case with conventional SOFCs, so that the carrier mismatch between electrolytes and cathodes limits the effective reaction area within gas–electrolyte–cathode triple-phase boundaries (TPBs).[169] Among numerous approaches to overcome these problems including innovative materials development and device engineering, recent studies[165,166] have highlighted the importance of heterostructures. Of them, a hydrogen-permeable metal-support-type fuel cells (HMFC), which is based on a solid–solid heterostructure consisting of a 1-μm-thick $BaCe_{0.8}Y_{0.2}O_{3-\delta}$ thin film on a dense, hydrogen-permeable metal anode support, gained an extraordinary peak power density of 0.9 W cm^{-2} at 400 °C, the highest-ever performance reported in the SOFC community, with a total ASR of only 0.34 Ω cm^2 (the ohmic ASR: 0.13 Ω cm^2 and the ASR of polarization: 0.21 Ω cm^2).[170] This demonstrates that its configuration is conducive for ensuring low electrolyte and cathode polarization resistances even at low temperatures. However, given that it used conventional electrolyte and cathode materials of PCFCs,[170] its power generation mechanism is still unclear.

A further challenge in PCFC development is to fabricate ceramic cells with chemically stable

protonic electrolyte materials for their use with carbon containing fuels. $BaCeO_3$-based oxides display excellent proton conductivity of 1–15 mS cm^{-1} at the 300–500 °C,[158,159] but they are thermodynamically unstable in a CO_2-containing atmosphere below 800 °C,[171] resulting in their decomposition to $BaCO_3$ and CeO_2. In contrast, $BaZrO_3$ is thermodynamically stable in a CO_2-rich atmosphere; thus, the partial replacement of Ce with Zr can improve the stability in a CO_2-rich atmosphere.[172,173] Solid solutions, $BaZr_xCe_{1-x-y}M_yO_{3-\delta}$ (BZCM; M = Y, Yb, etc.) tend to be more tolerant to CO_2 with the increasing Zr contents[172,173] and thus Zr-rich BZCM is desirable as a practical electrolyte for LT-SOFCs. Meanwhile, the fuel cell performances are still limited because the solid solutions tend to show poor sinterability with increasing Zr contents due to high refractory nature of $BaZrO_3$ moieties, and their coarse-grained microstructures have large grain-boundary resistances of electrolytes.[172,173] Normally, Zr-rich phases require sintering temperatures over 1600 °C for sufficient grain growth,[174] but such high temperature sintering causes BaO evaporation and undesired reaction at the interface between the electrolyte and cermet anodes, which significantly increases electrolyte resistances of fuel cells.[175,176]

This thesis aims at obtaining scientific insights on device engineering of high-power PCFCs by means of protonic ceramic thin film electrolytes for development of highly efficient LT-SOFCs. It has two main objectives. One is to fabricate highly efficient porous-anode-support-type fuel cells with large-grained electrolyte films using high Zr-content BZCY under moderate sintering conditions. The other is to understand the power generation mechanism of HMFC and give scientific insights into

fuel cell device engineering; thus, I have revealed how HMFC generates high power density despite using the conventional materials through experimental and theoretical approaches. Finally, I have developed prototype HMFCs based on Pd-alternative hydrogen permeable metal anode.

1.7. Contents of this thesis

This thesis consists of 6 chapters as follows.

Chapter 1 gives an overview of the backgrounds and recent advances of solid-state fuel cell technologies and highlights the necessity of LT-SOFCs. The motivations and objectives in these studies are also described.

In Chapter 2, porous-anode-support-type fuel cells based on Zr-rich $BaZr_xCe_{0.8-x}Y_{0.2}O_{3-\delta}$ (BZCY; $x \geq 0.4$) electrolytes were fabricated via one step co-firing process with $Zn(NO_3)_2$ additives at relatively low sintering temperature. Owing to the improved sinterability, the BZCY6 cell showed 3 times higher peak power densities than the analogous cell fabricated via wet chemical processes. Further, the CO_2 tolerance of the BZCY6 cell was demonstrated.

In Chapter 3, to understand the power generation mechanism of HMFC, the electrochemical behavior was compared between porous-anode-support-type fuel cells and HMFCs by means of numerical and electrochemical methods. The Nernst–Planck–Poisson model was employed to simulate the defect concentration profiles in a BZCM electrolyte on both type of cells. Combined experimental and simulation results demonstrated that the retardation of oxide-ion conduction at the metal/electrolyte heterointerfaces heavily hydrates the electrolyte membrane so as to compensate for negative charge of the oxide ions accumulating near the interfaces due to the prevention of their conduction, which is named *proton pumping*. Further, it is suggested that the proton pumping develops noticeably enlarged concentration gradient of proton in the vicinity of cathode interfaces,

facilitating proton interfacial diffusion and boosting energy conversion. These phenomena were thermodynamically understood by assuming quasi-equilibrium; this indicated that the metal/oxide heterointerfaces incredibly enhance chemical potential of water.

In Chapter 4, HMFCs comprising oxygen-nonstoichiometric $BaZr_{1-x}Sc_xO_{3-x/2}$ electrolytes (x = 0.2 and 0.5) were fabricated to demonstrate effects of oxygen deficiency on proton pumping. The HMFC with highly-oxygen-deficient $BaZr_{0.5}Sc_{0.5}O_3$ electrolyte is capable of inducing enhanced proton pumping and thus achieved the cathode reaction resistance of 0.54 Ω cm^2 at 400°C under DC conditions with conventional O^{2-}/e^- conducting cathode materials. The oxygen surface exchange near the TPB is sufficiently fast in HMFCs and the cathode reaction is thus completed within TPB zones without via the long-range diffusion of O adatoms, as confirmed by numerical and electrochemical analysis. These findings demonstrate that HMFC is a system that utilize overpotential efficiently. Hence, HMFCs can be an approach for future advanced ceramic fuel cells at low temperature. Further, the discriminative features of bias-dependent R_p in HMFCs will open a new route to design of electrochemical devices achieving close-to-zero polarization even at low temperature below 400°C.

In Chapter 5, prototype HMFCs were constructed with transition metal base hydrogen-permeable anode, i.e., V-Ni alloy foils. They could produce a stable power generation at temperatures below 350 °C, demonstrating the possibility of Pd-free HMFC operating in low temperature region.

In Chapter 6, the overall summary and conclusion of this thesis are presented.

1.8. References

1. IPCC, 2014: *Climate Change 2014: Synthesis Report. Contribution of Working Groups I, II and III to the Fifth Assessment Report of the Intergovernmental Panel on Climate Change* [Core Writing Team, R.K. Pachauri and L.A. Meyer (eds.)]. IPCC, Geneva, Switzerland, 151 pp.

2. Hannah Ritchie and Max Roser (2020) "CO_2 and Greenhouse Gas Emissions". *Published online at OurWorldInData.org*. Retrieved from: 'https://ourworldindata.org/co2-and-other-greenhouse-gas-emissions' [Online Resources]

3. Theo Stein (2020) "Carbon dioxide peaks near 420 parts per million at Mauna Loa observatory". Published online at *www.noaa.gov.* Retrieved from: 'https://research.noaa.gov/article/ArtMID/587/ArticleID/2764/Coronavirus-response-barely-slows-rising-carbon-dioxide' [Online Resources]

4. IPCC, 2021: Summary for Policymakers. In: *Climate Change 2021: The Physical Science Basis. Contribution of Working Group I to the Sixth Assessment Report of the Intergovernmental Panel on Climate Change* [Masson-Delmotte, V., P. Zhai, A. Pirani, S. L. Connors, C. Péan, S. Berger, N. Caud, Y. Chen, L. Goldfarb, M. I. Gomis, M. Huang, K. Leitzell, E. Lonnoy, J.B.R. Matthews, T. K. Maycock, T. Waterfield, O. Yelekçi, R. Yu and B. Zhou (eds.)]. Cambridge University Press. In Press.

5. IPCC, 2018: *Global Warming of 1.5°C.An IPCC Special Report on the impacts of global warming of 1.5°C above pre-industrial levels and related global greenhouse gas emission pathways, in the context of strengthening the global response to the threat of climate change, sustainable development, and efforts to eradicate poverty* [Masson-Delmotte, V., P. Zhai, H.-O. Pörtner, D. Roberts, J. Skea, P.R. Shukla, A. Pirani, W. Moufouma-Okia, C. Péan, R. Pidcock, S. Connors, J.B.R. Matthews, Y. Chen, X. Zhou, M.I. Gomis, E. Lonnoy, T. Maycock, M. Tignor, and T. Waterfield (eds.)]. In Press.

6. United Nations, Framework Convention on Climate Change (2021). *Nationally Determined Contributions under the Paris Agreement* (FCCC/PA/CMA/2021/8).

7. United Nations, Department of Economic and Social Affairs, Population Division (2019). *World Population Prospect 2019: Highlights* (ST/ESA/SER.A/423).

8. IRENA (2021), *Renewable Power Generation Costs in 2020*, International Renewable Energy Agency, Abu Dhabi.

9. N. Kannan, D. Vakeesan, "Solar energy for future world: -A review" *Renewable and Sustainable Energy Review* **2016**, 62, 1092.

10. IEA (2021), Key World Energy Statistics 2021, IEA, Paris https://www.iea.org/reports/key-world-energy-statistics-2021.

11. IEA (2021), *Net Zero by 2050*, IEA, Paris https://www.iea.org/reports/net-zero-by-2050.

12. IRENA (2019), *Global energy transformation: A roadmap to 2050 (2019 edition)*, International Renewable Energy Agency, Abu Dhabi.
13. B. E. Layton, "A comparison of energy densities of prevalent energy sources in units of joules per cubic meter" *Int. J. Green Energy* **2018**, 5, 438.
14. IEA (2019), *Solar Energy: Mapping the Road Ahead*, IEA, Paris https://www.iea.org/reports/solar-energy-mapping-the-road-ahead.
15. E. Fanone, A. Gamba and M. Prokopczuk, "The case of negative day-ahead electricity prices" *Energy Economics* **2013**, 35, 22.
16. X. C. Fan, W. Q. Wang, R. J. Shi and F. T. Li, "Analysis and countermeasures of wind power curtailment in China" *Renewable and Sustainable Energy Review* **2015**, 52, 1429.
17. C. Dong, Y. Qi, W. Dong, X. Lu, T. Liu and S. Qian, "Decomposing driving factors for wind curtailment under economic new normal in China" *Appl. Energy* **2018**, 217, 178.
18. F. Xia, X. Lu and F. Song, "The role of feed-in tariff in the curtailment of wind power in China" *Energy Economics* **2020**, 86, 104661.
19. S. Rehman, L. M. A. Hadhrami and M. M. Alam, "Pumped hydro energy storage system: A technological review" *Renewable and Sustainable Energy Reviews* **2015**, 44, 586.
20. J. Wang, K. Lu, L. Ma, J. Wang, M. Dooner, S. Miao, J. Li and D. Wang, "Overview of Compressed Air Energy Storage and Technology Development" *Energies* **2017**, 10, 991.
21. K. C. Divya and J. Ostergaard, "Battery energy storage technology for power systems — An overview" *Electric Power Systems Research* **2009**, 79, 511.
22. D. M. Davies, M. G. Verde, O. Mnyshenko, Y. R. Chenm R. Rajeev, Y. S. Meng and G. Elliott, "Combined economic and technological evaluation of battery energy storage for grid applications" *Nat. Energy* **2019**, 4, 42.
23. S. V. Renssen, "The hydrogen solution?" *Nature Climate Change* **2020**, 10, 799.
24. M. A. Pellow, C. J. M. Emmott, C. J. Barnhart and S. M. Benson, "Hydrogen or batteries for grid storage? A net energy analysis" *Energy Environ. Sci.* **2015**, 8, 1938.
25. IEA (2019), *The Future of Hydrogen*, IEA, Paris https://www.iea.org/reports/the-future-of-hydrogen.
26. B. R. Sutherland, "Sustainably Heating Heavy Industry" *Joule* **2020**, 4, 14.
27. Nedstack. Source: https://nedstack.com/en.
28. Panasonic Corporation. Source: https://panasonic.biz/appliance/FC/lineup/manshion.html.
29. Panasonic Corporation. Source: https://news.panasonic.com/global/press/data/2021/10/en211001-4/en211001-4.html.
30. Doosan Fuel Cell. Source: https://www.doosanfuelcell.com/en/prod/prod-0101.

31. FuelCell Energy, Inc. Source: https://www.fuelcellenergy.com/products.
32. Kyosera Corporation. Source: https://global.kyocera.com/prdct/ecd/sofc.
33. AISIN Corporation. Source: https://www.aisin.com/jp/product/energy/cogene/enefarm/products.
34. Kyosera Corporation. Source: https://www.kyocera.co.jp/news/2017/0605_ipfa.html.
35. Miura Co., Ltd. Source: https://www.miuraz.co.jp/product/thermoelectric/sofc.html.
36. Mitsubishi Heavy Industries, Ltd. Source: https://power.mhi.com/products/sofc.
37. Bloom Energy. "Bloom Energy Sever ES5-300kW" Source: https://www.bloomenergy.com/wp-content/uploads/es5-300kw-datasheet-2019.pdf.
38. Fuel Cells Bulletin (2020). "Hanwa, Doosan open by-product hydrogen fuel cell power plant" 2020(8) 7.
39. FuelCellsWorks (2020). "Ceres and Bosch Scale up for Mass Solid Oxide Fuel Cell (SOFC) Production" Source: https://fuelcellsworks.com/news/ceres-and-bosch-scale-up-for-mass-solid-oxide-fuel-cell-sofc-production.
40. FuelCellsWorks (2020). "Ceres and Doosan Expand Strategic Collaboration with Mass Manufacturing in South Korea" Source: https://fuelcellsworks.com/news/ceres-and-doosan-expand-strategic-collaboration-with-mass-manufacturing-in-south-korea.
41. E. P. Murray, T. Tsai and S. A. Barnett, "A direct-methane fuel cell with a ceria-based anode" *Nature* **1999**, 400, 649.
42. B. C. H. Steele and A. Heinzel, "Materials for fuel-cell technologies" *Nature* **2001**, 414, 345.
43. K. H. Kim, K. Y. Lee, S. Y. Lee, E. A. Cho, T. H. Lim, H. J. Kim, S. P. Yoon, S. H. Kim, T. W. Lim and J. H. Jang, "The effects of relative humidity on the performances of PEMFC MEAs with various Nafion® ionomer contents" *Int. J. Hydrogen Energy* **2010**, 35, 13104.
44. A. Chandan, M. Hattenberger, A. El-kharouf, S. Du, A. Dhir, V. Self, B. G. Pollet, A. Ingram and W. Bujalski, "High temperature (HT) polymer membrane fuel cells (PEMFC) – A review" *J. Power Sources* **2013**, 231, 264.
45. H. Li, Y. Tang, Z. Wang, Z. Shi, S. Wu, D. Song, J. Zhang, K. Fatih, J. Zhang, H. Wang, Z. Liu, R. Abouatallah and A. Mazza, "A review of water flooding issues in the proton exchange membrane fuel cell" *J. Power Sources* **2000**, 178, 103.
46. T. Yoshida and K. Kojima, "Toyota MIRAI Fuel Cell Vehicle and Progress Toward a Future Hydrogen Society" *Electrochem. Soc. Interface* **2015**, 24, 45.
47. C. Y. Chen, W. H. Lai, W. M. Yan, C. C. Chen, S. W. Hsu, "Effects of nitrogen and carbon monoxide concentrations on performance of proton exchange membrane fuel cells with Pt–Ru anodic catalyst" *J. Power Sources* **2013**, 243, 138.
48. C. Y. Chen and K. P. Huang, "Performance and transient behavior of the kW-grade PEMFC stack

with the Pt–Ru catalyst under CO-contained diluted hydrogen" *Int*. *J*. *Hydrogen Energy* **2017**, 42, 22250.

49. D. J. L. Brett, A. Atkinson, N. P. Brandon, S. J. Skinner, "Intermediate temperature solid oxide fuel cells" *Chem*. *Soc*. *Rev*. **2008**, 37, 1568.

50. Z. Gao, L. V. Mogni, E. C. Miller, J. G. Railsback and S. A. Barnett, "A perspective on low-temperature solid oxide fuel cells" *Energy Environ*. *Sci*. **2016**, 9, 1602.

51. H. Yokokawa, T. Horita, K. Yamaji, M. E. Brito, Y. P. Xiong and H. Kishimoto, "Thermodynamic considerations on Cr poisoning in SOFC cathodes" *Solid State Ionics* **2006**, 177, 3193.

52. E. I. Tiffee, A. Weber and D. Herbstritt, "Materials and technologies for SOFC-components" *J*. *Eur*. *Ceram*. *Soc*. **2001**, 21, 1805.

53. W. L. Gore & Associates, Inc. "Gore's Fuel Cell Technology Helps Power Latest Hyundai Fuel Cell Vehicle. Source: https://www.gore.com/news-events/press-release/gore-s-fuel-cell-technology-helps-power-latest-hyundai-fuel-cell-vehicle.

54. Toyota Motor Co., Ltd. Source:
https://toyota.jp/pages/contents/mirai/001_p_001/pdf/spec/mirai_spec_201501.pdf.

55. Honda Motor Co., Ltd. Source:
https://global.honda/heritage/timeline/product-history/automobiles/2016Clarity-Fuel-Cell.html.

56. Hyundai Motor Company. Source:
https://www.hyundainews.com/en-us/models/hyundai-nexo-2019-nexo/specifications.

57. FuelCellsWorks (2020). "World's First Fuel Cell Heavy-Duty Truck, Hyundai XCIENT Fuel Cell, Heads to Europe for Commercial Use" Source: https://fuelcellsworks.com/news/worlds-first-fuel-cell-heavy-duty-truck-hyundai-xcient-fuel-cell-heads-to-europe-for-commercial-use.

58. FuelCellsWorks (2020). "New Mirai Hydrogen Fuel Cell Electric Vehicle – Under the Skin" Source: https://mag.toyota.co.uk/new-mirai-hydrogen-fuel-cell-electric-vehicle.

59. Erin L. Redmond *et al* 2018 *Meet*. *Abstr*. MA2018-02 1455.

60. F. Baldi, S. Moret, K. Tammi, F. Marechal, "The role of solid oxide fuel cells in future ship energy systems" *Energy* **2020**, 194, 116811.

61. Bloom Energy (2021). "Bloom energy achieves key milestones on its path to decarbonize the marine industry" Source: https://www.bloomenergy.com/news/bloom-energy-achieves-key-milestones-on-its-path-to-decarbonize-the-marine-industry.

62. S. Liu, S. Li, R. Wang, Y. Rao, Q. Zhong, K. Hong and M. Pan, "Preparation of High Performance and Ultra-Low Platinum Loading Membrane Electrode Assembly for PEMFC Commercial Application" *J*. *Electrochem*. *Soc*. **2019**, 166, F1308.

63. M. Tsipoaka, M. A. Aziz and S. Shanmugam, "Degradation-Mitigating Composite Membrane

That Exceeds a 1 W cm^{-2} Power Density of a Polymer Electrolyte Membrane Fuel Cell Operating Under Dry Conditions" *ACS Sustainable Chem*. *Eng*. **2021**, 9, 2693.

64. X. Fu, P. Zamani, J. Y. Choi, F. M. Hassan, G. Jiang, D. C. Higgins, Y. Zhang, M. A. Hoque and Z. Chen, "In situ Polymer Graphenization Ingrained with Nanoporosity in a Nitrogenous Electrocatalyst Boosting the Performance of Polymer-Electrolyte-Membrane Fuel Cells" *Adv*. *Mater*. **2017**, 29, 1604456.

65. D. Zhao, B. L. Yi, H. M. Zhang, H. M. Yu, L. Wang, Y. W. Ma and D. M. Xing, "Cesium substituted 12-tungstophosphoric ($Cs_xH_{3-x}PW_{12}O_{40}$) loaded on ceria-degradation mitigation in polymer electrolyte membranes" *J*. *Power Sources* **2009**, 190, 301.

66. H. C. Chien, L. D. Tsai, C. M. Lai, J. N. Lin, C. Y. Zhu, F. C. Chang, "Characteristics of high-water-uptake activated carbon/Nafion hybrid membranes for proton exchange membrane fuel cells" *J*. *Power Sources* **2013**, 226, 87.

67. A. Dorjgotov, Y. Jeon, J. Hwang, B. Ulziidelger, H. S. Kim, B. Han and Y. G. Shul, "Synthesis of Durable Small-Sized Bilayer Au@Pt Nanoparticles for High Performance PEMFC Catalysts" *Electrochimica Acta* **2017**, 228, 389.

68. W. Zheng, L. Wang, F. Deng, S. A. Giles, A. K. Prasad, S. G. Advani, Y. Yan and D. G. Vlachos, "Durable and self-hydrating tungsten carbide-based composite polymer electrolyte membrane fuel cells" *Nat*. *Commun*. **2017**, 8, 418.

69. Y. Kim, K. Ketpang, S. Jaritphun, J. S. Park and S. Shanmugam, "A polyoxometalate coupled graphen oxide–Nafion composite membrane for fuel cells operating at low relative humidity" *J*. *Mater*. *Chem*. *A* **2015**, 3, 8148.

70. K. Ketpang, K. Lee and S. Shanmugam, "Facile Synthesis of Porous Metal Oxide Nanotubes and Modified Nafion Composite Membranes for Polymer Electrolyte Fuel Cells Operated under Low Relative Humidity" *ACS Appl*. *Mater*. *Interfaces* **2014**, 6, 16734.

71. M. Vinothkannan, R. Hariprasad, S. Ramakrishnan, A. R. Kim and D. J. Yoo, "Potential Bifunctional Filler (CeO_2–ACNTs) for Nafion Matrix toward Extended Electrochemical Power Density and Durability in Proton-Exchange Membrane Fuel Cells Operating at Reduced Relative Humidity" *ACS Sustainable Chem*. *Eng*. **2019**, 7, 12847.

72. V. Atanasov, A. S. Lee, E. J. Park, S. Maurya, E. D. Baca, C. Fujimoto, M. Hibbs, I. Matanovic, J. Kerres and Y. S. Kim, "Synergistically integrated phosphonated poly(pentafluorostyrene) for fuel cells" *Nat*. *Mater*. **2021**, 20, 370.

73. J. Zhang, Y. Tang, C. Song, Z. Xia, H. Li, H. Wang, J. Zhang, "PEM fuel cell relative humidity (RH) and its effect on performance at high temperatures" *Electrochimica Acta* **2008**, 53, 5315.

74. J. Zhang, Y. Tang, C. Song, Z. Zhang, "Polybenzimidazole-membrane-based PEM fuel cell in the

temperature range of 120–200 °C" *J. Power Sources* **2007**, 172, 163.
75. S. Martin, J. O. Jensen, Q. Li, P. L. Garcia-Ybarra and J. L. Castillo, "Feasibility of ultra-low Pt loading electrodes for high temperature proton exchange membrane fuel cells based in phosphoric acid-doped membrane" *Int. J. Hydrogen Energy* **2019**, 44, 28273.
76. Y. Cheng, S. He, S. Lu, J. P. Veder, B. Johannessen, L. Thomsen, M. Saunders, T. Becker, R. D. Marco, Q. Li, S. Yang and S. P. Jiang, "Iron Single Atoms on Graphene as Nonprecious Metal Catalysts for High-Temperature Polymer Electrolyte Membrane Fuel Cells" *Adv. Sci.* **2019**, 6, 1802066.
77. N. N. Krishnan, N. M. H. Duong, A. Konovalova, J. H. Jang, H. S. Park, H. J. Kim, A. Roznowska, A. Michalak, D. Henkensmeier, "Polybenzimidazole / tetrazole-modified poly(arylene ether) blend membranes for high temperature proton exchange membrane fuel cells" *J. Membr. Sci.* **2020**, 614, 118494.
78. D. Yao, W. Zhang, Q. Ma, Q. Xu, S. Pasupathi and H. Su, "Achieving high Pt utilization and superior performance of high temperature polymer electrolyte membrane fuel cell by employing low-Pt-content catalyst and microporous layer free electrode design" *J. Power Sources* **2019**, 426, 124.
79. F. Seland, T. Berning, B. Borresen and R. Tunold, "Improving the performance of high-temperature PEM fuel cells based on PBI electrolyte" *J. Power Sources* **2006**, 160, 27.
80. C. Wannek, W. Lehnert and J. Mergel, "Membrane electrode assemblies for high-temperature polymer electrolyte fuel cells based on *poly*(2,5-benzimidazole) membranes with phosphoric acid impregnation via the catalyst layers" *J. Power Sources* **2009**, 192, 258.
81. O. E. Kongstein, T. Berning, B. Borresen, F. Seland and R. Tunold, "Polymer electrolyte fuel cells based on phosphoric acid doped polybenzimidazole (PBI) membranes" *Energy* **2007**, 32, 418.
82. H. Su, T. C. Jao, O. Barron, B. G. Pollet and S. Pasupathi, "Low platinum loading for high temperature proton exchange membrane fuel cell developed by ultrasonic spray coating technique" *J. Power Sources* **2014**, 267, 155.
83. S. Martin, P. L. Garcia-Ybarra and J. L. Castillo, "Ten-fold reduction from the state-of-the-art platinum loading of electrodes prepared by electrospraying for high temperature proton exchange membrane fuel cells" *Electrochem. Commun.* **2018**, 93, 57.
84. H. Su, S. Pasupathi, B. J. Bladergroen, V. Linkov and B. G. Pollet, "Enhanced performance of polybenzimidazole-based high temperature proton exchange membrane fuel cell with gas diffusion electrodes prepared by automatic catalyst spraying under irradiation technique" *J. Power Sources* **2013**, 242, 510.
85. H. Su, Q. Xu, J. Chong, H. Li, C. Sita and S. Pasupathi, "Eliminating micro-porous layer from gas diffusion electrode for use in high temperature polymer electrolyte membrane fuel cell" *J. Power*

Sources **2017**, 341, 302.

86. H. Su, T. C. Jao, S. Pasupathi, B. J. Bladergroen, V. Linkov and B. G. Pollet, "A novel dual catalyst layer structured gas diffusion electrode for enhanced performance of high temperature proton exchange membrane fuel cell" *J. Power Sources* **2014**, 246, 63.

87. N. Chen, H. H. Wang, S. P. Kim, H. M. Kim, W. H. Lee, C. Hu, J. Y. Bae, E. S. Sim, Y. C. Chung, J. H. Jang, S. J. Yoo, Y. Zhuang and Y. M. Lee, "Poly(fluorenyl aryl piperidinium) membranes and ionomers for anion exchange membrane fuel cells" *Nat. Commun.* **2021**, 12, 2367.

88. G. Huang, M. Mandal, X. Peng, A. C. Yang-Neyerlin, B. S. Pivovar, W. E. Mustain and P. A. Kohl, "Composite Poly(norbornene) Anion Conducting Membranes Achieving Durability, Water Management and High Power (3.4 W/cm^2) in Hydrogen/Oxygen Alkaline Fuel Cells" *J. Electrochem. Soc.* **2019**, 166, F637.

89. L. Wang, M. Bellini, H. A. Miller and J. R. Varcoe, "A high conductivity ultrathin anion-exchange membrane with 500+ h alkali stability for use in alkaline membrane fuel cells that can achieve 2 W cm^{-2} at 80 °C" *J. Mater. Chem. A* **2018**, 6, 15404.

90. M. Mandal, G. Huang, N. U. Hassan, X. Peng, T. Gu, A. H. Brooks-Starks, B. Bahar, W. E. Mustain and P. A. Kohl, "The Importance of Water Transport in High Conductivity and High-Power Alkaline Fuel Cells" *J. Electrochem. Soc.* **2020**, 167, 054501.

91. J. C. Douglin, J. R. Varcoe and D. R. Dekel, "A high-temperature anion-exchange membrane fuel cell" *J. Power Sources Adv.* **2020**, 5, 100023.

92. J. C. Douglin, R. K. Singh, S. Haj-Bsoul, S. Li, J. Biemolt, N. Yan, J. R. Varcoe, G. Rothenberg and D. R. Dekel, "A high-temperature anion-exchange membrane fuel cell with a critical raw material-free cathode" *Chem. Eng. J. Adv.* **2021**, 8, 100153.

93. Y. Yang, H. Peng, Y. Xiong, Q. Li, J. Lu, L. Xiao, F. J. DiSalvo, L. Zhuang and H. D. Abruna, "High-Loading Composition-Tolerant Co–Mn Spinel Oxides with Performance beyond 1 W/cm^2 in Alkaline Polymer Electrolyte Fuel Cells" *ACS Energy Lett.* **2019**, 4, 1251.

94. X. Peng, D. Kulkarni, Y. Huang, T. J. Omasta, B. Ng, Y. Zheng, L. Wang, J. M. LaManna, D. S. Hussey, J. R. Varcoe, I. V. Zenyuk and W. E. Mustain, "Using operando techniques to understand and design high performance and stable alkaline membrane fuel cells" *Nat. Commun.* **2020**, 11, 3561.

95. L. Wang, X. Peng, W. E. Mustain and J. R. Varcoe, "Radiation-grafted anion-exchange membranes: the switch from low- to high-density polyethylene leads to remarkably enhanced fuel cell performance" *Energy Environ. Sci.* **2019**, 12, 1575.

96. M. S. Cha, J. E. Park, S. Kim, S. H. Han, S. H. Shin, S. H. Yang, T. H. Kim, D. M. Yu, S. So, Y. T. Hong, S. J. Yoon, S. G. Oh, S. Y. Kang, O. H. Kim, H. S. Park, B. Bae, Y. E. Sung, Y. H. Cho and J. Y. Lee, "Poly(carbazole)-based anion-conducting materials with high performance and durability

for energy conversion devices" *Energy Environ*. *Sci*. **2020**, 13, 3633.
97. M. Mandal, G. Huang, N. U. Hassan, W. E. Mustain and P. A. Kohl, "Poly(norbornene) anion conductive membranes: homopolymer, block copolymer and random copolymer properties and performance" *J*. *Mater*. *Chem*. *A* **2020**, 8, 17568.
98. Q. Li, H. Peng, Y. Wang, L. Xiao, J. Lu and L. Zhuang, "The comparability of Pt to Pt-Ru in Catalyzing the Hydrogen Oxidation Reaction for Alkaline Polymer Electrolyte Fuel Cells Operated at 80°C" *Angew*. *Chem*. *Int*. *Ed*. **2019**, 58, 1442.
99. N. U. Hassan, M. Mandal, G. Huang, H. A. Firouzjaie, P. A. Kohl and W. E. Mustain, "Achieving High-Performance and 2000 h Stability in Anion Exchange Membrane Fuel Cells by Manipulating Ionomer Properties and Electrode Optimization" *Adv*. *Energy Mater*. **2020**, 10, 2001986.
100. H. Adabi, A. Shakouri, N. U. Hassan, J. R. Varcoe, B. Zulevi, A. Serov, J. R. Regalbuto and W. E. Mustain, "High-performing commercial Fe–N–C cathode electrocatalyst for anion-exchange membrane fuel cells" *Nat*. *Energy* **2021**, 6, 834.
101. K. Develos-Bagarinao, T. Ishiyama, H. Kishimoto, H. Shimada and K. Yamaji, "Nanoengineering of cathode layers for solid oxide fuel cells to achieve superior power densities" *Nat*. *Commun*. **2021**, 12, 3979.
102. J. S. Ahn, D. Pergolesi, M. A. Camaratta, H. Yoon, B. W. Lee, K. T. Lee, D. W. Jung, E. Traversa and E. D. Wachsman, "High-performance bilayered electrolyte intermediate temperature solid oxide fuel cells" *Electrochem*. *Commun*. **2009**, 11, 1504.
103. J. H. Park, S. M. Han, K. J. Yoon, H. Kim, J. Hong, B. K. Kim, J. H. Lee and J. W. Son, "Impact of nanostructured anode on low-temperature performance of thin-film-based anode-supported solid oxide fuel cells" *J*. *Power Sources* **2016**, 315, 324.
104. Y. Chen, Y. Lin, Y. Zhang, S. Wang, D. Su, Z. Yang, M. Han and F. Chen, "Low temperature solid oxide fuel cells with hierarchically porous cathode nano-network" *Nano Energy* **2014**, 8, 25.
105. Y. Mizutani, K. Hisada, K. Ukai, H. Sumi, M. Yokoyama, Y. Nakamura and O. Yamamoto, "From rare earth doped zirconia to 1kW solid oxide fuel cell system" *J*. *Alloys Compd*. **2006**, 408–412, 518.
106. A. A. Solovyev, A. V. Shipilova, I. V. Ionov, A. N. Kovalchuk, S. V. Rabotkin and V. O. Oskirko, "Magnetron-Sputtered YSZ and CGO electrolyte for SOFC" *J*. *Electron*. *Mater*. **2016**, 45, 3921.
107. D. H. Myung, J. Hong, K. Yoon, B. K. Kim, H. W. Lee, J. H. Lee and J. W. Son, "The effect of an ultra-thin zirconia blocking layer on the performance of a 1-μm-thick gadolinia-doped ceria electrolyte solid-oxide fuel cell" *J*. *Power Sources* **2012**, 206, 91.
108. S. Park, S. Choi, J. Shin and G. Kim, "A collaborative study of sintering and composite effects for a $PrBa_{0.5}Sr_{0.5}Co_{1.5}Fe_{0.5}O_{5+\delta}$ IT-SOFC cathode" *RSC Adv*. **2014**, 4, 1775.
109. Q. L. Liu, K. A. Khor and S. H. Chan, "High-performance low-temperature solid oxide fuel cell

with novel BSCF cathode" *J. Power Sources* **161** (2006) 123.

110. P. V. Dollen and S. Barnett, "A study of Screen Printed Yttria-Stabilized Zirconia Layers for Solid Oxide Fuel Cells" *J. Am. Ceram. Soc.* **2005**, 88, 3361.

111. Z. Gao, D. Kennouche and S. A. Barnett, "Reduced-temperature firing of solid oxide fuel cells with zirconia/ceria bi-layer electrolytes" *J. Power Sources* **2014**, 260, 259.

112. M. B. Choi, B. Singh, E. D. Wachsman and S. J. Song, "Performance of $La_{0.1}Sr_{0.9}Co_{0.8}Fe_{0.2}O_{3-\delta}$ and $La_{0.1}Sr_{0.9}Co_{0.8}Fe_{0.2}O_{3-\delta}$–$Ce_{0.9}Gd_{0.1}O_2$ oxygen electrodes with $Ce_{0.9}Gd_{0.1}O_2$ barrier layer in reversible solid oxide fuel cells" *J. Power Sources* **2013**, 239, 361.

113. Z. Jiang, L. Zhang, L. Cai and C. Xia, "Bismuth oxide-coated (La,Sr)MnO_3 cathodes for intermediate temperature solid oxide fuel cells with yttria-stabilized zirconia electrolytes" *Electrochimica Acta* **2009**, 54, 3059.

114. J. S. Cronin, Y. K. Chen-Wiegart, J. Wang, S. A. Barnett, "Three-dimensional reconstruction and analysis of an entire solid oxide fuel cell by full-field transmission X-ray microscopy" *J. Power Sources* **2013**, 233, 174.

115. S. Choi, S. Yoo, J. Kim, S. Park, A. Jun, S. Sengodan, J. Kim, J. Shin, H. Y. Jeong, Y. M. Choi, G. Kim and M. Liu, "Highly efficient and robust cathode materials for low-temperature solid oxide fuel cells: $PrBa_{0.5}Sr_{0.5}Co_{2-x}Fe_xO_{5+\delta}$" *Sci. Rep.* **2013**, 3, 2426.

116. J. G. Lee, J. H. Park and Y. G. Shul, "Tailoring gadolinium-doped ceria-based solid oxide fuel cells to achieve 2 W cm^{-2} at 550 °C" *Nat. Commun.* **2014**, 5, 4045.

117. J. V. Herle, R. Ihringer, N. M. Sammes, G. Tompsett, K. Kendall, K. Yamada, C. Wen, T. Kawada, M. Ihara and J. Mizusaki, "Concept and technology of SOFC for electric vehicles" *Solid State Ionics* **2000**, 132, 333.

118. C. Xia and M. Liu, "Low-temperature SOFCs based on $Gd_{0.1}Ce_{0.9}O_{1.95}$ fabricated by dry pressing" *Solid State Ionics* **2001**, 144, 249.

119. Y. J. Leng, S. H. Chan, S. P. Jiang and K. A. Khor, "Low-temperature SOFC with thin film GDC electrolyte prepared in situ by solid-state reaction" *Solid State Ionics* **2004**, 170, 9.

120. C. Duan, D. Hook, Y. Chen, J. Tong and R. O'Hayre, "Zr and Y co-doped perovskite as a stable, high performance cathode for solid oxide fuel cells operating below 500 °C" *Energy Environ. Sci.* **2017**, 10, 176.

121. M. Li, M. Zhao, F. Li, W. Zhou, V. K. Peterson, X. Xu, Z. Shao, I. Gentle and Z. Zhu, "A niobium and tantalum co-doped perovskite cathode for solid oxide fuel cells operating below 500 °C" *Nat. Commun.* **2017**, 8, 13990.

122. S. S. Shin, J. H. Kim, K. T. Bae, K. T. Lee, S. M. Kim, J. W. Son, M. Choi and H. Kim, "Multiscale structured low-temperature solid oxide fuel cells with 13 W power at 500 °C" *Energy*

Environ. *Sci*. **2020**, 13, 3459.

123. C. Xia and M. Liu, "Novel Cathodes for Low-Temperature Solid Oxide Fuel Cells" *Adv*. *Mater*. **2002**, 14, 521.

124. X. Zhang, M. Robertson, S. Yuck, C. Deces-Petit, E. Styles, W. Qu, Y. Xie, R. Hui, J. Roller, O. Kesler, R. Maric and D. Ghosh, "$Sm_{0.5}Sr_{0.5}CoO_3$ + $Sm_{0.2}Ce_{0.8}O_{1.9}$ composite cathode for cermet supported thin $Sm_{0.2}Ce_{0.8}O_{1.9}$ electrolyte SOFC operating below 600 °C" *J*. *Power Sources* **2006**, 160, 1211.

125. Z. Shao and S. M. Haile, "A high-performance cathode for the next generation of solid-oxide fuel cells" *Nature* **2004**, 431, 170.

126. H. S. Noh, K. J. Yoon, B. K. Kim, H. J. Je, H W. Lee, J. H. Lee and J. W. Son, "Thermo-mechanical stability of multi-scale-architectured thin-film-based solid oxide fuel cells assessed by thermal cycling tests" *J*. *Power Sources* **2014**, 249, 125.

127. M. Liu, D. Ding, Y. Bai, T. He and M. Liu, "An Efficient SOFC Based on Samaria-Doped Ceria (SDC) Electrolyte" *J*. *Electrochem*. *Soc*. **2012**, 159, B661.

128. K. J. Kim, S. W. Choi, M. Y. Kim, M. S. Lee, Y. S. Kim and H. S. Kim, "Fabrication characteristics of SOFC single cell with thin LSGM electrolyte via tape-casting and co-sintering" *J*. *Ind*. *Eng*. *Chem*. **2016**, 42, 69.

129. Z. Bi, B. Yi, Z. Wang, Y. Dong, H. Wu, Y. She and M. Cheng, "A high-Performance Anode-Supported SOFC with LDC-LSGM Bilayer Electrolytes" *Electrochem*. *Solid-State Lett*. **2004**, 7, A105.

130. H. Orui, K. Watanabe, R. Chiba and M. Arakawa, "Application of $LaNi(Fe)O_3$ as SOFC Cathode" *J*. *Electrochem*. *Soc*. **2004**, 151, A1412.

131. D. W. Joh, J. H. Park, D. Kim, E. D. Wachsman and K. T. Lee, "Functionally Graded Bismuth Oxide/Zirconia Bilayer Electrolytes for High-Performance Intermediate-Temperature Solid Oxide Fuel Cells (IT-SOFCs)" *ACS Appl*. *Mater*. *Interfaces* **2017**, 9, 8443.

132. Z. Lu, X. Zhou, D. Fisher, J. Templeton, J. Stevenson, N. Wu and A. Ignatiev, "Enhanced performance of an anode-supported YSZ thin electrolyte fuel cell with a laser-deposited $Sm_{0.2}Ce_{0.8}O_{1.9}$ interlayer" *Electrochem*. *Commun*. **2010**, 12, 179.

133. R. J. Milcarek, K. Wang, M. J. Garrett and J. Ahn, "Performance Investigation of Dual Layer Yttria-Stabilized Zirconia-Samaria-Doped Ceria Electrolyte for Intermediate Temperature Solid Oxide Fuel Cells" *J*. *Electrochem*. *En*. *Conv*. *Stor*. **2016**, 13, 011002.

134. J. Li, S. Wang, Z. Wang, J. Qian, R. Liu, T. Wen and Z. Wen, "Effect of the cathode structure on the electrochemical performance of anode-supported solid oxide fuel cells" *J*. *Solid State Electrochem*. **2010**, 14, 579.

135. N. Ai, M. Chen, S. He, K. Chen, T. Zhang and S. P. Jiang, “High performance nanostructured bismuth oxide–cobaltite as a durable oxygen electrode for reversible solid oxide cells” *J. Mater. Chem. A* **2018**, 6, 6510.

136. W. Wu, X. Wang, Z. Liu, Z. Zhao, D. Ou, B. Tu and M. Cheng, “Influence of Deposition Temperature of GDC Interlayer Deposited by RF Magnetron Sputtering on Anode-Supported SOFC” *Fuel Cells* **2014**, 14, 171.

137. M. Chen, Y. Cheng, S. He, N. Ai, J. P. Veder, W. D. A. Rickard, M. Saunders, K. Chen, T. Zhang and S. P. Jiang, “Active, durable bismuth oxide-manganite composite oxygen electrodes: Interface formation induced by cathodic polarization” *J. Power Sources* **2018**, 397, 16.

138. S. L. Zhang, H. Wang, M. Y. Lu, A. P. Zhang, L. V. Mogni, Q. Liu, C. X. Li, C. J. Li and S. A. Barnett, “Cobalt-substituted $SrTi_{0.3}Fe_{0.7}O_{3-\delta}$: a stable high-performance oxygen electrode material for intermediate-temperature solid oxide electrochemical cells” *Energy Environ. Sci.* **2018**, 11, 1870.

139. T. Ishihara, “Low Temperature Solid Oxide Fuel Cells Using $LaGaO_3$-based Oxide Electrolyte on Metal Support” *J. Jpn. Petrol. Inst.* **2015**, 58, 71.

140.B. H. Yun, K. J. Kim, D. W. Joh, M. S. Chae, J. J. Lee, D. W. Kim, S. Kang, D. Choi, S. T. Hong and K. T. Lee, “Highly active and durable double-doped bismuth oxide-based oxygen electrodes for reversible solid oxide cells at reduced temperatures” *J. Mater. Chem. A* **2019**, 7, 20558.

141. E. O. Oh, C. M. Whang, Y. R. Lee, S. Y. Park, D. H. Prasad, K. J. Yoon, J. W. Son, J. H. Lee and H. W. Lee, “Extremely Thin Bilayer Electrolyte for Solid Oxide Fuel Cells (SOFCs) Fabricated by Chemical Solution Deposition (CSD)” *Adv. Mater.* **2012**, 24, 3373.

142. Z. Gao, V. Y. Zenou, D. Kennouche, L. Marks and S. A. Barnett, “Solid oxide cells with zirconia/ceria Bi-Layer electrolytes fabricated by reduced temperature firing” *J. Mater. Chem. A* **2015**, 3, 9955.

143. J. An, Y. B. Kim, J. Park, T. M. Gur and F. B. Prinz, “Three-Dimensional Nanostructured Bilayer Solid Oxide Fuel Cell with 1.3 W/cm^2 at 450 °C” *Nano Lett.* **2013**, 13, 4551.

144. C. C. Chao, C. M. Hsu, Y. Cui and F. B. Prinz, “Improved Solid Oxide Fuel Cell Performance with Nanostructured Electrolytes” *ACS Nano* **2011**, 5, 5692.

145. P. C. Su, C. C. Chao, J. H. Shim, R. Fasching and F. B. Prinz, “Solid Oxide Fuel Cell with Corrugated Thin Film Electrolyte” *Nano Lett.* **2008**, 8, 2289.

146. H. Huang, M. Nakamura, P. Su, R. Fasching, Y. Saito and F. B. Prinz, “High-Performance Ultrathin Solid Oxide Fuel Cells for Low-Temperature Operation” *J. Electrochem. Soc.* **2007**, 154, B20.

147. A. Evans, J. Martynczuk, D. Stender, C. W. Schneider, T. Lippert and M. Prestat, “Low-Temperature Micro-Solid Oxide Fuel Cells with Partially Amorphous $La_{0.6}Sr_{0.4}CoO_{3-\delta}$ Cathodes”

Adv. *Energy Mater*. **2015**, 5, 1400747.

148. X. Gang, L. Qingfeng, H. A. Hjuler and N. J. Bjerrum, "Hydrogen Oxidation on Gas Diffusion Electrodes for Phosphoric Acid Fuel Cells in the Presence of Carbon Monoxide and Oxygen" *J. Electrochem*. *Soc.* **1995**, 142, 2890.

149. Q. Li, R. He, J. A. Gao, J. O. Jensen and N. J. Bjerrum, "The CO poisoning Effect in PEMFCs Operational at Temperatures up to 200°C" *J. Electrochem*. *Soc*. **2003**, 150, A1599.

150. S. T. Thompson, D. Peterson, D. Ho and D. Papageorgopoulos, "Perspective—The Next Decade of AEMFCs: Near-Term Targets to Accelerate Applied R&D" *J. Electrochem*. *Soc*. **2020**, 167, 084514.

151. J. R. Varcoe and R. C. Slade, "Prospects for Alkaline Anion-Exchange Membranes in Low Temperature Fuel Cells" *Fuel Cells* **2005**, 5, 187.

152. B. Y. S. Lin, D. W. Kirk and S. J. Thorpe, "Performance of alkaline fuel cells: A possible future energy system?" *J. Power Sources* **2006**, 161, 474.

153. M. Mandal, "Recent Advancement on Anion Exchange Membranes for Fuel Cell and Water Electrolysis" *ChemElectroChem* **2020**, 7, 1.

154. J. D. Baek, C. C. Yu and P. C. Su, "A Silicon-Based Nanothin Film Solid Oxide Fuel Cell Array with Edge Reinforced Support for Enhanced Thermal Mechanical Stability" *Nano Lett*. **2016**, 16, 2413.

155. M. Tsuchiya, B. K. Lai and S. Ramanathan, "Scalable nanostructured membranes for solid-oxide fuel cells" *Nat*. *Nanotech*. **2011**, 6, 282.

156. J. Hyodo, K. Tsujikawa, M. Shiga, Y. Okuyama and Y. Yamazaki, "Accelerated Discovery of Proton-Conducting Perovskite Oxide by Capturing Physicochemical Fundamentals of Hydration" *ACS Energy Lett*. **2021**, 6, 2985

157. K. D. Kreuer, "Proton-Conducting Oxides" *Annu*. *Rev*. *Mater*. *Res*. **2003**, 33, 333.

158. L. Yang, S. Wang, K. Blinn, M. Liu, Z. Liu, Z. Cheng and M. Liu, "Enhanced Sulfur Coking Tolerance of a Mixed Ion Conductor for SOFCs: $BaZr_{0.1}Ce_{0.7}Y_{0.2-x}Yb_xO_{3-\delta}$" *Science* **2009**, 326, 126.

159. C. Zuo, S. Zha, M. Liu, M. Hatano and M. Uchiyama, "$Ba(Zr_{0.1}Ce_{0.7}Y_{0.2})O_{3-\delta}$ as an Electrolyte for Low-Temperature Solid-Oxide Fuel Cells" *Adv. Mater*. **2006**, 18, 3318.

160. H. An, H. W. Lee, B. K. Kim, J. W. Son, K. J. Yoon, H. Kim, D. Shin, H. I. Ji and J. H. Lee, "A 5 × 5 cm^2 protonic ceramic fuel cell with a power density of 1.3 W cm^{-2} at 600 °C" *Nat*. *Energy* **2018**, 3, 870.

161. K. J. Albrecht, C. Duan, R. P. O'Hayre and R. J. Braun, "Modeling Intermediate Temperature Protonic Ceramic Fuel Cells" *ECS Trans*. **2015**, 68, 3165.

162. C. Duan, R. J. Kee, H. Zhu, C. Karakaya, Y. Chen, S. Ricote, A. Jarry, E. J. Crumlin, D. Hook, R. Braun, N. P. Sullivan and R. O'Hayre, "Highly durable, coking and sulfur tolerant, fuel-flexible

protonic ceramic fuel cells" *Nature* **2018**, 557, 217.

163. X. Li, M. Liu, S. Y. Lai, D. Ding, M. Gong, J. P. Lee, K. S. Blinn, Y. Bu, Z. Wang, L. A. Bottomley, F. M. Alamgir and M. Liu, "In Situ Probing of the Mechanisms of Coking Resistance on Catalyst-Modified Anodes for Solid Oxide Fuel Cells" *Chem*. *Mater*. **2015**, 27, 822.

164. S. H. Nien, C. S. Hsu, C. L. Chang and B. H. Hwang, "Preparation of $BaZr_{0.1}Ce_{0.7}Y_{0.2}O_{3-\delta}$ Based Solid Oxide Fuel Cells with Anode Functional Layers by Tape Casting" *Fuel Cells* **2011**, 11, 178.

165. S. Choi, C. J. Kucharczyk, Y. Liang, X. Zhang, I. Takeuchi, H. I. Ji and S. M. Haile, "Exceptional power density and stability at intermediate temperatures in protonic ceramic fuel cells" *Nat*. *Energy* **2018**, 3, 202.

166. C. Xia, Y. Mi, B. Wang, B. Lin, G. Chen and B. Zhu, "Shaping triple-conducting semiconductor $BaCo_{0.4}Fe_{0.4}Zr_{0.1}Y_{0.1}O_{3-\delta}$ into an electrolyte for low-temperature solid oxide fuel cells" *Nat*. *Commun*. **2019**, 10, 1707.

167. W. Bian, W. Wu, Y. Gao, J. Y. Gomez, H. Ding, W. Tang, M. Zhou and D. Ding, "Regulation of Cathode Mass and Charge Transfer by Structural 3D Engineering for Protonic Ceramic Fuel Cell at 400 °C" *Adv*. *Funct. Mater*. **2021**, 31, 2102907.

168. M. Choi, J. Paik, D. Kim, D. Woo, J. Lee, S. J. Kim, J. Lee and W. Lee, "Exceptionally high performance of protonic ceramic fuel cells with stoichiometric electrolytes" *Energy Environ*. *Sci*. **2021**, in press.

169. R. Zohourian, R. Merkle, G. Raimondi and J. Maier, "Mixed-Conducting Perovskites as Cathode Materials for Protonic Ceramic Fuel Cells: Understanding the Trends in Proton Uptake" *Adv*. *Funct*. *Mater*. **2018**, 28, 1801241.

170. N. Ito, M. Iijima, K. Kimura and S. Iguchi, "New intermediate temperature fuel cell with ultra-thin proton conductor electrolyte" *J*. *Power Sources* **2005**, 152, 200.

171. K. Katahira, Y. Kohchi, T. Shimura, H. Iwahara, "Protonic conduction in Zr-substituted $BaCeO_3$" *Solid State Ionics* **2000**, 138, 91.

172. P. Sawant, S. Varma, B. N. Wani and S. R. Bharadwaj, "Synthesis, stability and conductivity of $BaCe_{0.8-x}Zr_xY_{0.2}O_{3-\delta}$ as electrolyte for proton conducting SOFC" *Int*. *J*. *Hydrogen Energy* **2012**, 37, 3848.

173. E. Fabbri, A. D'Epifanio, E. D. Bartolomeo, S. Licoccia and E. Traversa, "Tailoring the chemical stability of $Ba(Ce_{0.8-x}Zr_x)Y_{0.2}O_{3-\delta}$ protonic conductors for Intermediate Temperature Solid Oxide Fuel Cells (IT-SOFCs)" *Solid State Ionics* **2008**, 179, 558.

174. S. B. C. Duval, P. Holtappels, U. F. Vogt, U. Stimming, T. Graule, "Characterization of $BaZr_{0.9}Y_{0.1}O_{3-\delta}$ Prepared by Different Synthesis Methods: Study of the Sinterability and the Conductivity" *Fuel Cells* **2009**, 9, 613.

175. S. M. Haile, G. Staneff and K. H. Ryu, “Non-stoichiometry, grain boundary transport and chemical stability of proton conducting perovskites” *J. Mater. Sci.* **2001**, 36, 1149.
176. E. Fabbri, D. Pergolesi and E. Traversa, “Materials challenges toward proton-conducting oxide fuel cells: a critical review” *Chem. Soc. Rev.* **2010**, 39, 4355.

Chapter 2

Fabrication of porous-anode-support-type fuel cells (PAFCs) with Zr-rich side $BaZr_xCe_{0.8-x}Y_{0.2}O_{3-\delta}$ electrolyte thin films

2.1. Objective of chapter 2

As presented in the chapter 1, it is hard to fabricate protonic ceramic fuel cells (PCFCs) with Zr-rich side $BaZr_xCe_{0.8-x}Y_{0.2}O_{3-\delta}$ electrolytes due to their high refractory nature. The objective of this chapter is to fabricate highly efficient porous-anode-support-type fuel cells (PAFCs) with large-grained electrolyte films using high Zr-content $BaZr_xCe_{0.8-x}Y_{0.2}O_{3-\delta}$ (BZCY; $x \geq 0.4$) under moderate sintering conditions.

In many scientific studies, wet chemical processes, such as co-precipitation and combustion methods, were employed to prepare fine green powders of $BaZr_xCe_{0.8-x}Y_{0.2}O_{3-\delta}$, whereas such powders did not lead to the highly dense ceramics with more than 90% relative density by sintering at temperatures below 1500°C, especially, for $x > 0.4$.[1] Recently, Duan *et al*. have developed a significantly simplified and cost-effective solid-state reactive sintering (SSRS) method to fabricate thin film electrolyte PAFC with $BaZr_{0.1}Ce_{0.7}Y_{0.1}Yb_{0.1}O_3$ (BZCYYb).[2] In the SSRS process, phase formation, densification and grain growth were conducted at a single high-temperature sintering step, and the resultant electrolyte films were significantly densified despite lower (200–400 °C) sintering temperatures compared with the observations of the conventional process.[3] The resultant cells could

conduct efficient power generation even at 500 °C.[2] In this chapter, I successfully fabricated thin film PAFCs based on high Zr-content $BaZr_xCe_{0.8-x}Y_{0.2}O_{3-\delta}$ (x = 0.4, 0.6, 0.7 and 0.8) electrolytes (~30 μm thickness) by modifying the SSRS method with a single sintering step at 1400 °C. $BaZr_{0.6}Ce_{0.2}Y_{0.2}O_{3-\delta}$-based cells achieved the highest power output among the four studied cells, which was due to the superior proton conductivity at elevated temperatures; they were also highly tolerant to CO_2 due to the relatively high fraction of the thermodynamically stable zirconates, which demonstrated that $BaZr_{0.6}Ce_{0.2}Y_{0.2}O_{3-\delta}$ is a promising electrolyte for protonic ceramic fuel cells.

2.2. Experimental

2.2.1. Fabrication of PAFCs

The PAFCs were fabricated by SSRS of green pellets with alternative $Zn(NO_3)_2$ sintering aids instead of commonly used NiO aids.[2,4–5] The fabrication process is schematically represented in **Figure 2-1**. Precursor powders of $BaZr_xCe_{0.8-x}Y_{0.2}O_{3-\delta}$ (x = 0.4, 0.6, 0.7 and 0.8) were prepared by mixing stoichiometric amounts of starting materials: $BaCO_3$ (High Purity Chemicals, 99.95%), CeO_2 (High Purity Chemicals, 99.99%), ZrO_2 (High Purity Chemicals, 98%) and Y_2O_3 (High Purity Chemicals, 99.99%) with addition of 3.56% of $Zn(NO_3)_2 \cdot 6H_2O$ as a sintering aid. The mixtures were ball-milled in ethanol for 24 h and subsequently dried at 80°C; thus, precursor powders of $BaZr_xCe_{0.8-x}Y_{0.2}O_{3-\delta}$ (denoted as Pre-1 hereafter) were obtained. For Ni/$BaZr_xCe_{0.8-x}Y_{0.2}O_{3-\delta}$ anode supports, Pre-1 and NiO were blended at a weight ratio of 40 : 60 in ethanol and ball-milled for 48 h.

The obtained mixed powders were uniaxially pressed into green pellets (12 mm ϕ, 1.2 mm *d*) under 20 MPa and subsequently pressed under a hydrostatic pressure of 100 MPa in an isostatic press. The precursor layers of electrolyte films were spin-coated on the green pellets by using a MISAKA 1H-D7 spin-coater. The sols were prepared by dispersing Pre-1 in a solution containing dispersant (20 wt.% polyethyleneimine (M_w 28000) dissolved in α-terpineol) and binder (5 wt.% surfactant dissolved in α-terpineol) at a weight ratio of 10 : 3 : 1, and they were spin-coated on the surfaces of the green pellets at 3000 rpm for 40 s. After spin coating, the pellets were dried at room temperature and co-fired at 1400 °C for 8 h, 12 h, 12h and 18 h for x = 0.4, 0.6, 0.7 and 0.8, respectively, in air. The pellets were highly densified by sintering, which resulted in a compact ceramic disc with *ca*. 9 mm ϕ × 1 mm *d*.

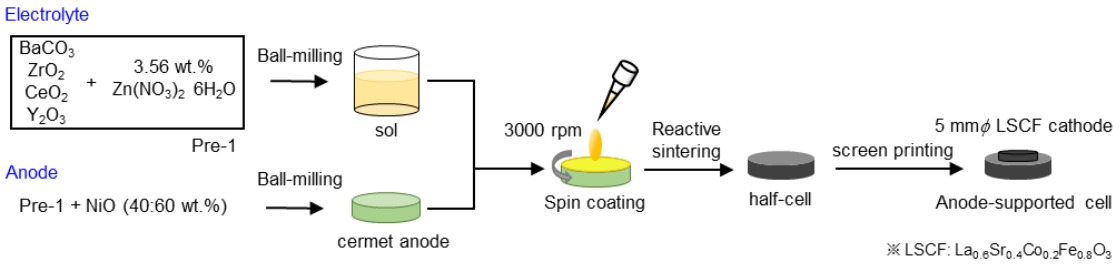

Figure 2-1. The schematic diagram for SSRS fabrication of anode-supported cells.

The back sections of the sintered discs were polished with 1000 SiC abrasive sandpapers and then, Pt paste was applied as a current collector attached with a gold wire (0.1 mm ϕ). Finally, $La_{0.6}Sr_{0.4}Co_{0.2}Fe_{0.8}O_{3-\delta}$ (LSCF) button electrode (5 mm ϕ) was deposited on the other side as a porous

cathode by screen-printing with a commercial LSCF paste (Fuelcellmaterials) and post-annealing at 700°C. Pt mesh was used as a current collector of the cathode.

Bulk ceramics for conductivity measurements of $BaZr_xCe_{0.8-x}Y_{0.2}O_{3-\delta}$ (x = 0.4 and 0.6) were prepared by the similar SSRS process. Pre-1 powders were uniaxially pressed into green pellets (12 mm ϕ, 1.2 mm d) under 20 MPa and subsequently pressed under hydrostatic pressure of 100 MPa in an isostatic press. The pellets, thus prepared, were reactive-sintered at 1400 °C for 8 or 12 h in air. Both faces of the sintered disc were polished by a SIC paper and then was applied with Pt paste as a current collector.

The phase purity was checked by X-ray diffraction (XRD) analysis in the 2θ range between 10^o and 80^o at a scan rate of 5^o min^{-1} using Rigaku Ultima IV (CuKα radiation). For the XRD measurements, the cells before screen-printing LSCF layer were pulverized in a mortar. The microstructures of the fabricated cells were examined by using a field emission scanning electron microscope (FESEM; SIGMA500, ZEISS). The composition of the electrolytes was evaluated by energy-dispersive X-ray analysis (EDX; JEOL-S100).

2.2.2. Electrochemical assessment of a single cell

A single cell, thus prepared, was mounted in a lab-constructed fuel cell test station. The cathode compartment was sealed by a molten glass ring gasket. Before fuel cell tests, the cathode side was exposed to humidified Ar gases, and the anode side was exposed to humidified 10%-H_2/Ar mix gases at 700 °C for 1 h to convert NiO to metallic Ni; thus, a porous Ni/$BaZr_xCe_{0.8-x}Y_{0.2}O_{3-\delta}$ cermet anode

was prepared. All humidified gases were prepared by bubbling in Milli-Q deionized water at room temperature at a flow rate of 50 sccm, such that the corresponding water partial pressure (p_{H_2O}) equaled 3 kPa. For fuel cell tests, humidified hydrogen was fed to anode, and humidified air was supplied to the cathode side at a rate of 50 sccm. The electrochemical performances of the cells were evaluated in the temperature range of 550–700 °C. Impedance spectroscopy was conducted with a Solartron 1260A frequency response analyzer implemented with a Solartron 1287 potentiostat in the frequency range of 10^6 to 0.1 Hz with ac amplitude of 30 mV under OCV condition. Current–voltage (*I–V*) and current–power (*I–P*) characteristics were recorded on the same apparatus. CO_2 durability tests were performed by monitoring the current outputs under potentiostatic conditions while feeding 1%-CO_2/H_2 mixed gases to the anode for 2 days.

2.3. Results and discussion

2.3.1. Material characterization

Hereafter, $BaZr_xCe_{0.8-x}Y_{0.2}O_{3-\delta}$ with x = 0.4, 0.6, 0.7 and 0.8 are denoted as BZCY4, BZCY6, BZCY7 and BZY, respectively. **Figure 2-2** represents the powder X-ray diffraction(XRD) patterns of the pulverized thin film fuel cells without screen-printing LSCF cathodes; the main peaks are assigned to NiO and $BaZr_xCe_{0.8-x}Y_{0.2}O_{3-\delta}$ for all x. The peaks of $BaZr_xCe_{0.8-x}Y_{0.2}O_{3-\delta}$ shift to high 2θ angle with the increasing x while is due to lattice contraction by the substitution of Ce^{4+} (0.87 Å) with smaller Zr^{4+} (0.72 Å).[6] BZCY4 does not contain any secondary impurity phases whereas BZCY6,

BZCY7 and BZY show a small impurity peak in the vicinity of 32.5°, which is due to the formation of BaY_2NiO_5 (PDF 00-041-0463). It has been reported that such a secondary phase is readily formed by the reaction between BZY and NiO through high-temperature sintering.[4,5,7,8] Therefore, the absence of BaY_2NiO_5 impurity phase in BZCY4 is probably due to the low reactivity of $BaCeO_3$ against NiO. EDX analysis confirms that Ba/Zr/Ce/Y molar ratios in all electrolytes are very close to the target ones, indicating that the vaporization of Ba is minimal in our fabrication process.

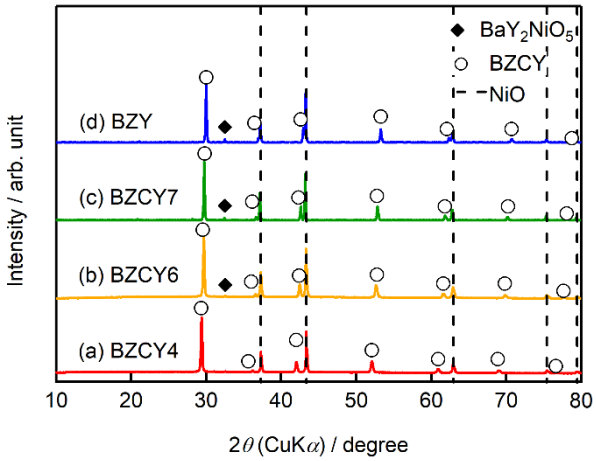

Figure 2-2. XRD patterns of the thin film fuel cells based on (a) BZCY4, (b) BZCY6 (c) BZCY7 and (d) BZY electrolytes prepared by SSRS process shown in Figure 1. For the measurements, the sintered sample is pulverized without screen-print of LSCF.

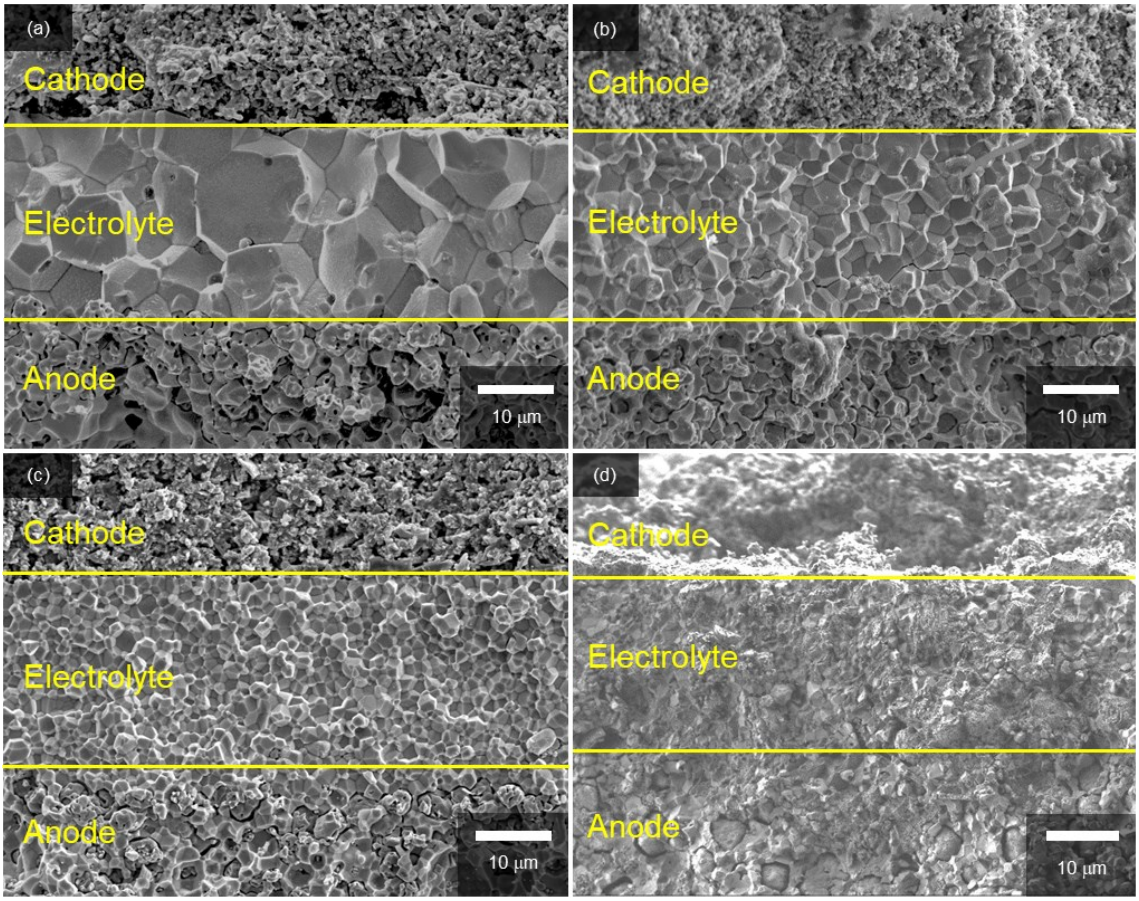

Figure 2-3. Cross-section SEM micrographs of PAFCs with (a) BZCY4, (b) BZCY6, (c) BZCY7 and (d) BZY electrolytes.

Figure 2-3 shows SEM images of the cross-sections of PAFCs after fuel cell tests; all cells comprise three layers: porous LSCF cathodes, dense $BaZr_xCe_{0.8-x}Y_{0.2}O_{3-\delta}$ electrolyte films and porous Ni/$BaZr_xCe_{0.8-x}Y_{0.2}O_{3-\delta}$ cermet anode supports. The recent PAFCs use an electrolyte-electrode composite for the cathode to reduce the cathodic interfacial overpotentials with extended gas–electron–proton triple phase boundaries.[2] In this study, however, a single phase LSCF paste is used as a well-defined cathode in all cells because the objective of this study is to clarify optimal Zr contents of $BaZr_xCe_{0.8-x}Y_{0.2}O_{3-\delta}$ electrolytes to obtain satisfactorily high fuel cell efficiency and

excellent CO_2 tolerance simultaneously.

In every case, dense electrolyte films with 30 μm thickness are uniformly formed over a wide area of porous anode supports without apparent cracks or pinholes. The average grain sizes remarkably decreases with the increasing Zr contents. In BZCY4 electrolyte films, the oxide grains exhibit significant growth; their diameter is as large as 5–10 μm (**Figure 2-3a**). BZCY6 electrolyte films are also formed by close packing of micrometer grains although the typical grain sizes (4–6 μm) are smaller than those of BZCY4 (**Figure 2-3b**). The grain sizes of BZCY7 and BZY are much smaller than those of BZCY6 (**Figure 2-3c** and **2-3d**), i.e., they are typically less than 1 μm and thus, their films have a large volume of grain boundaries. In addition, porous precipitates are formed at the grain boundaries in the BZY electrolyte film (**Figure 2-4**), which can be identical to Ni particles formed by the reduction of BaY_2NiO_5 impurity phases under hydrogen atmosphere.[5,9] Such metallic Ni segregation is not observed in BZCY6 and BZCY7, indicating that the reaction between BZCY6 or BZCY7 and NiO is much less pronounced than with BZY.

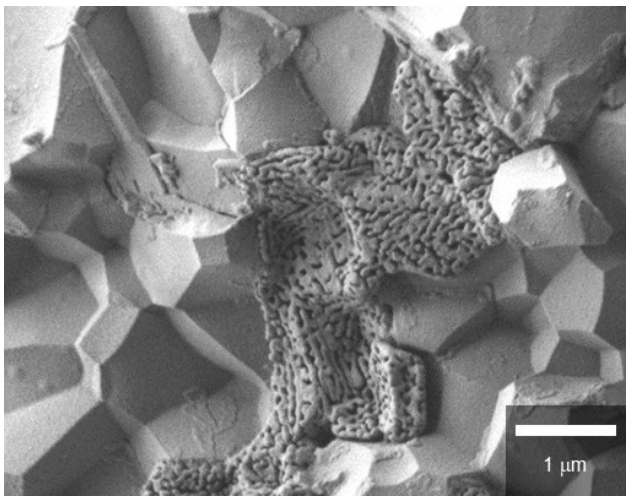

Figure 2-4. High magnification image of BZY electrolyte thin film.

2.3.2. Electrochemical performances

Figure 2-5 shows the *I–V* curves of all PAFCs along with the summary of open circuit voltages (OCVs) and peak power densities (PPDs). The BZCY4- and BZCY6-based cells exhibit sufficiently high OCVs of more than 1 V in the measured temperature range, which are close to the theoretical values, suggesting that electronic conduction and gas leakage are sufficiently small in BZCY4 and BZCY6 electrolyte thin films. Hence, the BZCY4- and BZCY6-based cells yield significantly high PPDs. The BZCY4-based cell delivers PPD values of 381, 340, 279 and 205 mW cm^{-2} at 700, 650, 600 and 550 °C, respectively (**Figure 2-5f**). Moreover, BZCY6-based cells yield higher PPDs than BZCY4 regardless of the higher Zr contents, and the values reach 435, 396, 336 and 264 mW cm^{-2} in the same temperature range (**Figure 2-5f**). However, the fuel cell performances rapidly deteriorate with further Zr substitution. PPD of the BZCY7-based cell is less than 120 mW cm^{-2} even at 600°C although the cell grains OCV of more than 1.0 V at temperatures below 650 °C. PPD of the BZY cell

is smaller than that of BZCY7, and OCVs do not reach 1.0 V even at temperatures below 600 °C, which is probably due to electronic leakage mediated *via* metallic Ni precipitates.

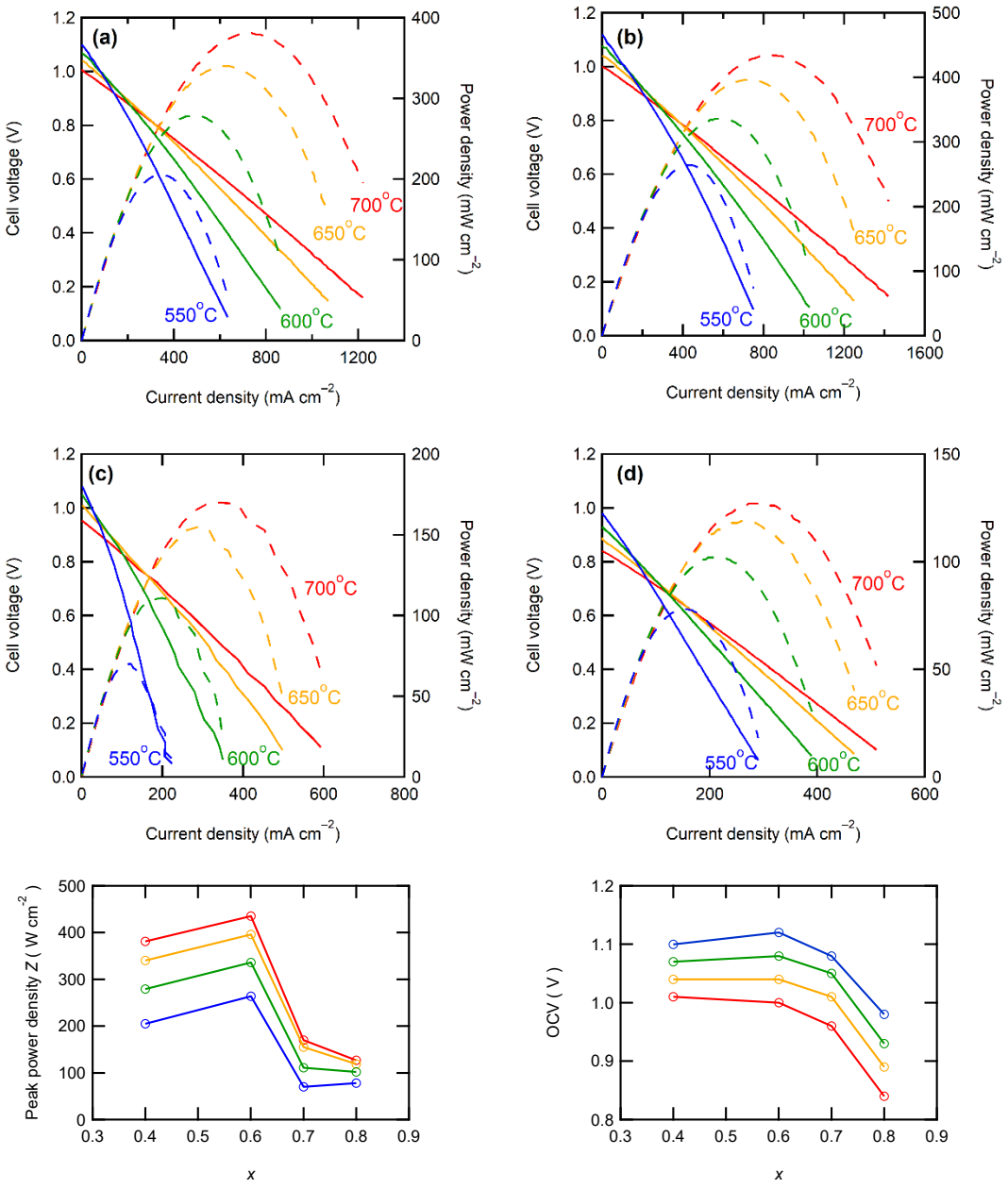

Figure 2-5. *I-V* and *I-P* curves of fabricated PAFCs consisting of (a) BZCY4, (b) BZCY6, (c) BZCY7 and (d) BZY. Solid lines show *I-V* characteristics and dashed line *I-P* characteristics. Summary of (e) peak power densities and (f) open circuit voltages.

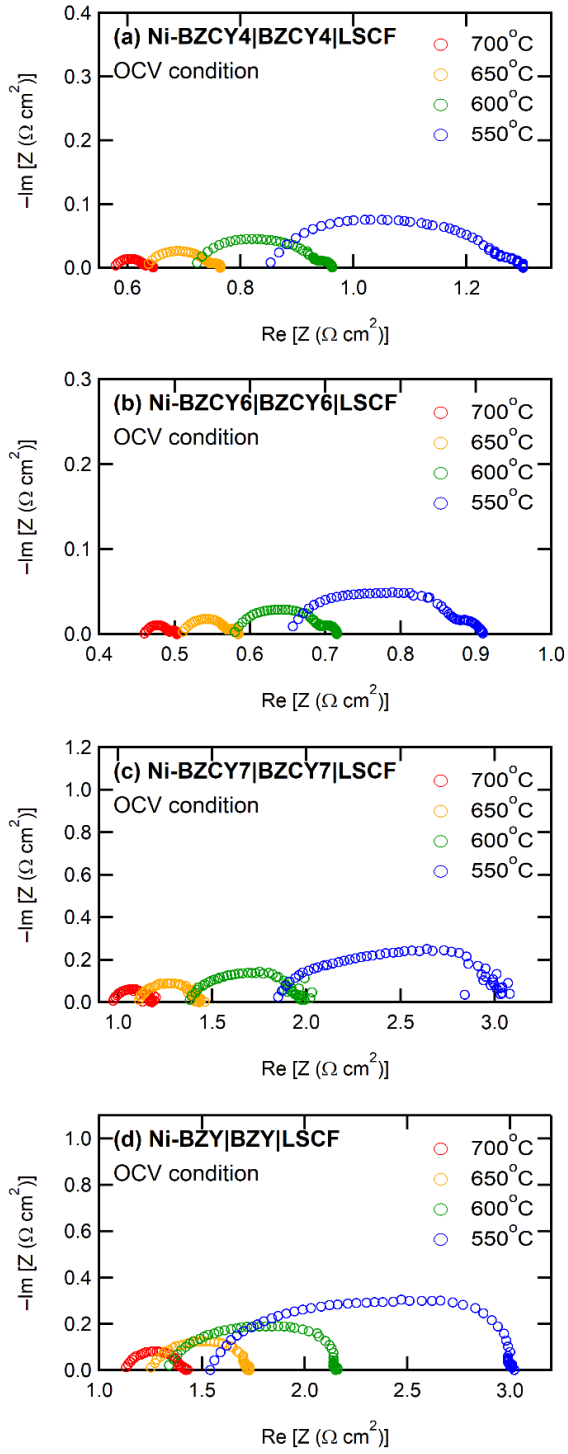

Figure 2-6. Electrochemical impedance spectra of thin film PAFCs with electrolytes of (a) BZCY4, (b) BZCY6, (c) BZCY7 and (d) BZY in fuel cell atmosphere under OCV condition.

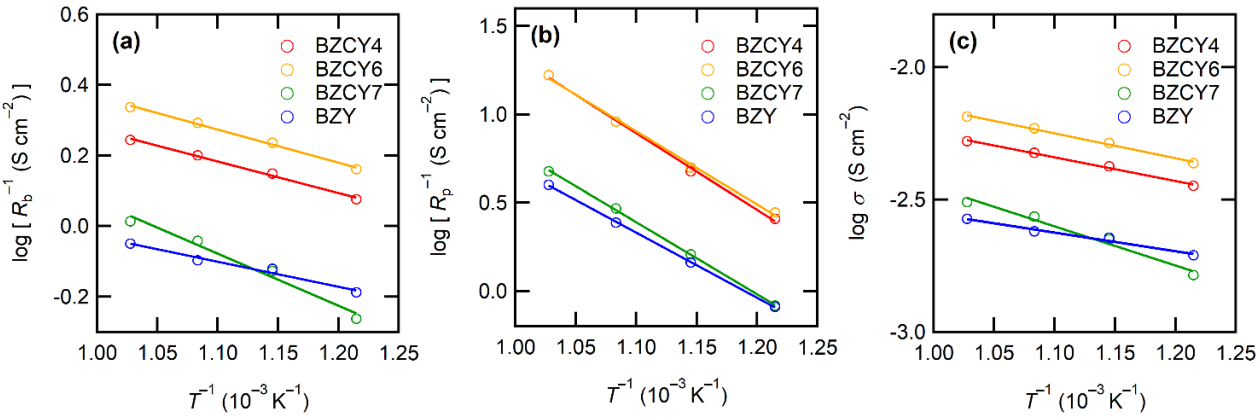

Figure 2-7. Arrhenius plots of reciprocal of (a) ohmic resistance (R_b) and (b) polarization resistance (R_p) of PAFCs. The values of R_b and R_p are determined from the features of impedance Nyquist plots in Figure 6. (c) Arrhenius plots of proton conductivity of BZCY4, BZCY6, BZCY7 and BZY electrolyte films determined from R_b and film thickness.

To provide further verification for fuel cell performances, the polarization behavior is studied by electrochemical impedance techniques. **Figure 2-6** presents the impedance spectra of the fuel cells under OCV conditions. In general, Nyquist plots of the impedance responses of PAFCs provide the *x*-intercept in a high frequency region, corresponding to electrolyte resistances. After the intercept, they exhibit broad semi-arcs mainly due to interfacial polarization resistances at the cathodic side;[10] thus, the diameters of the arcs provide polarization resistances. **Figure 2-7** display Arrhenius plot of inversed ohmic resistance (R_b) and polarization resistance (R_p) determined from the spectral features of the Nyquist impedance plots. All electrolyte-type cells show Arrhenius-type linear temperature

dependence of R_p^{-1} (**Figure 2-7b**), and the related activation energies are similar; the values are 0.94, 0.90, 0.89 and 0.81 eV for BZCY4, BZCY6, BZCY7 and BZY-based cells, respectively, which implies that the cathodic reaction involves the same rate-determining steps. R_p values of BZCY4- and BZCY6-based cells are very close each other at all temperatures, whereas R_p values of BZCY7 and BZY are one order of magnitude larger than the former values, which is probably due to their low proton conductivity,[11] as mentioned below.

R_b^{-1} obeys linear Arrhenius-type relationship, providing the activation energies of proton conduction of 0.26, 0.33, 0.34 and 0.22 eV for BZCY4, BZCY6, BZCY7 and BZY cells, respectively, and those energies are similar to the corresponding ones reported elesewhere.[12–16] In all electrolyte cells, the fractions of R_b to total resistances ($R_b + R_p$) account for 65–80% at 600°C, indicating that the electrolyte resistances involve a major part of the voltage losses. R_b values of BZCY7 and BZY electrolyte films are one order of magnitude higher than those of BZCY4 and BZCY6, which is due to large grain boundary resistances; the grain boundary volumes of the former are much larger than those of the latter (**Figure 2-3**). The BZCY6-based cell has the lowest ohmic resistance among the four cells (**Figure 2-6**), which is the main reason for obtaining the highest PPD value with the BZCY6-based cell.

The performances of recently reported PAFCs with BZCY4, BZCY6, BZCY7 and BZY electrolyte films at 600 °C are summarized in **Table 2-1** for direct comparison; most of these materials were fabricated using chemically synthesized fine powder of $BaZr_xCe_{0.8-x}Y_{0.2}O_{3-\delta}$ for sintering.[1,13–

[25] In recent years, S. Choi *et al*. reported outstanding performances of $BaZr_{0.4}Ce_{0.4}Y_{0.1}Yb_{0.1}O_{3-\delta}$-based cells with $PrBa_{0.5}Sr_{0.5}Co_{1.5}Fe_{0.5}O_{5+\delta}$ cathodic interlayer, which reached to about 1.1 W cm^{-2} at 600 °C.[26] Although PPD of our BZCY4 cells is lower than this significant result, it is higher than PPD values reported elsewhere for PAFCs with the same electrolyte (**Table 2-1**).[1,13–14,17,19] Moreover, the studies on BZCY6 cells are rather rare,[20] and PPD of our BZCY6 cells is 3 times higher than that of the analogous cell fabricated with sol–gel-derived fine powders (116 mW cm^{-2}).[20] This behavior could be related to the sufficiently low grain boundary resistances of our electrolyte films because the average grain size of our BZCY6 was larger than those of the previously reported cells (ref. 3). Although the BZCY7- and BZY-based cells prepared here possessed low fuel cell performances compared to the other two, their PPDs were higher than those of most of the analogous-electrolyte fuel cells[1,15,16,18–23] (**Table 2-1**). Moreover, PPD of our BZY cell is comparable to that reported for BZY-based thin film fuel cells fabricated by pulsed laser deposition (PLD) at 600 °C (ref. 16) (**Table 2-1**). It can be concluded that all electrolyte cells prepared here have equivalent or higher efficiencies than the corresponding high-performance fuel cells reported elsewhere. These features prove that the upper limit of Zr contents in $BaZr_xCe_{0.8-x}Y_{0.2}O_{3-\delta}$ electrolyte is near $x = 0.6$ to develop a low-resistive, large-grained electrolyte film *via* a low-temperature reactive sintering process.

Table 2-1. Summary of fuel cell performances at 600 °C for recent-reported thin film PAFC with BZCY4, BZCY6, BZY and $BaZr_{0.1}Ce_{0.7}Y_{0.1}Yb_{0.1}O_3$ (BZCYYb) electrolyte, fabricated by solid state sintering processes.

Anode	Electrolyte	Cathode	R_b / Ω cm^2	Thickness / μm	OCV /V	PPD / mW cm^{-2}	Film conductivity / S cm^{-1}	Reference
Ni-BZCY4	BZCY4	LSCF	0.71	30	1.07	279	4.2×10^{-3}	This work
Ni-BZCY6	BZCY6	LSCF	0.58	30	1.08	336	5.2×10^{-3}	This work
Ni-BZCY7	BZCY7	LSCF	1.34	30	1.05	111	2.7×10^{-3}	This work
Ni-BZY	BZY	LSCF	1.32	30	0.93	102	2.2×10^{-3}	This work
Ni-BZCY4	BZCY4	BSCF	–	20	1.04	230	–	17
Ni-BZCY4	BZCY4	BSCF	1.23	35	1.05	159	2.8×10^{-3}	1
Ni-BZCY4	BZCY4	BSCF	0.74	25	1.02	276	3.4×10^{-3}	13
Ni-BZCY4	BZCY4	BSCF	-	35	0.98	151	-	14
Ni-BZY	BZCY4	Pr_2NiO_4	0.77	5	1.03	102	6.5×10^{-4}	18
Ni-BZCY4	BZCY4	BZCY4-BSCFT	0.91	20	1.03	194	2.2×10^{-3}	19
Ni-BZCY6	BZCY6	BSCF	–	25	1.07	116	–	20
Ni-BZY	BZY	BSCF	–	35	1	22	–	1
Ni-BZI	BZI	PBC-BZPY	2.01	15	0.946	84	7.5×10^{-4}	15
Ni-BZY	BZY (PLD)	LSCF-BCYb	1.85	4	0.99	110	2.16×10^{-4}	16
Ni-BZCY	BZY	SSC-SDC	3.24	25	0.97	55	7.7×10^{-4}	21
Ni-BZY	BZYZn	Pt	1.15	20	0.94	75	1.7×10^{-3}	22
Ni-BZY	BZPY	LSCF-BZPY	1.33	20	0.93	81	1.5×10^{-3}	23
Ni-BZY	BZPY	LSCF-BZPY30	0.53	12	0.9	163	2.26×10^{-3}	24
Ni-BZCYYb (SSRS)	BZCYYb	BCFZY	0.29	30	1.1	660	1.0×10^{-2}	2
Ni-BZCYYb 4411	BZCYYb 4411	PBSCF	0.08	15	1.03	1098	1.88×10^{-2}	26

Note: $La_{0.6}Sr_{0.4}Co_{0.2}Fe_{0.8}O_3$ (LSCF), $Ba_{0.5}Sr_{0.5}Co_{0.8}Fe_{0.2}O_3$ (BSCF), $La_{0.6}Sr_{0.4}CoO_3$ (LSC),

$Ba_{0.5}Sr_{0.5}(Co_{0.8}Fe_{0.2})_{0.9}Ti_{0.1}O_3$ (BSCFT), $NdBa_{0.5}Sr_{0.5}Co_{1.5}Fe_{0.5}O_{5+\delta}$ (NBSCF), $BaCo_{0.4}Fe_{0.4}Zr_{0.1}Y_{0.1}O_3$ (BCFZY), $BaZr_{0.85}Y_{0.15}O_3$ (BZY15), $BaCe_{0.9}Yb_{0.1}O_{3-\delta}$ (BCYb), $Sm_{0.5}Sr_{0.5}CoO_{3-\delta}$ (SSC), $Ce_{0.8}Sm_{0.2}O_{2-\delta}$ (SDC), $PrBaCo_2O_{5+\delta}$ (PBC), $BaZr_{0.7}In_{0.3}O_{3-\delta}$ (BZI), $BaZr_{0.1}Ce_{0.7}Y_{0.2}O_{3-\delta}$ (BZCY), $BaZr_{0.8}Y_{0.16}Zn_{0.04}O_{3-\delta}$ (BZYZn), $BaZr_{0.7}Pr_{0.1}Y_{0.2}O_{3-\delta}$ (BZPY), $BaZr_{0.5}Pr_{0.3}Y_{0.2}O_{3-\delta}$ (BZPY30), $BaZr_{0.4}Ce_{0.4}Y_{0.1}Yb_{0.1}O_3$ (BZCYYb4411), $PrBa_{0.5}Sr_{0.5}Co_{1.5}Fe_{0.5}O_{5+\delta}$ (PBSCF).

The aforementioned results clearly demonstrate that the BZCY6 cells exhibit superior fuel cell performances compared to BZCY4 cells in spite of the higher Zr contents and smaller grain sizes. **Figure 2-7c** displays the proton conductivity (σ) of the electrolyte films determined from R_b and film thickness; BZCY6 has higher conductivity than BZCY4 even though the grain boundary volumes of the former are apparently larger than those of the latter. To verify this point, I examine the proton conductivities of BZCY4 and BZCY6 bulk ceramics prepared by an SSRS process that is similar to the one used for the fabrication of anode-supported cells. The BZCY4 and BZCY6 ceramics thus prepared have highly dense matrices (relative density > 97%), with grain sizes equal to 10 and 5 μm diameter, respectively (**Figure 2-8a** and **2-8b**); these results are in agreement with the grain sizes observed for the thin film fuel cell (**Figure 2-3**). The impedance spectra of both ceramics show apparent bulk and interfacial contributions in high (10^6–10^5 Hz) and middle (10^5–10^2 Hz) frequency

ranges, respectively, at relatively low temperatures together with electrode contribution in low frequency region (< 10^2 Hz), as shown in **Figure 2-8c**. The bulk resistance of BZCY6 is lower than that of BZCY4 and thus, the total resistance of BZCY6 is 20% larger than that of BZCY4 at 200 °C; after increasing the temperature to 550 °C, both show only an *x*-intercept in the frequency range of 10^6–10^4 Hz due to sufficiently reduced resistances.[27] The *x*-intercept of BZCY6 is clearly smaller than that of BZCY4 at 550 °C.

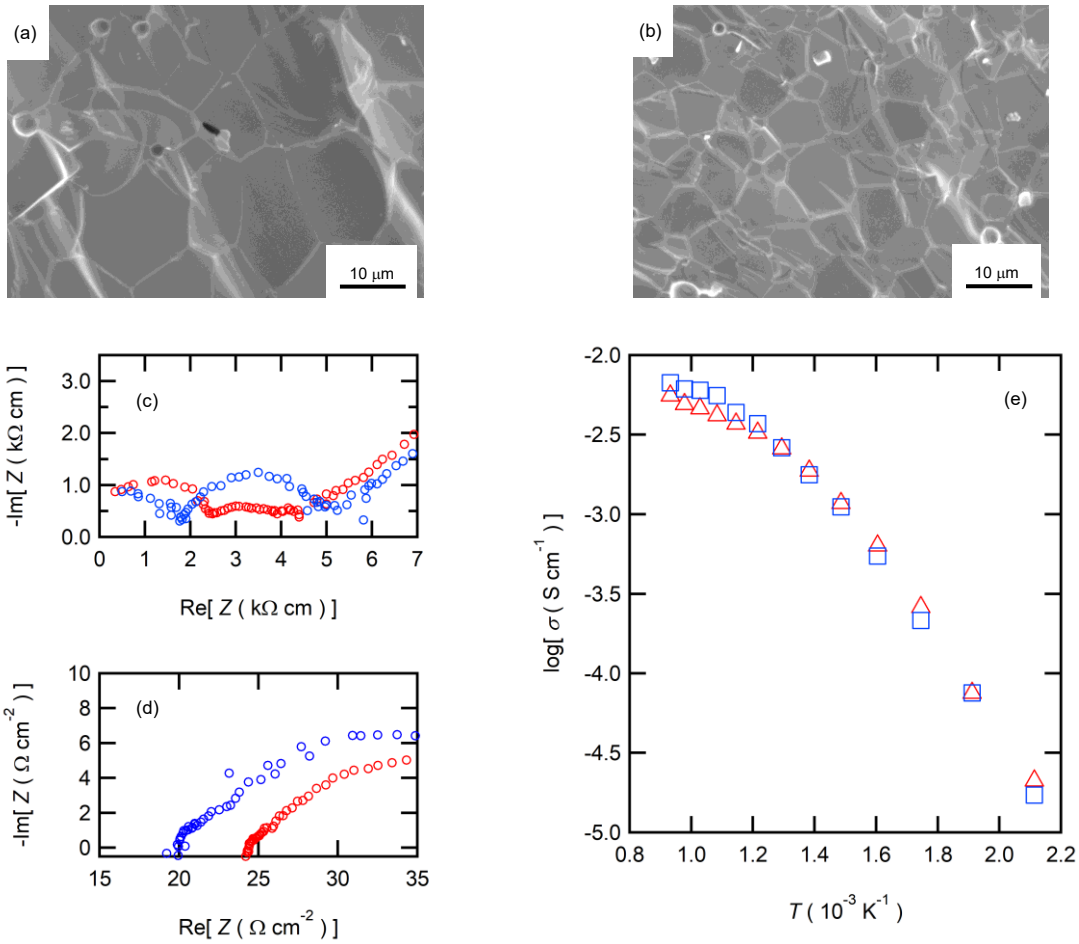

Figure 2-8. Cross-sectional SEM micrographs of thermally-etched (a) BZCY4 and (b) BZCY6 sintered discs. Impedance responses of the sintered discs measured in wet 10%-H_2/Ar at (c) 200 °C and (d) 600 °C (◯: BZCY4 and ◯: BZCY6); (e) Arrhenius plots of total conductivity of the sintered discs (△: BZCY4 and □: BZCY6).

Figure 2-8e displays the Arrhenius plots of the total conductivity of the BZCY4 and BZCY6 bulk ceramics determined by the sum of the bulk resistances and grain-boundary resistances. In both, the slopes of the plots change at around 400 °C, indicating that dominant conduction mechanism has

changed at this temperature. For many $BaZr_xCe_{0.8-x}Y_{0.2}O_{3-\delta}$ systems, it has been reported that the grain boundary resistances are dominant in the low-temperature region, whereas these are smaller than the bulk resistances in the high-temperature region because the activation energies of grain boundary conduction are larger than those of the bulk[28] Accordingly, the relatively high total conductivity of BZCY6 can be due to the bulk conductivity being higher than that of BZCY4 (**Figure 2-8e**). In fact, this feature is in agreement with the previously reported result.[27] These results prove that the superior fuel cell performances of BZCY6 can be due to relatively high proton conductivity in the intermediate temperature, 500–700 °C.

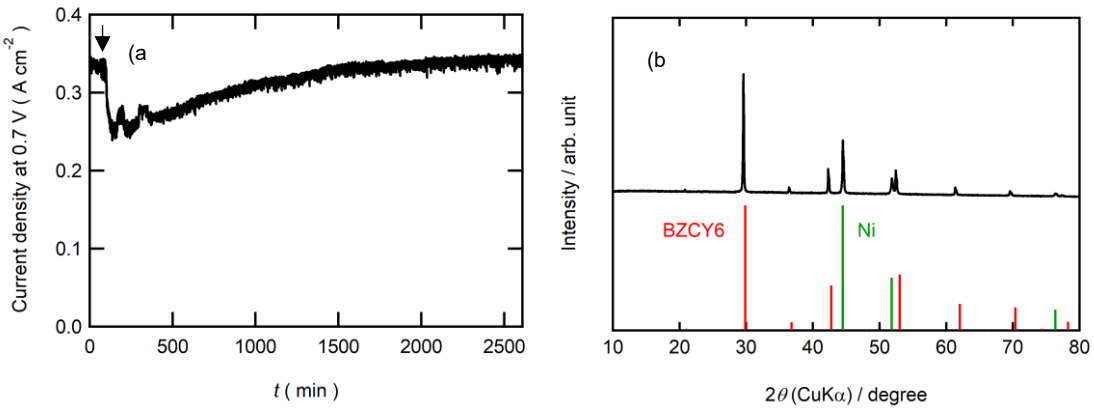

Figure 2-9. Durability test of BZCY6 cell. (a) Current decays of BZCY6 cells in a potentiostatic run at 0.7 V with fed by 1% CO_2-containing hydrogen fuels. (b) XRD pattern of BZCY6 cell after potentiostatic operation under CO_2-containg fuel conditions.

Finally, I examined the durability of BZCY6 under CO_2-containing fuel cell conditions. **Figure 2-9a** shows current decays of BZCY6 cells in potentiostatic operation at 0.7 V with 1% CO_2-containing hydrogen fuels. The cell keeps outputting a constant current of about 330 mA cm^{-2} for 2 days with CO_2-containing fuels although the current slightly decreases just after the introduction of CO_2. XRD measurements of the BZCY6 cell after durability tests confirm that decomposition products such as $BaCO_3$, ZrO_2 and CeO_2 are not formed even after fuel cell operations for several hours under a CO_2 atmosphere (**Figure 2-9b**), which reveals that BZCY6 is thermodynamically stable under CO_2-containing fuel conditions. The current results unambiguously demonstrate that BZCY6 is a promising electrolyte for PCFCs operating at around 600 °C with excellent low-temperature sinterability and CO_2 tolerance.

2.4. Conclusion

Herein, high performance anode-supported cells with Zr-rich $BaZr_xCe_{0.8-x}Y_{0.2}O_3$ (x = 0.4, 0.6, 0.7 and 0.8) were successfully fabricated by solid-state reactive sintering (SSRS) with $Zn(NO_3)_2$ additives by a single sintering step at 1400 °C. For x = 0.4 and 0.6, $BaZr_xCe_{0.8-x}Y_{0.2}O_3$ ceramics exhibited excellent sinterability and thus densely packed films comprising μm-sized grains were obtained by sintering at a relatively low temperature with the aid of Zn additives. According to the large-grained microstructures, the ohmic resistances of these electrolyte films were smaller than those reported for the analogous thin film and thus the cells with x = 0.4 and 0.6 exhibited highly efficient power generation, yielding peak power densities of 279 and 336 mW cm^{-2} at 600 °C, respectively, which were comparable to or several times higher than those of the analogous thin film fuel cells prepared from sol–gel-derived $BaZr_xCe_{0.8-x}Y_{0.2}O_3$ powders.

$BaZr_{0.6}Ce_{0.2}Y_{0.2}O_3$ was found to have higher proton conductivity than $BaZr_{0.4}Ce_{0.4}Y_{0.2}O_3$ at temperatures above 500°C despite the relatively high Zr contents and thus it showed excellent durability under CO_2-containing atmosphere. The preceding results encourage the development of high-performance PCFCs with thermally stable, Zr-enriched $BaZr_{0.6}Ce_{0.2}Y_{0.2}O_3$ electrolytes.

2.5. References

1. Y. Guo, Y. Lin, R. Ran and Z. Shao, "Zirconium doping effect on the performance of proton-conducting $BaZr_yCe_{0.8-y}Y_{0.2}O_{3-\delta}$ ($0.0 \leq y \leq 0.8$) for fuel cell applications" *J. Power Sources* **2009**, 193, 400.

2. C. Duan, J. Tong, M. Shang, S. Nikodemski, M. Sanders, S. Ricote, A. Almansoori and R. O'Hayre, "Readily processed protonic ceramic fuel cells with high performance at low temperatures" *Science* **2015**, 349, 1321.

3. S. Nikodemski, J. Tong and R. O'Hayre, "Solid-state reactive sintering mechanism for proton conducting ceramics" *Solid State Ionics* **2013**, 253, 201.

4. J. Tong, D. Clark, M. Hoban and R. O'Hayre, "Cost-effective solid-state reactive sintering method for high conductivity proton conducting yttrium-doped barium zirconium ceramics" *Solid State Ionics* **2010**, 181, 496.

5. J. Tong, D. Clark, L. Bernau, A. Subramaniyan and R. O'Hayre, "Proton-conducting yttrium-doped barium cerate ceramics synthesized by a cost-effective solid-state reactive sintering method" *Solid State Ionics* **2010**, 181, 1486.

6. R. D. Shannon, "Revised effective ionic radii and systematic studies of interatomic distances in halides and chalcogenides" *Acta Cryst*. **1976**, 32, 751.

7. L. Bi, E. Fabbri, Z. Sun and E. Traversa, "Sinteractive anodic powders improve densification and electrochemical properties of $BaZr_{0.8}Y_{0.2}O_{3-\delta}$ electrolyte films for anode-supported solid oxide fuel cells" *Energy Environ*. *Sci*. **2011**, 4, 1352.

8. J. Tong, D. Clark, L. Bernau, M. Sanders and R. O'Hayre, "Solid-state reactive sintering mechanism for large-grained yttrium-doped barium zirconate proton conducting ceramics" *J. Mater*. *Chem*. **2010**, 20, 6333.

9. W. G. Coors, "Protonic ceramics of the solid solution $BaCe_xZr_{0.8-x}Y_{0.2}O_{3-\delta}$ prepared by NiO-reactive sintering. Part I: fabrication and microstructure'', CoorsTek report (available from the author), March 18th, 2010.

10. A. Jun, J. Kim, J. Shin and G. Kim, "Perovskite as a Cathode Material: A review of its Role in Solid-Oxide Fuel Cell Technology" *ChemElectroChem* **2016**, 3, 511.

11. E. Fabbri, A. D'Epifanio, E. D. Bartolomeo, S. Licoccia and E. Traversa, "Tailoring the chemical stability of $Ba(Ce_{0.8-x}Zr_x)Y_{0.2}O_{3-\delta}$ protonic conductors for Intermediate Temperature Solid Oxide Fuel Cells (IT-SOFCs)" *Solid State Ionics* **2008**, 179, 558.

12. S. H. Nien, C. S. Hu, C. L. Chang and B. H. Hwang, "Preparation of $BaZr_{0.1}Ce_{0.7}Y_{0.2}O_{3-\delta}$ Based Solid Oxide Fuel Cells with Anode Functional Layers by Tape Casting" *Fuel Cells* **2011**, 11, 178.

13. Y. Liu, Y. Guo, R. Ran and Z. Shao, "A novel approach for substantially improving the sinterability of $BaZr_{0.4}Ce_{0.4}Y_{0.2}O_{3-\delta}$ electrolyte for fuel cells by impregnating the green membrane with zinc nitrate as a sintering aid" *J. Membr. Sci.* **2013**, 437, 189.
14. Y. Guo, R. Ran and Z. Shao, "A novel way to improve performance of proton-conducting solid-oxide fuel cells through enhanced chemical interaction of anode components" *Int. J. Hydrogen Energy* **2011**, 36, 1683.
15. L. Bi, E. Fabbri, Z. Sun and E. Traversa, "Sinteractivity, proton conductivity and chemical stability of $BaZr_{0.7}In_{0.3}O_{3-\delta}$ for solid oxide fuel cells (SOFCs)" *Solid State Ionics* **2011**, 196, 59.
16. D. Pergolesi, E. Fabbri and E. Traversa, "Chemically stable anode-supported solid oxide fuel cells based on Y-doped barium zirconate thin films having improved performance" *Electrochem. Commun.* **2010**, 12, 977.
17. Y. Guo, R. Ran and Z. Shao, "Optimizing the modification method of zinc-enhanced sintering of $BaZr_{0.4}Ce_{0.4}Y_{0.2}O_{3-\delta}$-based electrolytes for application in an anode-supported protonic solid oxide fuel cell" *Int. J. Hydrogen Energy* **2010**, 35, 5611.
18. N. Nasani, D. Ramasamy, S. Mikhalev, A. V. Kovalevsky and D. P. Fagg, "Fabrication and electrochemical performance of a stable, anode supported thin $BaCe_{0.4}Zr_{0.4}Y_{0.2}O_{3-\delta}$ electrolyte Protonic Ceramic Fuel Cell" *J. Power Sources* **2015**, 278, 582.
19. L. Bi, E. Fabbri and E. Traversa, "Effect of anode functional layer on the performance of proton-conducting solid oxide fuel cells (SOFCs)" *Electrochem. Commun.* **2012**, 16, 37.
20. Y. Liu, R. Ran, M. O. Tade and Z. Shao, "Structure, sinterability, chemical stability and conductivity of proton-conducting $BaZr_{0.6}M_{0.2}Y_{0.2}O_{3-\delta}$ electrolyte membranes: The effect of the M dopant" *J. Membr. Sci.* **2014**, 467, 100.
21. J. Xiao, W. Sun, Z. Zhu, Z. Tao and W. Liu, "Fabrication and characterization of anode-supported dense $BaZr_{0.8}Y_{0.2}O_{3-\delta}$ electrolyte membranes by a dip-coating process" *Mater. Lett.* **2012**, 73, 198.
22. I. Luisetto, S. Licoccia, A. D'Epifanio, A. Sanson, E. Mercadelli and E. D. Bartolomeo, "Electrochemical performance of spin coated dense $BaZr_{0.80}Y_{0.16}Zn_{0.04}O_{3-\delta}$ membranes" *J. Power Sources* **2012**, 220, 280.
23. E. Fabbri, L. Bi, H. Tanaka, D. Pergolesi and E. Traversa, "Chemically Stable Pr and Y Co-Doped Barium Zirconate Electrolytes with High Proton Conductivity for Intermediate-Temperature Solid Oxide Fuel Cells" *Adv. Funct. Mater.* **2011**, 21, 158.
24. E. Fabbri, L. Bi, J. L. M. Rupp, D. Pergolesi and E. Traversa, "Electrode tailoring improves the intermediate temperature performance of solid oxide fuel cells based on a Y and Pr co-doped barium zirconate proton conducting electrolyte" *RSC Adv.* **2011**, 1, 1183.
25. K. Bae, D. Y. Jang, H. J. Choi, D. Kim, J. Hong, B. K. Kim, J. H. Lee, J. W. Son and J. H. Shim,

"Demonstrating the potential of yttrium-doped barium zirconate electrolyte for high-performance fuel cells" *Nat. Commun.* **2017**, 8, 14553.

26. S. Choi, C. J. Kucharczyk, Y. Liang, X. Zhang, I. Takeuchi, H. I. Ji and S. M. Haile, "Exceptional power density and stability at intermediate temperatures in protonic ceramic fuel cells" *Nat. Energy* **2018**, 3, 202.

27. P. Sawant, S. Varma, B. N. Wani and S. R. Bharadwaj, "Synthesis, stability and conductivity of $BaCe_{0.8-x}Zr_xY_{0.2}O_{3-\delta}$ as electrolyte for proton conducting SOFC" *Int. J. Hydrogen Energy* **2012**, 37, 3848.

28. S. Ricote, N. Bonanos, A. Manerbino and W. G. Coors, "Conductivity study of dense $BaCe_xZr_{(0.9-x)}Y_{0.1}O_{(3-\delta)}$ prepared by solid state reactive sintering at 1500 °C" *Int. J. Hydrogen Energy* **2012**, 37, 7954.

Chapter 3

Mechanism of power generation in hydrogen-permeable metal-support-type fuel cells (HMFCs): Proton pumping

3.1. Objective of chapter 3

Protonic ceramic fuel cells normally have configuration of porous-anode-support-type fuel cells (PAFCs), as described in the chapter 2; they comprise a porous cathode of an O^{2-}/e^{-} mixed conductor, a dense $BaZr_xCe_{1-x-y}M_yO_{3-\delta}$ (BZCM; M = Y, Yb, etc.) electrolyte membrane, and a porous anode support of a Ni-electrolyte cermet (**Figure 3-1a**). Although PAFCs exhibiting peak power densities greater than 1 W cm^{-2} at 600 °C[1–3] have been reported recently, their applicability at below 500 °C remains limited. As presented in the chapter 1, this is attributed to greater ohmic loss than expected and enlarged cathodic polarization resistance due to the confined effective reaction area within gas–electrolyte–cathode triple-phase boundaries (TPBs) of conventional O^{2-}/e^{-} conducting cathodes.

Meanwhile, a hydrogen-permeable metal-support-type fuel cell (HMFC), which is based on a solid–solid heterostructure consisting of a BZCM electrolyte thin film and a dense, hydrogen-permeable metal anode support with a top layer of an O^{2-}/e^{-} mixed-conduction porous cathode (**Figure 3-1b**), gained an extraordinary peak power density of 0.9 W cm^{-2} at 400 °C (**Figure 3-1c**) although the electrolyte and cathode materials used in HMFC are similar to those employed in conventional PAFCs.[4] Therefore, the power generation mechanism of HMFC must be different with

conventional PAFCs and thus the underlying phenomenon should be investigated.

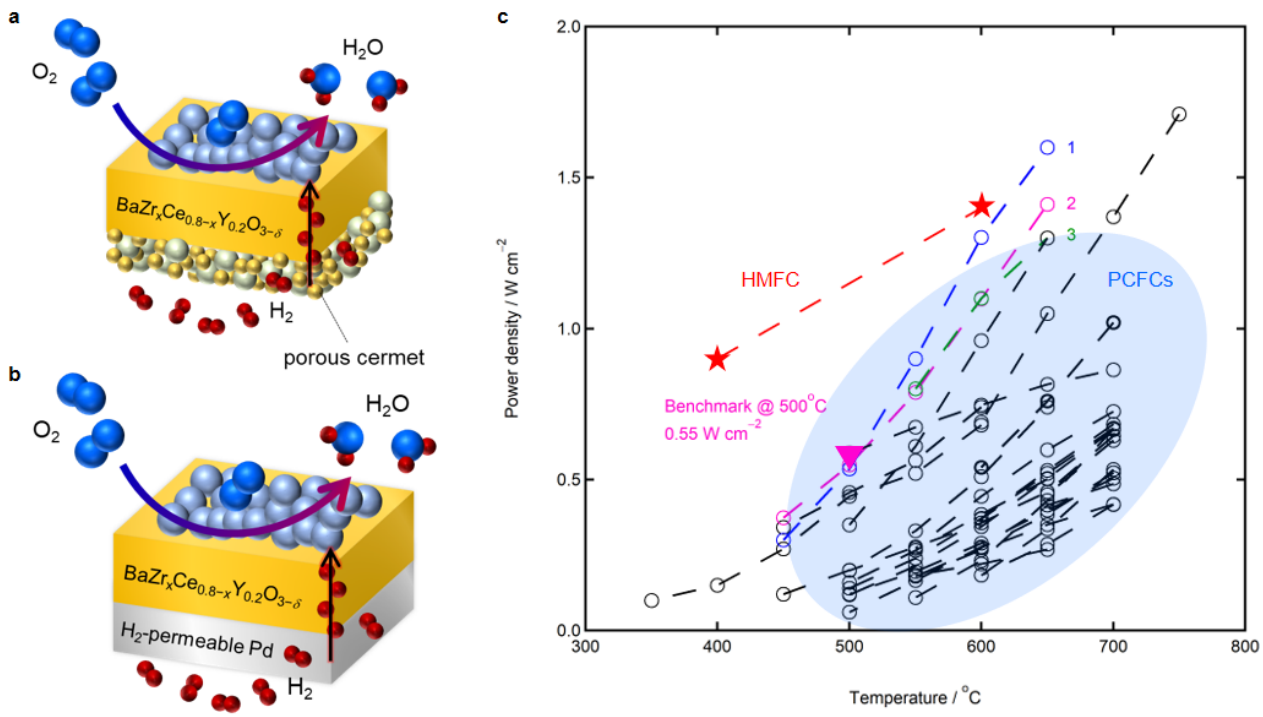

Figure 3-1. Cell configurations of HMFC and PAFC and the performance distribution. Schematic cell configuration of **a,** PAFC and **b,** HMFC. **c,** Performance distribution of protonic ceramic fuel cells (PCFCs). Numbers show literatures (1. An et al.[1], 2. Choi et al.[2], 3. Bae et al.[3]). Star plots show HMFC performances reported from Ito et al.[4] Pink inverted triangle plot corresponds to benchmark at 500°C.

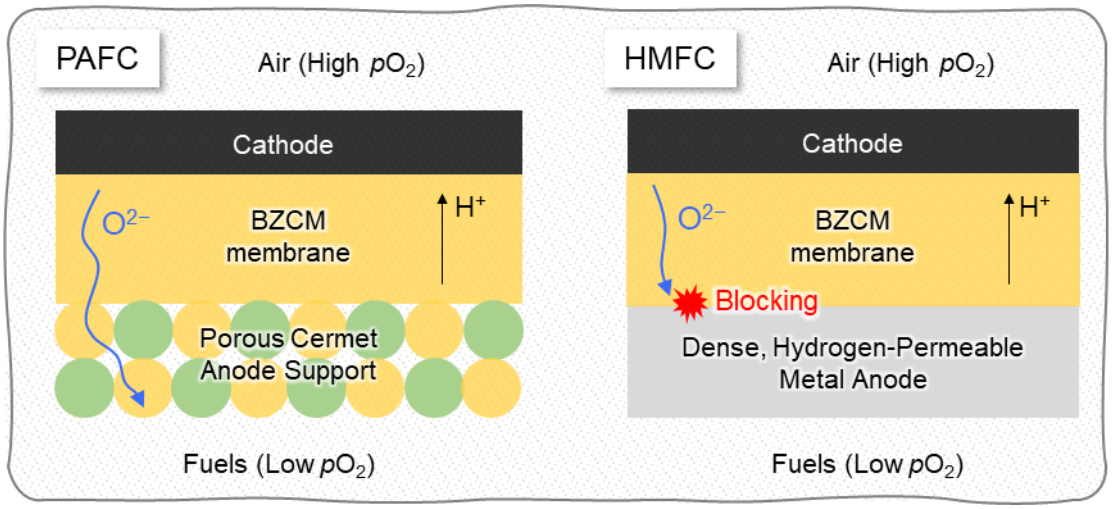

Figure 3-2. Motivation of this chapter: Blocking of secondary oxide-ion conduction in HMFCs.

This chapter aims to understand the power generation mechanism of HMFC. I have noted that the metal/oxide heterointerfaces in HMFCs block secondary oxide-ion conduction, which necessarily happens toward anode within BZCM electrolyte membranes due to the difference in chemical potential of oxygen between anode and cathode under fuel cell atmosphere, as shown in **Figure 3-2**. In this chapter, to understand the effects of oxide-ion blocking on the power generation mechanism, the electrochemical behavior was compared between PAFCs and HMFCs by means of numerical and electrochemical methods: Mass transfers were simulated within electrolyte membranes between PAFCs and HMFCs based on the Nernst–Planck–Poisson model and their electrochemical behavior was experimentally confirmed. As a result, it is demonstrated that HMFCs show higher power outputs than those of conventional PAFCs despite using the same electrolyte and cathode materials. This is due to 'proton pumping', which is triggered by the blocking of oxide-ion conduction at the metal/electrolyte heterointerfaces. It allows HMFCs to pump excess protons into BZCM membranes

through chemical potential of oxygen so as to compensate for negative charge of the oxide ions that accumulate due to the prevention of their conduction, so that the BZCM membranes used in HMFCs are heavily hydrated and eject the excess protons via the formation of water at the cathode side, thereby decreasing the electrolyte and cathodic polarization resistances.

3.2. Numerical methods

3.2.1. Numerical simulations of defect concentration profiles

I simulated the local defect concentration profiles and ionic conductivities of a $BaZr_{0.8}Y_{0.2}O_{3-\delta}$ (BZY) membrane in the HMFC and PAFC configurations to obtain insight regarding the effects of Pd/electrolyte heterointerfaces. I used the Nernst–Planck–Poisson model,[5–8] which is in terms of defect mass conservation, Nernst–Planck flux and Gauss law, to predict the defect and electrostatic potential profiles of the BZY membrane through numerical simulations performed using experimentally determined thermodynamic parameters.[7] The simulation methods used were similar to those employed in previous studies.[5–8] During the simulations, I assumed a one-dimensional BZY electrolyte that contains the following three charged defect carriers: Oxygen vacancies ($V_O^{\bullet\bullet}$), protons ($OH_O^{\bullet}$) and oxygen holes ($O_O^{\bullet}$). The flux of each defect carrier was simulated only along the thickness direction. The coordinates within the electrolyte membrane were defined only by the thickness (L), which was normalized so that the anode and cathode surfaces could be set as 0 and 1, respectively. Further, all the defects are represented using the Krögger–Vink notation.

The mathematical models used are shown in **Figure 3-3**. For the PAFC, the boundary conditions, namely the defect concentrations at the membrane surfaces, were determined by assuming a state of equilibrium between the BZY membrane and the gas phase. The H_2 and H_2O partial pressures (p_{H2} and p_{H2O}, respectively) on the anode side are 0.97 p_0 and 0.03 p_0, respectively. The values for p_{H2O} and O_2 partial pressure (p_{O2}) on the cathode side are 0.2 p_0 and 0.03 p_0, respectively. Here p_0 is the

standard pressure, i.e., 101.3 kPa. In the case of the HMFC, however, the boundary conditions at the anodic surface were undefined because the surface was sealed by the dense metal anode and hence was not in equilibrium with the water vapor present in the anode gas (**Figure 3-3b**). The nominal p_{H2} at the metal/electrolyte interface can be fixed at 1.0 p_0 because Pd anode is equilibrated with pure H_2 gas whereas the p_{H2O} is undefined. Meanwhile, the flux of $V_O^{\bullet\bullet}$ defects was set as 0 for the HMFC membrane because the conduction of the oxide ions, that is, $V_O^{\bullet\bullet}$, was blocked. However, the $OH_O^{\bullet}$ and $O_O^{\bullet}$ defects could diffuse across the interface between the BZY membrane and the solid metal anode. This allowed the boundary conditions at the anodic surface to be determined. Electrostatic potentials were implicitly imposed on the membranes in terms of the current density, which was taken to be the sum of all the fluxes of the charged defects within the membrane. For both cells, the cathode is set as reference electrode. The computation performed are described in the following sections.

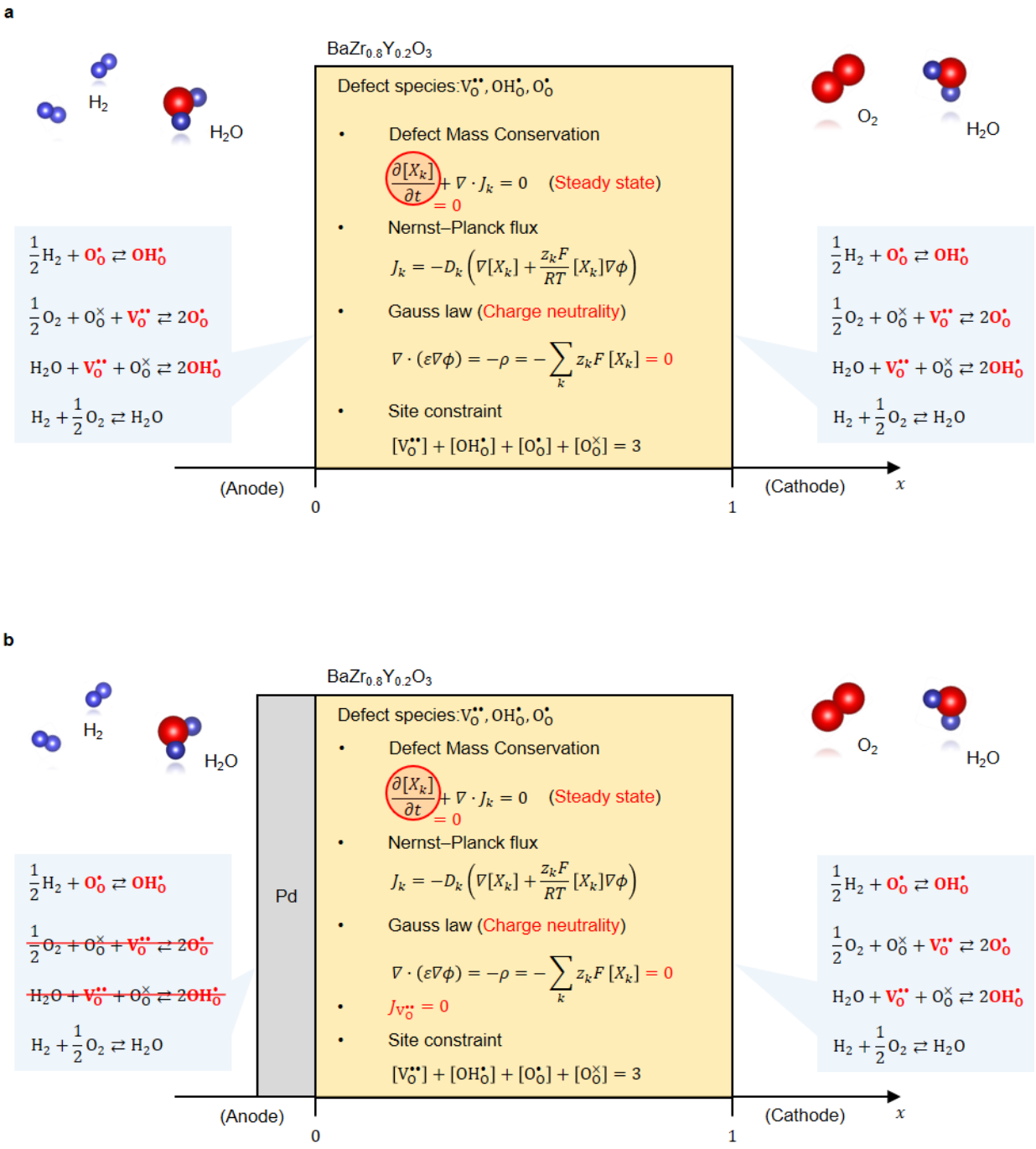

Figure 3-3. Mathematical models for numerical simulations of mobile charge-carrying defect profiles in a fuel cell with $BaZr_{0.8}Y_{0.2}O_{3-\delta}$ (BZY) membranes. **a,** Model for a porous-anode-support-type fuel cell (PAFC). **b,** Model for a hydrogen-permeable metal-support-type fuel cell (HMFC).

3.2.2 Defect thermodynamics

Three mobile charge-carrying defects (protons $\mathrm{OH_O^{\bullet}}$, oxygen vacancies $\mathrm{V_O^{\bullet\bullet}}$, oxygen holes $\mathrm{O_O^{\bullet}}$) are involved in BZCM electrolytes through the defect reactions at gas–oxide interface. The defect formation reaction can be written by the following equations.

$$\frac{1}{2}\mathrm{H_2} + \mathrm{O_O^{\bullet}} \rightleftharpoons \mathrm{OH_O^{\bullet}}. \quad (1)$$

$$\frac{1}{2}\mathrm{O_2} + \mathrm{V_O^{\bullet\bullet}} + \mathrm{O_O^{\times}} \rightleftharpoons 2\mathrm{O_O^{\bullet}}. \quad (2)$$

$$\mathrm{H_2O} + \mathrm{V_O^{\bullet\bullet}} + \mathrm{O_O^{\times}} \rightleftharpoons 2\mathrm{OH_O^{\bullet}}. \quad (3)$$

The equilibrium constant of Eqs. (1), (2), and (3) can be defined as follows.

$$K_{\mathrm{H_2}} = \frac{[\mathrm{OH_O^{\bullet}}]}{p_{\mathrm{H_2}}^{1/2}[\mathrm{O_O^{\bullet}}]}. \quad (4)$$

$$K_{\mathrm{O_2}} = \frac{[\mathrm{O_O^{\bullet}}]^2}{p_{\mathrm{O_2}}^{1/2}[\mathrm{V_O^{\bullet\bullet}}][\mathrm{O_O^{\times}}]}. \quad (5)$$

$$K_{\mathrm{H_2O}} = \frac{[\mathrm{OH_O^{\bullet}}]^2}{p_{\mathrm{H_2O}}[\mathrm{V_O^{\bullet\bullet}}][\mathrm{O_O^{\times}}]}. \quad (6)$$

$[X_k]$ is defined as the formula-unit concentration of defect species, which is related to a molar concentration $[X_k]_{\mathrm{m}}$ with a molar volume, V_{m}, as $[X_k] = [X_k]_{\mathrm{m}}V_{\mathrm{m}}$. The three equilibrium constants, $K_{\mathrm{H_2}}$, $K_{\mathrm{O_2}}$ and $K_{\mathrm{H_2O}}$ are not independent, but instead are coupled through the water dissociation reactions.

$$\mathrm{H_2O} \rightleftharpoons \mathrm{H_2} + \frac{1}{2}\mathrm{O_2}. \quad (7)$$

The equilibrium constants of Eq. (7) (K_w) can be correlated with $K_{\mathrm{H_2}}$, $K_{\mathrm{O_2}}$ and $K_{\mathrm{H_2O}}$ as follows.

$$K_{\mathrm{H_2}}{}^2 K_{\mathrm{O_2}} = K_{\mathrm{H_2O}} K_w \quad (8)$$

Normally, the equilibrium constants, K, are related to the Gibbs free energy changes ($\Delta G° = \Delta H° - T\Delta S°$) of the reactions as follows.

$$K = \exp\left(-\frac{\Delta G^{\circ}}{RT}\right) = \exp\left(\frac{\Delta S^{\circ}}{R}\right)\exp\left(-\frac{\Delta H^{\circ}}{RT}\right). \quad (9)$$

Unfortunately, the complete sets of thermodynamic parameters, i.e., $\Delta H°$ and $\Delta S°$ of the three defect formation reactions (Eqs. (1), (2) and (3)), are not available for BZCY. Alternatively, all the thermodynamic parameters of $BaZr_{0.8}Y_{0.2}O_{3-\delta}$ have been experimentally investigated elsewhere[9] altogether with diffusion coefficients and activation energy of each defect, such that the simulations here were carried out by using the thermodynamic and diffusional parameters of $BaZr_{0.8}Y_{0.2}O_{3-\delta}$,[9] as listed in **Table 3-1** and **Table 3-2**. The diffusion coefficients of each defect at an arbitrary temperature are calculated with the activation energy (E_k) of the defects as

$$D_k = D_k^{\circ}\exp\left(-E_k/RT\right). \quad (10)$$

Table 3-1. Thermodynamics of defect reactions for BZY[9]

Reaction	ΔH° (kJ mol^{-1})	ΔS° (J mol^{-1} K^{-1})
$\frac{1}{2}H_2 + O_O^{\bullet} \rightleftharpoons OH_O^{\bullet}$	−158.67	−50.74
$\frac{1}{2}O_2 + O_O^{\times} + V_O^{\bullet\bullet} \rightleftharpoons 2O_O^{\bullet}$	−24.08	−54.00
$H_2O + V_O^{\bullet\bullet} + O_O^{\times} \rightleftharpoons 2OH_O^{\bullet}$	−93.30	−100.00
$H_2 + \frac{1}{2}O_2 \rightleftharpoons H_2O$	−248.11	−55.48

Table 3-2. Diffusion coefficients of mobile defects for BZY[9]

Mobile defect	D_k° ($m^2\ s^{-1}$)	E_k (kJ mol^{-1})
$OH_O^{\bullet}$	5.37×10^{-7}	61.01
$V_O^{\bullet\bullet}$	1.98×10^{-7}	84.92
$O_O^{\bullet}$	2.79×10^{-5}	78.92

Site constraints and electroneutrality must be preserved inside the BZCY membranes. The total number of oxide ion sites in the perovskite is 3.

$$[V_O^{\bullet\bullet}] + [OH_O^{\bullet}] + [O_O^{\bullet}] + [O_O^{\times}] = 3. \quad (11)$$

Total charges of the positively charged defects should be equivalent to total charges of the acceptor dopants, i.e., $[Y'_{Zr}]$ defects.

$$2[V_O^{\bullet\bullet}] + [OH_O^{\bullet}] + [O_O^{\bullet}] - [Y'_{Zr}] = 0. \quad (12)$$

In BZY, $[Y'_{Zr}] = 0.2$. For the molar volume, $V_m = 4.57 \times 10^{-5}$ m^3 mol^{-1}.

With Eqs. (5), (6), and (12), the defect concentration of $[O_O^{\bullet}]$ can be given by the function of $[V_O^{\bullet\bullet}]$ as

$$[O_O^{\bullet}]_L = \frac{[Y'_{Zr}]-2[V_O^{\bullet\bullet}]}{1+\Theta}, \quad (13)$$

where

$$\Theta = \frac{[OH_O^{\bullet}]}{[O_O^{\bullet}]} = \left[\frac{K_{H_2O}}{K_{O_2}}\frac{p_{H_2O}}{p_{O_2}^{0.5}}\right]^{1/2}. \quad (14)$$

Consequently,

$$[\mathrm{OH}_{\mathrm{O}}^{\bullet}] = \Theta \cdot [\mathrm{O}_{\mathrm{O}}^{\bullet}]. \tag{15}$$

Using Eq. (5), $[\mathrm{O}_{\mathrm{O}}^{\times}]$ is given by

$$[\mathrm{O}_{\mathrm{O}}^{\times}] = \frac{[\mathrm{O}_{\mathrm{O}}^{\bullet}]^2}{K_{\mathrm{O}_2} p_{\mathrm{O}_2}^{1/2} [\mathrm{V}_{\mathrm{O}}^{\bullet\bullet}]}. \tag{16}$$

By explicitly substituting Eqs. (13), (15) and (16) for Eq. (11), lattice oxygen site constraint in perovskite, one non-linear self-consistent equation by one unknown, $[\mathrm{V}_{\mathrm{O}}^{\bullet\bullet}]$, is obtained as shown below.

$$[\mathrm{Y}_{\mathrm{Zr}}'] - [\mathrm{V}_{\mathrm{O}}^{\bullet\bullet}] + \frac{1}{K_{\mathrm{O}_2}\sqrt{p_{\mathrm{O}_2}}(1+\Theta)^2} \frac{\left([\mathrm{Y}_{\mathrm{Zr}}'] - [\mathrm{V}_{\mathrm{O}}^{\bullet\bullet}]\right)^2}{[\mathrm{V}_{\mathrm{O}}^{\bullet\bullet}]} - 3 = 0. \tag{17}$$

The Eq. (17) is numerically solved by means of Newton's method, a root-finding algorithm. The iterative calculation process is initiated by giving an appropriate initial value of $[\mathrm{V}_{\mathrm{O}}^{\bullet\bullet}]$. If a $[\mathrm{V}_{\mathrm{O}}^{\bullet\bullet}]$ to satisfy Eq. (17) is discovered, all other defect concentrations are determined from Eqs. (13), (15) and (16).

3.2.3. Nernst–Planck–Poisson model for one-dimensional BZCY membranes

The spatial and temporal profiles of defect concentrations and the electrostatic potential across the BZCY electrolyte membrane can be simulated using Nernst–Planck–Poisson model. The defect transport through the membrane is governed by defect mass conservation equation as

$$\frac{\partial [X_k]}{\partial t} + \nabla \cdot J_k = 0. \tag{18}$$

Here, $[X_k]$ shows a concentration of defect carrier k and J_k is the transport flux. Without any interaction among individual defects, J_k occurs according to concentration gradients (diffusion) and

electrostatic potential gradients (migration); thus, it can be represented using a Nernst–Planck formulation as

$$J_k = -D_k \left(\nabla [X_k] + \frac{z_k F}{RT} [X_k] \nabla \phi \right). \quad (19)$$

Under steady state,

$$\nabla \cdot J_k = 0. \quad (20)$$

In this study, chemical potential gradients and electrical fields are assumed to develop only along *x*-axis, i.e., the direction from cathode to anode; therefore, in-plane fluxes are negligible. In one-dimensional model under steady state, the governing equation is rewritten by coupled with Eq. (19) and (20), as

$$\frac{\partial}{\partial x} J_k = \frac{d^2 [X_k]}{dx^2} + \frac{z_k F}{RT} \frac{d[X_k]}{dx} \frac{d\phi}{dx} + \frac{z_k F}{RT} [X_k] \frac{d^2 \phi}{dx^2} = 0. \quad (21)$$

D_k and z_k are diffusion coefficients and charges of the k defect carrier, respectively, and F is a faraday constant. D_k is applied by the data for BZY[9] as listed in **Table 3-2**. The variable ϕ is the local electrostatic potential, which is related to the local charge density ρ as follows through the Gauss law:

$$\nabla \cdot (\varepsilon_r \varepsilon_0 \nabla \phi) = -\rho = -\sum_k z_k F [X_k]. \quad (22)$$

Local charge neutrality should be established according to Eq. (12), which requires the right-hand side of Eq. (22) to equal 0.

$$\frac{d^2 \Phi}{dx^2} = -\frac{dE}{dx} = -\frac{1}{\varepsilon_r \varepsilon_0} \sum_k z_k F [X_k] = 0. \quad (23)$$

Eq. (23) means that the electrical field is constant across electrolyte membranes. Hence, ϕ is

represented by

$$\phi = -\frac{\phi_a}{L}(x - L). \quad (24)$$

The variable ϕ_a is the potential at gas–electrolyte interface of the anode side, and L is a thickness of membrane. The variable x is a one-dimensional coordinate on the line between two surfaces across membranes, in which $x = 0$ and L at the anode and cathode sides, respectively. Introducing Eqs. (23) and (24) into Eq. (21), the fluxes can be represented by

$$\frac{d^2[X_k]}{dx^2} - \frac{z_k F \phi_a}{RTL}\frac{d[X_k]}{dx} = 0. \quad (25)$$

3.2.4. Mathematical model for PAFC

At the membrane surfaces, the defect reactions of Eqs. (1), (2), (3) and (4) are in equilibrium with the anode or cathode gases. Therefore, the defect concentrations at the surfaces in anode and cathode sides are calculated from Eqs. (13)–(16), all together with site constraints (Eq. (11)) and charge neutrality (Eq. (12)), by using a thermodynamic data as listed in **Table 3-1**. These values are employed to the defect concentration boundary conditions for numerical simulations. Boundary conditions are also needed for the internal electrostatic potentials. At the cathode surface, a reference potential, ϕ_c, is set to be 0. The other boundary, i.e., ϕ_a is implicitly imposed in terms of the current density which is yielded by the summation of all charged defect fluxes inside membranes, as

$$I = \sum_k z_k F J_k. \quad (26)$$

The I thus obtained is equivalent to the output current. With these boundary conditions, the defect concentrations, such as protons $[OH_O^{\bullet}]$, oxygen vacancies $[V_O^{\bullet\bullet}]$, and oxygen holes $[O_O^{\bullet}]$ at each x

can be determined by solving the governing equation of Eq. (25).

3.2.5. Mathematical model for HMFC

Unlike PAFC, the boundary conditions at the anode side cannot be directly calculated in HMFC. Anode surface of the BZCY membrane is covered with a dense hydrogen-permeable metal anode, so that any gas phase other than hydrogen is not able to be equilibrated with electrolyte membrane; hence, the defect reactions of (2) and (3) are not established. With regard to HMFC, however, as the metal anode acts as a blocking electrode only for oxide-ion conduction, the flux of $V_O^{\bullet\bullet}$ defects must be 0.

$$J_{V_O^{\bullet\bullet}} = -D_{V_O^{\bullet\bullet}} \left(\frac{\partial}{\partial x} [V_O^{\bullet\bullet}] + \frac{2F}{RT} [V_O^{\bullet\bullet}] \frac{\partial}{\partial x} \phi \right) = 0. \quad (27)$$

By solving Eq. (27) with combining Eq. (24), $[V_O^{\bullet\bullet}]$ profile in the electrolyte membrane is explicitly determined as

$$[V_O^{\bullet\bullet}](x) = [V_O^{\bullet\bullet}](L) \exp\left(\frac{2F\phi_a}{RTL} (x - L) \right). \quad (28)$$

The cathodic surface of the membrane is equilibrated with O_2 and H_2O gases in HMFC, so that the $[V_O^{\bullet\bullet}](L)$, oxygen vacancy at cathode, can be calculated by Eq. (17), allowing calculation of $[V_O^{\bullet\bullet}](0)$, oxygen vacancy at anode using Eq. (28).

Based on the $[V_O^{\bullet\bullet}](0)$, anodic boundary conditions, i.e., concentrations of the other defects, can be equipped. Once $[V_O^{\bullet\bullet}](0)$ is calculated, Eq. (12) becomes equation with the two variables, $[O_O^{\bullet}]$ and $[OH_O^{\bullet}]$. Moreover, since hydrogen is able to equilibrate with electrolyte membrane, the relation between $[O_O^{\bullet}]$ and $[OH_O^{\bullet}]$ is determined by the equilibrium constant, Eq. (4). Therefore, by solving

the simultaneous equation comprised of Eqs. (4) and (12), the anodic boundary condition, $[\mathrm{O}_{\mathrm{O}}^{\bullet}](0)$ and $[\mathrm{OH}_{\mathrm{O}}^{\bullet}](0)$ is determined as

$$[\mathrm{O}_{\mathrm{O}}^{\bullet}](0) = \frac{[\mathrm{Y}'_{\mathrm{Zr}}]-2[\mathrm{V}_{\mathrm{O}}^{\bullet\bullet}]}{1+K_{\mathrm{H_2}}\sqrt{p_{\mathrm{H_2}}}}. \quad (29)$$

and

$$[\mathrm{OH}_{\mathrm{O}}^{\bullet}](0) = \frac{K_{\mathrm{H_2}}\sqrt{p_{\mathrm{H_2}}}}{1+K_{\mathrm{H_2}}\sqrt{p_{\mathrm{H_2}}}}([\mathrm{Y}'_{\mathrm{Zr}}] - 2[\mathrm{V}_{\mathrm{O}}^{\bullet\bullet}]). \quad (30)$$

Numerical calculation of defect profiles can be implemented with the boundary conditions including Eqs. (28)–(30). As to electrostatic potential, boundary conditions are imposed in the same way with PAFC. With these boundary conditions, the defect concentrations, such as protons $[\mathrm{OH}_{\mathrm{O}}^{\bullet}]$, oxygen vacancies $[\mathrm{V}_{\mathrm{O}}^{\bullet\bullet}]$ and oxygen holes $[\mathrm{O}_{\mathrm{O}}^{\bullet}]$ at each x can be determined by solving the governing equation of Eq. (25).

3.2.6. Local defect conductivity and polarization curves

In general, electrical conductivity is represented as

$$\sigma = q\mu C \quad (31)$$

where q, μ and C are charge, mobility and concentration. Nernst–Einstein relation provides the relationship between diffusion coefficient D_k and mobility μ_k as

$$\frac{\mu_k}{D_k} = \frac{q}{k_B T} \quad (32)$$

where k_B is boltzmann constant. Based on the Nernst–Einstein relation, the local conductivity of k defect in molar unit is represented as

$$\sigma_k(x) = \frac{(z_k F)^2}{RT} D_k[X_k]. \quad (33)$$

Polarization property, *I–V* curve, and cell performances in HMFC and PAFC are also simulated. When assuming perfect charge transfer at both electrodes, activation overpotentials are neglected and thus cell voltage can be evaluated as

$$E_{\mathrm{cell}} = (\phi_{\mathrm{c}} - \phi_{\mathrm{a}}) + \frac{RT}{F}\left(\ln\frac{[\mathrm{O}_{\mathrm{O}}^{\bullet}](L)}{[\mathrm{O}_{\mathrm{O}}^{\bullet}](0)} - \ln\frac{[\mathrm{O}_{\mathrm{O}}^{\times}](L)}{[\mathrm{O}_{\mathrm{O}}^{\times}](0)}\right).^{6} \quad (34)$$

3.2.7. Profiles of gaseous effective partial pressure

To obtain thermodynamic insights into the power generation of HMFC in terms of chemical potential, the profiles of gaseous effective partial pressure were calculated. Based on the simulated concentration profiles of all defects, assuming that each position of the membrane is quasi-equilibrated with gaseous phase, the effective partial pressure profiles of H_2, O_2 and H_2O were calculated with Eqs. (4), (5) and (6).

All the above simulations were implemented with C programming language.

3.3. Experimental

3.3.1. Fabrication and characterization of HMFC

HMFCs were fabricated by the same method as reported in the previous report.[10] Deposition of $BaZr_{0.1}Ce_{0.7}Y_{0.2}O_{3-\delta}$ (BZCY) electrolyte thin films were attempted on a Pd foil (0.05 × 12 × 12 mm, Tanaka Co.) by radio frequency cosputtering with $BaCe_{0.8}Y_{0.2}O_{3-\delta}$ and ZrO_2 targets. A commercial $La_{0.6}Sr_{0.4}Co_{0.2}Fe_{0.8}O_3$ (Fuelcellmaterials) button electrode (7 mmϕ) was screen-printed onto the surface of the BZCY film as a porous cathode. The optimal conditions for RF sputtering were listed in the previous report.[10] The phase purity of the deposited BZCY films was checked by X-ray diffraction (XRD) with Rigaku Ultima IV (CuKα radiation). The morphology was examined using a field-emission scanning electron microscope (FESEM; SIGMA500, ZEISS). The chemical composition was examined by field emission electron probe microanalyzer (FE-EPMA) with JXA-8530F instrument. Microstructures were examined via transmission electron microscopy (TEM; JEM-ARM200F). The specimens for TEM observation were prepared by a focused ion beam microfabrication (FIB; Hitachi FB-2100).

3.3.2. Fabrication and characterization of PAFC

PAFCs were fabricated by solid-state reactive sintering of the green pellets with $Zn(NO_3)_2$ sintering aids as described in the chapter 2. Shortly, precursor powders of $BaZr_{0.1}Ce_{0.7}Y_{0.2}O_{3-\delta}$ (BZCY) were prepared by mixing stoichiometric amounts of starting materials: $BaCO_3$ (High purity chemicals, 99.95%), CeO_2 (High purity chemicals, 99.99%), ZrO_2 (High purity chemicals, 98%), and

Y_2O_3 (High purity chemicals, 99.99%) with addition of 3.56 wt.% of $Zn(NO_3)_2$ $6H_2O$ (Wako chemicals, 99.9%) as a sintering aid. For Ni/BZCY anode supports, BZCY precursor and NiO powder (High purity chemicals, 99%) were blended at weight ratio of 40:60 in ethanol, and ball milled for 48 h. The obtained mixed powders were pressed into green pellets (12 mmϕ, 1.2 mm *d*) under a hydrostatic pressure of 100 MPa. The precursor layers of electrolyte films were spin-coated on the surfaces of the green pellets at 3000 rpm for 40 s with a sol prepared by dispersing a BZCY precursor powders in a solution including dispersant (20 wt.% polyethyleneimine (Mw 28000) dissolved in α-terpineol) and binder (5 wt.% surfactant dissolved in α-terpineol) at a weight ratio of 10:3:1. The pellets were co-fired at 1400 °C for 8 h in air, which resulted in a compact ceramic disc with ca. 10 mm $\phi \times$ 1 mm *d*. Finally, $La_{0.6}Sr_{0.4}Co_{0.2}Fe_{0.8}O_{3-\delta}$ (LSCF) button electrode (5 mmϕ) was deposited on the other side as a porous cathode by screen-printing with the commercial LSCF paste and post-annealing at 700 °C. Pt mesh was used as a current collector of the cathode. The structural characterization for the cells were conducted by the similar methods as the case with the HMFC.

3.3.3. Electrochemical assessment of a single cell

A single cell thus prepared was mounted in lab-constructed fuel cell test station. The cathode compartment was sealed by molten glass ring gasket. In the case of PAFC, the cathode side was exposed to humidified Ar gases and anode side was exposed to humidified 10%-H_2/Ar mix gases at 700 °C for 12 h before fuel cell tests to covert NiO to metallic Ni and thus prepare porous Ni/$BaZr_{0.1}Ce_{0.7}Y_{0.2}O_{3-\delta}$ cermet anode. All humidified gases were prepared by bubbling in Milli-Q

deionized water at room temperature at a flow rate of 100 sccm, so that the corresponding water partial pressure (p_{H2O}) equals 3 kPa. For fuel cell tests, humidified hydrogen was fed to the anode and humidified air was supplied to cathode side at a rate of 50 sccm. Impedance spectroscopy was conducted with a Solartron 1260A frequency response analyser implemented with a Solartron 1287 potentiostat in the frequency range of 10^6–0.1 Hz with ac amplitude of 30 mV.

3.4. Results

3.4.1. Prediction of effects of proton pumping in HMFCs

Figure 3-4 shows the simulated defect profiles, local ionic conductivities, and performances for a device with a 20-μm-thick membrane at 500 and 600 °C. The primary difference between the HMFC and PAFC is that they exhibit completely opposite $V_O^{\bullet\bullet}$ distributions with respect to the depth from the anode side (**Figure 3-4a** and **b**). At the open-cell voltage (OCV), the $[V_O^{\bullet\bullet}]$ profiles of the PAFC are almost flat from 0 to 0.75, with $[V_O^{\bullet\bullet}]$ decreasing slightly with as one approaches the cathode (i.e., for $L > 0.75$). This is in agreement with the results of simulations performed using the finite volume method.[6,7] Further, this behaviour is actually normal because $[V_O^{\bullet\bullet}]$ must decrease as one moves toward the cathode, owing to the higher oxygen partial pressure (p_{O2}). Meanwhile, the $[V_O^{\bullet\bullet}]$ value of the HMFC decreases sharply as one moves from the higher-p_{O2} side (i.e., the cathode side) to the lower-p_{O2} side (i.e., the anode side) (**Figure 3-4a** and **b**). In the PAFC, the diffusion of the $V_O^{\bullet\bullet}$ defects occurs in accordance with the gradient in the oxygen chemical potential ($\nabla\mu_{O_2}$), which is

given by the difference in the p_{O2} values of the anode and cathode. There is no diffusion of the $V_O^{\bullet\bullet}$ defects in the HMFC owing to the blocking of conduction at the anodic heterointerface. Hence, the $V_O^{\bullet\bullet}$ defects must be redistributed to ensure that the flux of $V_O^{\bullet\bullet}$ remains zero as even as $\nabla\mu_{O_2}$ changes. Consequently, a unique gradient in the concentration of the $V_O^{\bullet\bullet}$ defects ($\nabla[V_O^{\bullet\bullet}]$) develops within the HMFC membrane, wherein $[V_O^{\bullet\bullet}]$ increases logarithmically as one approaches the cathode (**Figure 3-4a** and **b**).

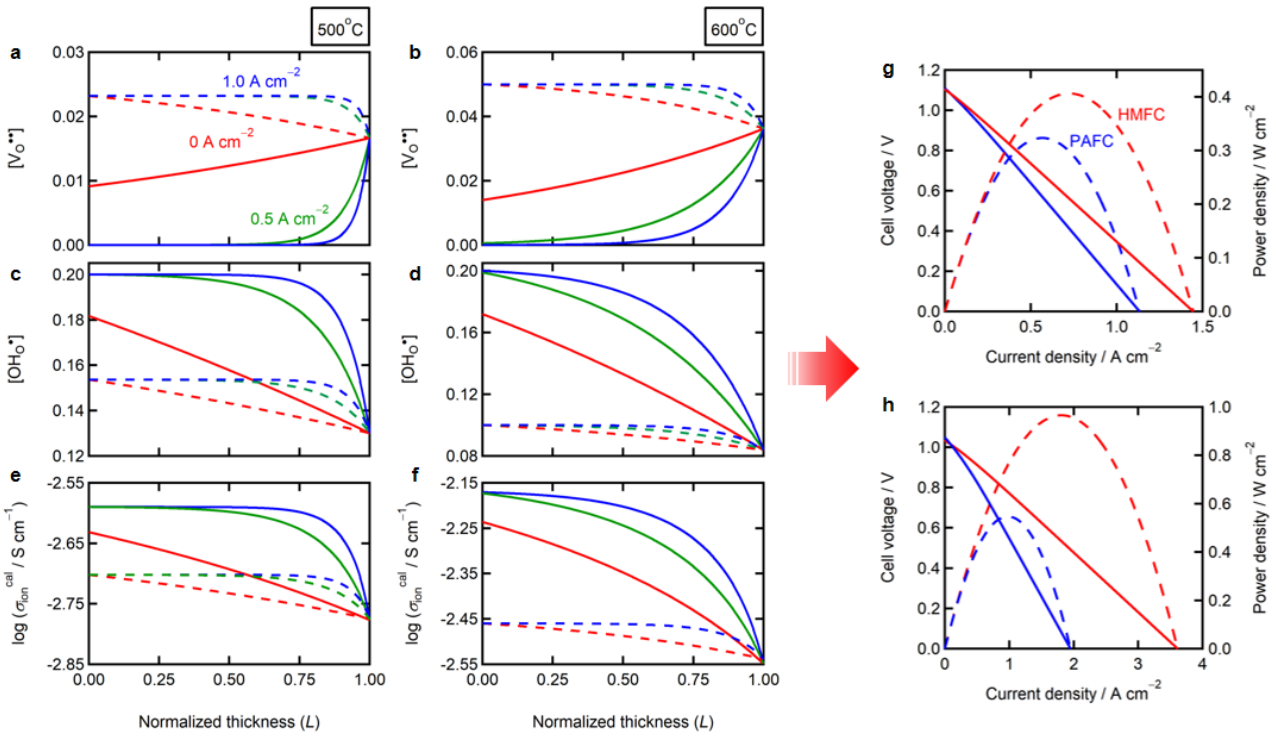

Figure 3-4. Simulated concentration profiles of mobile defects in BZY membranes at 500 and 600 °C. **a, b,** Concentration profiles of oxygen vacancies ($V_O^{\bullet\bullet}$), and **c, d,** protons ($OH_O^{\bullet}$) in 20-μm-thick BZY membrane under various DC conditions. **e, f,** Profiles of local ion conductivity (σ_{ion}) as calculated from $V_O^{\bullet\bullet}$ and $OH_O^{\bullet}$ concentration profiles for 20-μm-thick BZY electrolyte membrane. Normalized thickness is used. In **a-f**, solid lines show results for HMFC while dashed lines show results for PAFC. **g, h,** Ideal *I–V* and *I–P* curves of HMFC and PAFC as calculated from simulated σ_{ion} of 20-μm-thick BZY electrolyte membrane. Solid lines show *I–V* characteristics while dashed lines show *I–P* characteristics at (**g**) 500 and (**h**) 600 °C.

This redistribution of the $V_O^{\bullet\bullet}$ defects significantly modifies the concentration profile of the $OH_O^{\bullet}$ defects because both types of defects are strongly correlated to each other owing to site

constraints and charge neutrality. The $[OH_O^{\bullet}]$ value of the HMFC increases from 0.08 to 0.17 at 600 °C and OCV as *L* changes from 1 to 0 while the that of the PAFC remains constant throughout the membrane (**Figure 3-4d**). Consequently, the former is significantly higher than the latter at the OCV for all *L* values, which indicates that the membrane of HMFC gains protons to compensate for the loss in positive charge owing to the decrease in the number of $V_O^{\bullet\bullet}$ defects. The $O_O^{\bullet}$ defects have no effect on the charge balance because $[O_O^{\bullet}]$ is negligibly small as compared to $[OH_O^{\bullet}]$ and $[V_O^{\bullet\bullet}]$ (**Figure 3-5**). Thus, these simulations confirmed that, in HMFCs, protons are "pumped up" because of $\nabla\mu_{O_2}$ at the expense of the diffusion of the oxide ions.

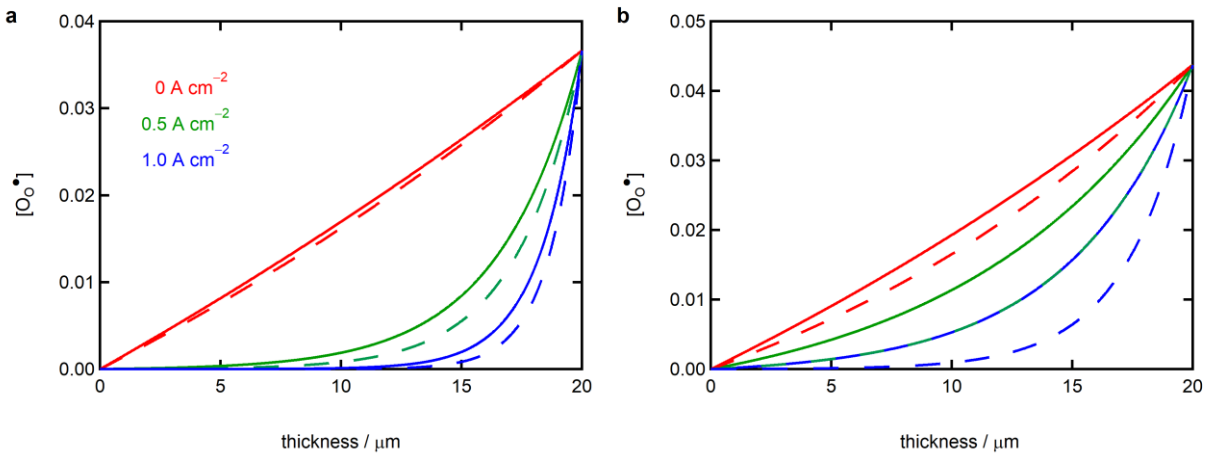

Figure 3-5. Simulated concentration profiles of oxygen-hole ($O_O^{\bullet}$) through electrolyte membrane with several DC conditions at (a) 500 and (b) 600 °C. Solid lines show results of HMFC and dashed lines those of PAFC. The gaseous atmosphere is identical with standard fuel cell atmosphere: 97% H_2 and 3% H_2O at the anode side (left) and 77% N_2, 20% O_2, 3% H_2O at the cathode side (right).

This proton pumping is amplified with an increase in the DC output (**Figure 3-4a**–**f**). As the electrical potential at the surface of the anode side increases in relation to that of the cathode side with the DC output, the HMFC membrane requires an additional concentration gradient, $\nabla[V_O^{\bullet\bullet}]$, to cancel the applied field ($\nabla\phi$). Consequently, the number of $V_O^{\bullet\bullet}$ defects in the BZY bulk decreases further, owing to which the number of $OH_O^{\bullet}$ defects increases with an increase in the DC output (**Figure 3-4a** and **b**). Under DC conditions (1 A cm^{-2}) and at 500 °C, $[V_O^{\bullet\bullet}]$ is nearly zero in the bulk ($L < 0.75$). Hence, $[OH_O^{\bullet}]$ is the highest, that is, that corresponding to the maximum number of $OH_O^{\bullet}$ defects possible (0.2) under site constraints, confirming that an increasingly higher number of protons accumulate in the HMFC membrane with an increase in the DC output owing to the amplified pumping of protons because of $\nabla\phi$.

The ion conductivity of HMFC membranes is greatly improved by the effects of proton pumping. Hereafter, I use the superscript "obs" for the experimentally measured parameter values and "cal" for those calculated. **Figure 3-4e** and **f** show the local ionic conductivity (σ_{ion}^{cal}) values calculated based on the simulated $[V_O^{\bullet\bullet}]$ and $[OH_O^{\bullet}]$ values at each L along with the experimentally determined mobilities,[9] confirming that the local σ_{ion}^{cal} of the HMFC is markedly higher than that of the PAFC for most L values at both 500 and 600 °C. These results prove that the advantage of the ionic conduction resulting from proton pumping outweighs the disadvantage of the blocking of oxide-ion conduction in HMFCs because the proton mobility of BZY is 2–3 orders of magnitude higher than that of the oxide ions.

The local σ_{ion}^{cal} value of the HMFC membrane increases sharply with the DC output, owing to the DC-amplified proton pumping (**Figure 3-4e** and **f**). Hence, the electrolyte resistance (R_b^{cal}), which is calculated by integrating the local σ_{ion} over L, must decrease with the DC current. Meanwhile, the R_b^{cal} value of the PAFC is weakly dependent on the DC current as the $[OH_O^{\bullet}]$ and $[V_O^{\bullet\bullet}]$ profiles of the PAFC does not change significantly with $\nabla\phi$ (**Figure 3-4a**–**d**). Hence, the difference between the R_b^{cal} values of the HMFC and PAFC increases with the DC current, with the former being 0.78 and 0.58 times smaller than the latter at 500 and 600 °C, respectively, under DC conditions (1 A cm^{-2}).

Therefore, the power output of the HMFC was much higher than that of the PAFC, even though they both used similar 20-μm-thick BZY membranes. **Figure 3-4g** and **h** show the ideal *I*–*V* and *I*–*P* characteristics of the HMFC and PAFC at 500 and 600 °C, respectively, as calculated based only on the membrane resistance. The peak power densities (P_{max}^{cal}) of the HMFC at 500 and 600 °C were 1.3 and 1.8 times higher, respectively, than those of the PAFC. This can be attributed to the R_b^{cal} value of the HMFC being lower than that of the PAFC (**Figure 3-4g** and **h**). Hence, the simulations confirmed that the HMFC configuration is advantageous for fuel–electricity conversion in the intermediate temperature range of 500–600 °C as it results in lower ohmic losses.

3.4.2. Fabrication and characterization of protonic fuel cell

To confirm proton pumping in HMFCs, electrochemical assessments were performed on HMFCs comprising $BaZr_{0.1}Ce_{0.7}Y_{0.2}O_{3-\delta}$ (BZCY) thin film membranes and a Pd anode. The BZCY thin films

(thicknesses of 1–3.5 μm) were deposited on a Pd foil (50 μm), which was used as a solid anode, by the reactive cosputtering technique (**Figure 3-6a**). Subsequently, a porous $La_{0.6}Sr_{0.4}Co_{0.2}Fe_{0.8}O_3$ (LSCF) cathode was screen-printed on the film surface. The fabrication procedure has been described elsewhere.[10] Although XRD pattern confirmed the formation of a single-phase perovskite BZCY (**Figure 3-6c**), the chemical composition of the deposited BZCY film was $BaZr_{0.12}Ce_{0.6}Y_{0.25}O_{3-\delta}$, as checked by EPMA, and thus slightly deviated from the target composition ($BaZr_{0.1}Ce_{0.7}Y_{0.2}O_{3-\delta}$), attributed to the element dependence of sputtering yield. TEM confirmed that the densely packed, clack-free thin films of BZCY electrolytes were uniformly formed over a wide area of the Pd foil anode without exfoliation (Inset of **Figure 3-6a**). The films have "bamboo"-like microstructures, in which columnar grains with widths of tens of nanometers grow perpendicular to the substrate and strongly adhere to each other. A high-resolution TEM image reveals that the columnar grain is a single crystalline with preferred growth orientation of (100) direction (**Figure 3-6b**); the interval of lattice fringes, 0.31 nm (**Figure 3-6b**), is equivalent to d_{100} spacing of cubic BZCY perovskites.[11,12]

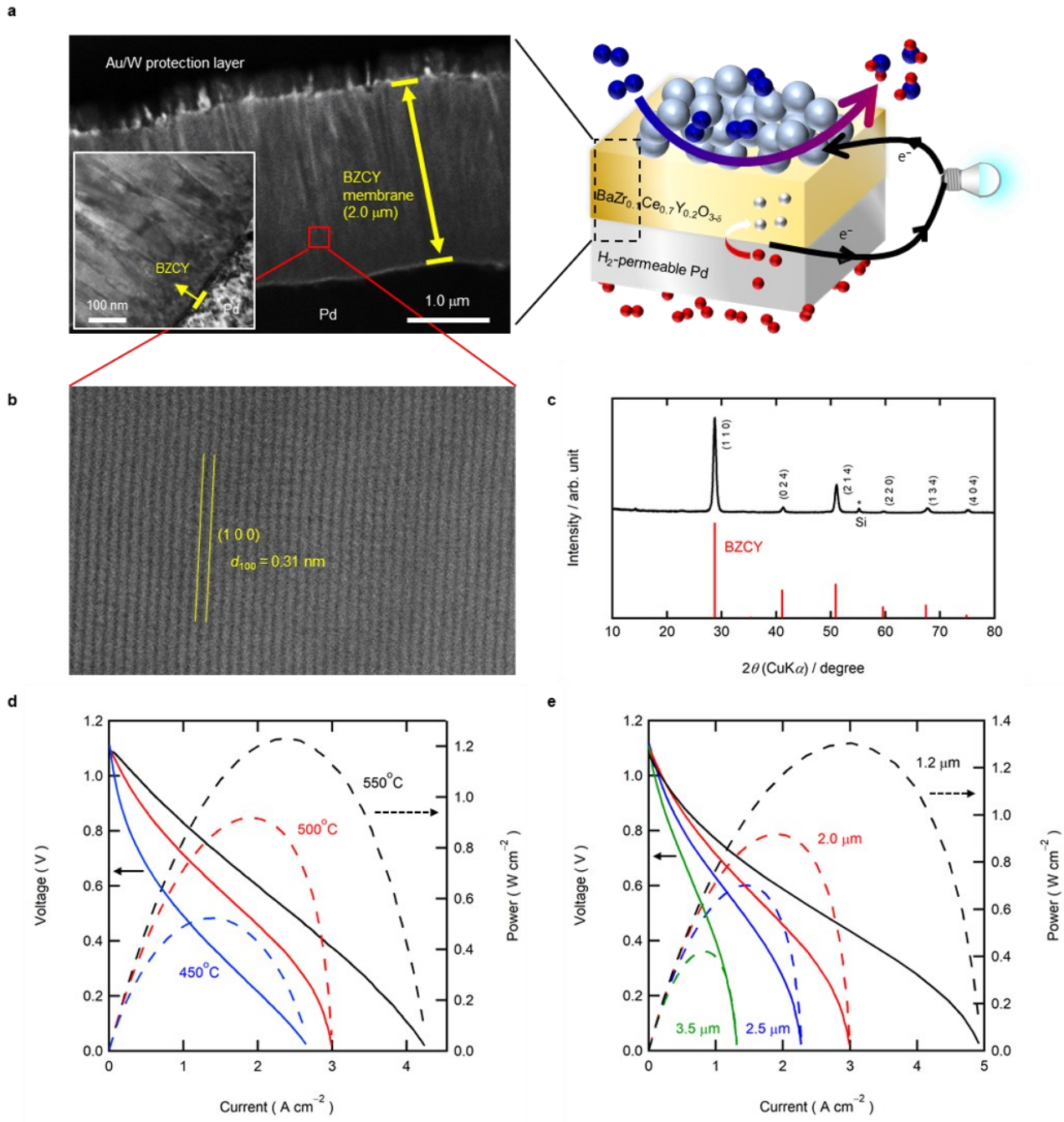

Figure 3-6. Experimental results for the performances of intermediate temperature HMFC. **a,** Transmission electron microscopy (TEM) images of BZCY electrolyte films. Inset shows an expansion near the Pd/BZCY interface. **b,** High resolution TEM image of a columnar grain. **c,** XRD pattern of the thin film. **d,** *I–V* and *I–P* curves of the HMFC with a 2.0-μm-thick BZCY membrane

at various temperatures. **e,** *I–V* and *I–P* curves at 500°C for the HMFC made of electrolyte membranes with different thickness.

The cell with a 2.0-μm-thick film exhibited peak power densities of 0.48, 0.95 and 1.23 W cm^{-2} at 450, 500 and 550 °C, respectively, and an OCV of approximately 1.1 V (**Figure 3-6d**); these are higher than those reported previously for PCFCs for the same temperature range (**Figure 3-1c**). Thus, the cell performance improved with a decrease in the thickness of the electrolyte layer, with the peak power densities at 500 °C being 1.3, 0.95, 0.72 and 0.45 W cm^{-2} for thicknesses of 1.2, 2.0, 2.5 and 3.5 μm, respectively (**Figure 3-6e**). At 500 °C, *I–V* curves shift downward with increasing the current to more than 2 A cm^{-2} (**Figure 3-6d**). This is attributed to the concentration overpotential due to the insufficient hydrogen permeability through the Pd metal support, as reported in the previous work.[13]

The cell resistances were evaluated using electrochemical impedance spectroscopy to further verify the fuel cell performances. In general, Nyquist plots of impedance responses of fuel cells provide the *x*-intercept in a high frequency region, which corresponds to electrolyte resistances. After the intercept, the plots exhibit broad semiarcs mainly owing to the interfacial polarization resistances on the cathode side.[14,15] In the previous report,[13] spectra of the $BaCe_{0.8}Y_{0.2}O_3$-base HMFC were deconvoluted by a systematic survey of the electrochemical impedance responses. The HMFC shows two distinct arcs in Nyquist plots at 600 °C, i.e., a relatively large arc in a high-frequency region at

approximately 10^4–10^1 Hz due to the cathodic interfacial polarization and a small arc in a low-frequency region at approximately 10^1–10^{-1} Hz related to the hydrogen diffusion-limited terms in the Pd anode.[13]

The impedance spectra of HMFC with a 3.5-μm-thick film at 500 °C are shown in **Figure 3-7a**. At 500 °C, the broad semiarc in the frequency region of 10^4–10^1 Hz can be assigned to the cathode contributions because its diameter clearly increases as the oxygen partial pressure (p_{O2}) in the cathode gas decreases and does not change with the hydrogen partial pressure (p_{H2}) in the anode gas (**Figures 3-8a** and **3-8b**). A new semiarc is observed in the frequency region below 10 Hz as p_{H2} decreases to 0.3 p_0 (**Figure 3-8b**), confirming that the anode contributions to overall impedances are rather small under sufficiently high p_{H2}. These features unambiguously prove that the cathode polarization dominantly contributes to the impedance semiarcs of the current HMFC. Thereby, the cathode polarization resistances (R_p^{obs}) are determined from the diameters of the impedance semi-arcs in the region of 10^4–10^1 Hz.

The impedance arcs of the HMFC with a 3.5-μm-thick film were clearly shifted to lower x side with an increase in the DC output, which indicates that the electrolyte resistances (R_b^{obs}) decrease from 0.15 to 0.06 Ω cm^2 with increasing DC current from 0 to 0.8 A cm^{-2} (**Figure 3-7a**). In addition, the impedance arcs shrank significantly by DC output, meaning that R_p^{obs} decreases sharply by DC output, with the R_p^{obs} values being equal to 0.75 Ω cm^2 and 0.18 Ω cm^2 at the OCV and 0.8 A cm^{-2},

respectively (**Figure 3-7a**). The HMFC with a thinner electrolyte film also exhibited DC-dependent reduction of R_p^{obs} (**Figure3-9**).

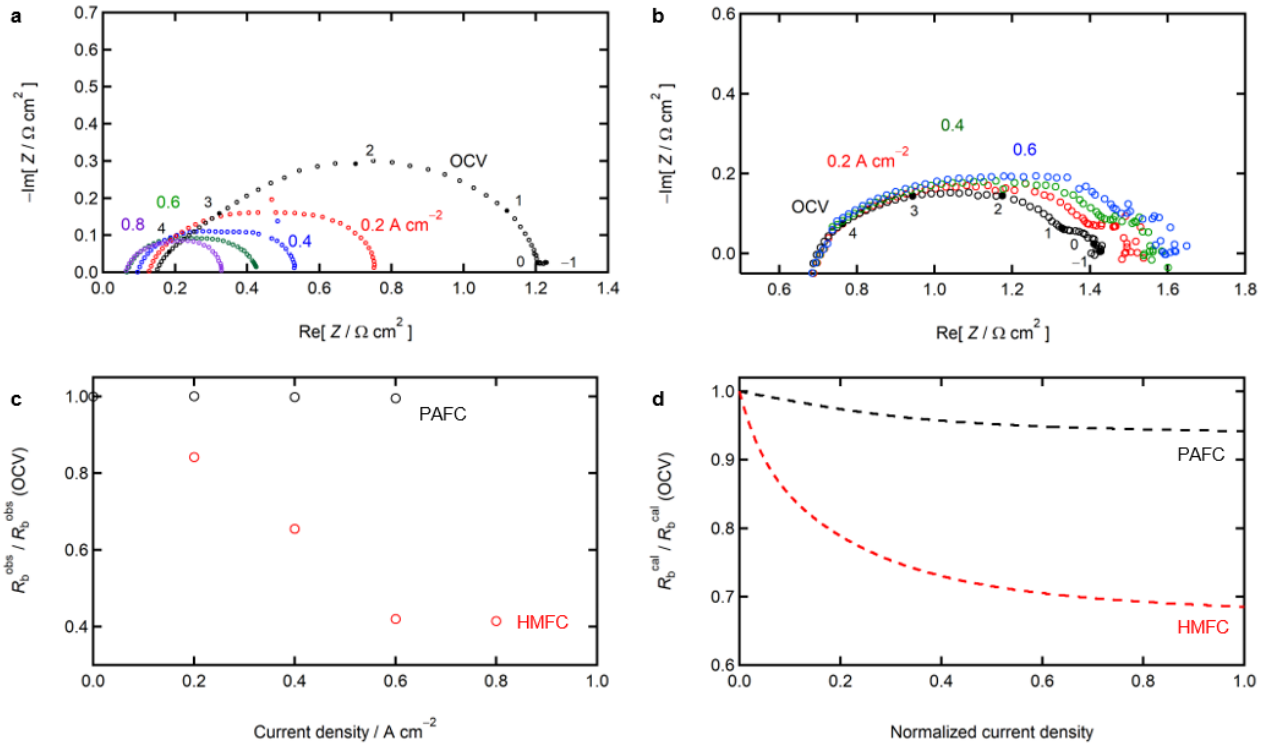

Figure 3-7. DC dependency of ohmic resistances of HMFC and PAFC. **a, b,** Electrochemical impedance spectra of HMFC with (a) a 3.5-μm-thick electrolyte film and (b) PAFC with a 20-μm-thick electrolyte film operating under various DC conditions at 500 °C. **c, d,** Relative ohmic resistances (R_b^{obs} / R_b^{obs} (OCV)) as a function of external current density, measured and simulated for HMFC and PAFC. R_b (OCV) is a R_b in OCV condition, and the superscript 'obs' and 'cal' indicate the measured and simulated ones, respectively.

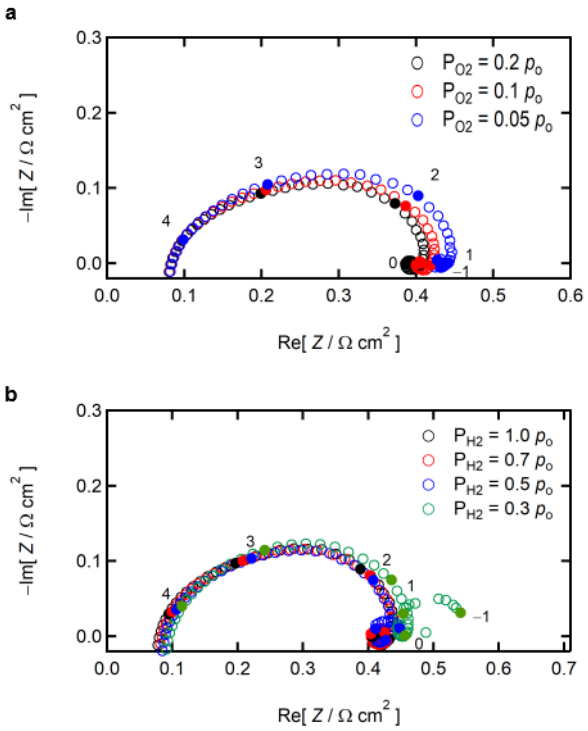

Figure 3-8. Electrochemical impedance spectra in different (a) oxygen partial pressure and (b) hydrogen partial pressure under OCV at 500 °C in HMFC.

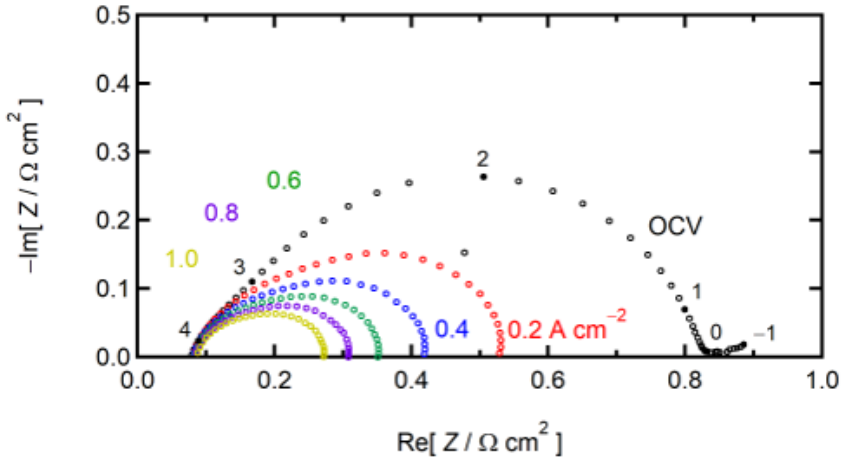

Figure 3-9. Electrochemical impedance spectra of HMFC with a 2.0-μm-thick electrolyte operating under various DC conditions at 500 °C.

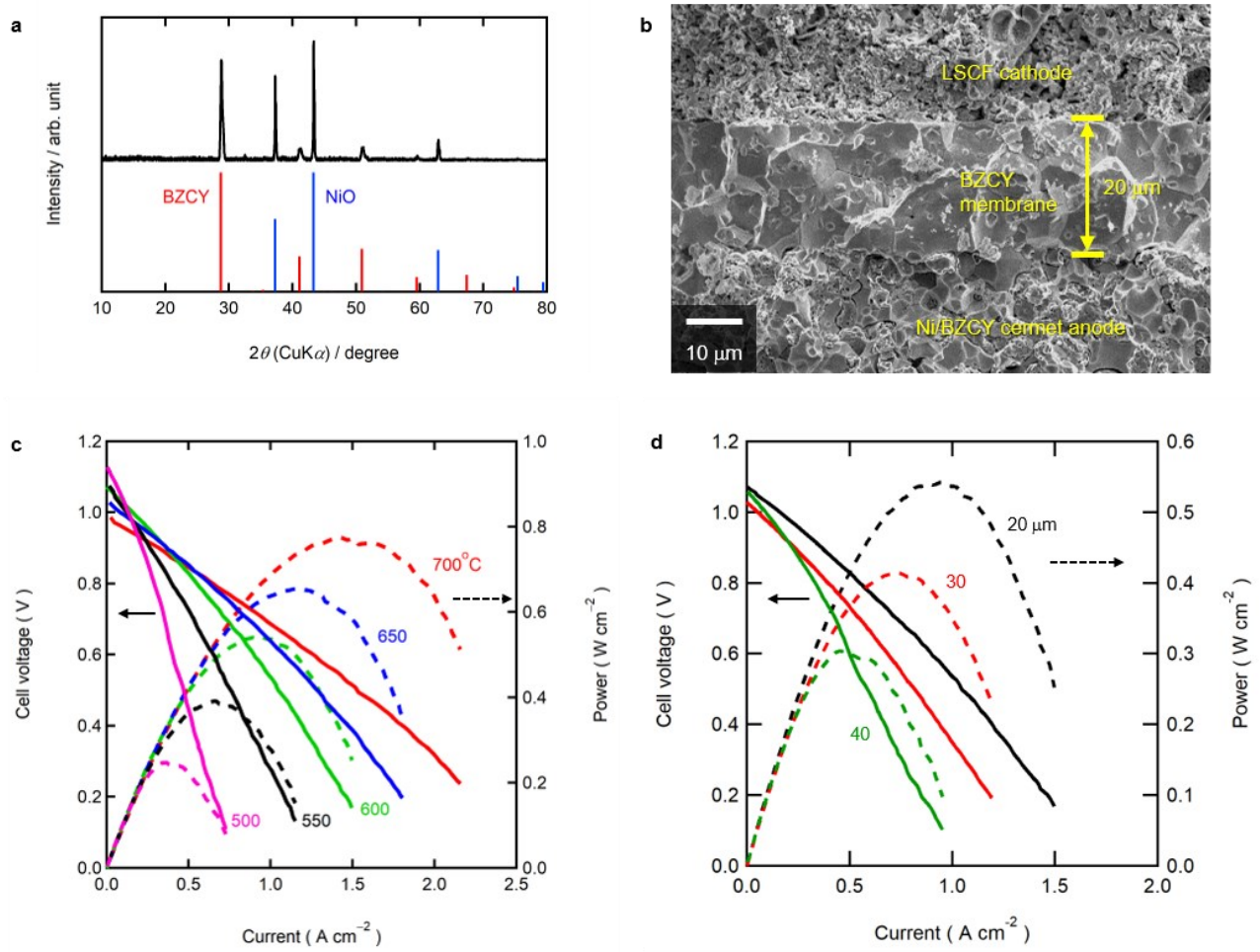

Figure 3-10. Experimental results for the performances of intermediate temperature PAFC. **a,** XRD pattern of prepared cermet anode support. **b,** Cross-section SEM micrograph of the PAFC. **c,** *I–V* and *I–P* curves of the PAFC with a 20-μm-thick BZCY membrane at various temperatures. **d,** *I–V* and *I–P* curves at 600°C for the PAFC made of electrolyte membranes with different thickness.

I also experimentally examined a PAFC with a $BaZr_{0.1}Ce_{0.7}Y_{0.2}O_{3-\delta}$ thin film electrolyte (typical thickness of 20 μm) and porous Ni-cermet anode fabricated through the one-step cofiring process that is described in the chapter 2. An impurity phase was not evident in XRD pattern (**Figure 3-10a**) and

a dense electrolyte film with 20 μm thickness was uniformly formed over a wide area of porous anode support without apparent cracks or pinholes (**Figure 3-10b**). Although there were significant differences in the film thickness and fabrication processes of the HMFC and PAFC, a qualitative comparison of the experimentally determined data would be invaluable for developing a physical model of the energy conversion mechanism of HMFCs. The PAFC showed moderately high performance, exhibiting P_{max}^{obs} values of 0.78, 0.66, 0.54, 0.39 and 0.25 W cm^{-2} at 700, 650, 600, 550 and 500 °C, respectively (**Figure 3-10c**). Further, R_b^{obs} increased linearly with the thickness, meaning that the performance decreased in a similar manner (**Figures 3-10d**, **3-11b** and **3-11c**).

The DC dependence of R_b^{obs} and R_p^{obs} of PAFC is quite different from that of HMFC. The impedance spectra of PAFC with a 20-μm-thick film do not cause the shifts of the *x*-intercepts with DC current (**Figure 3-7b**), proving that R_b^{obs} of the PAFC are almost constant at 0.7 Ω cm^2 under any DC conditions. The impedance semiarcs, which can be also assigned to the cathode polarization resistance,[14,15] increase significantly with DC current. Thus, R_p^{obs} increases from 0.75 to 0.93 Ω cm^2 with an increase in the DC current from 0 to 0.6 A cm^{-2} at 500 °C. A similar DC dependence of R_p^{obs} is also observed at 600 °C (**Figure 3-12**).

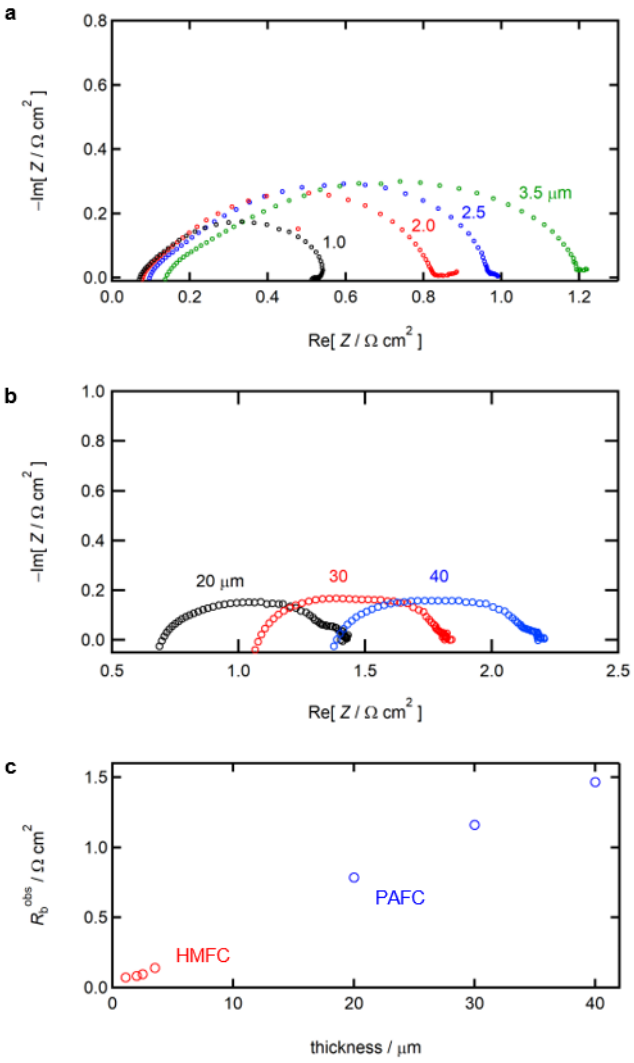

Figure 3-11. Thickness dependency of ohmic resistances. **a, b,** Electrochemical impedance spectra of (a) HMFCs and (b) PAFCs with BZCY membranes of various thicknesses at OCV and 500 °C. **c,** Plots of thickness vs. electrolyte resistances (R_b^{obs}) as determined from corresponding impedance spectra at 500 °C and OCV.

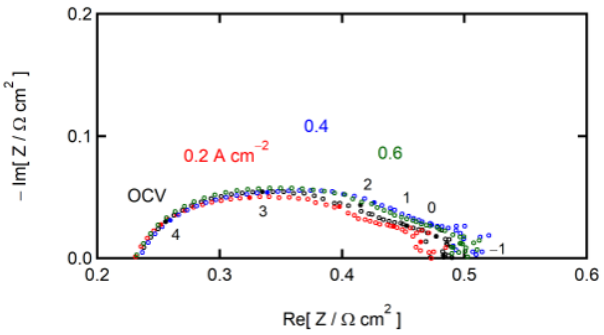

Figure 3-12. Electrochemical impedance spectra of PAFC with a 20-μm-thick electrolyte operating at 600 °C under various DC conditions.

3.5. Discussion

3.5.1 Verification of effects of proton pumping in HMFCs

The simulations could predict the current dependency of R_b^{obs} for the HMFC and PAFC with accuracy (**Figures 3-7c** and **3-7d**). As mentioned above, the R_b^{obs} value of the HMFC decreased sharply with the DC current while that of the PAFC remained unchanged (**Figure 3-7c**). This was in keeping with the simulation results (**Figure 3-7d**) and suggests that the number of protons in the bulk increased with $\nabla\phi$, thus providing clear evidence for the phenomenon of proton pumping in HMFCs.

The actual HMFC shows drop of 60% in the relative resistances, R_b^{obs} / R_b^{obs} (OCV), with increasing DC current, which is larger than the corresponding value (32%) for the simulation, R_b^{cal} / R_b^{cal} (OCV). This is attributed to the different chemical composition of the electrolyte used in experimental and simulation. The oxides including high concentration of $V_O^{\bullet\bullet}$ can trigger pronounced proton pumping because such oxides are capable of accommodating large excess of $OH_O^{\bullet}$ defects.

The sputter-deposited electrolyte film, i.e., $BaZr_{0.12}Ce_{0.65}Y_{0.25}O_{3-\delta}$, is expected to retain larger oxygen vacancy concentration. Thus, it is capable of accommodating larger excess protons by proton pumping than BZY. Hence, the former must show enhanced reduction of the electrolyte resistances by DC current. In fact, the R_b^{obs} values of the HMFC membranes were significantly lower than those of PCFCs with membranes with a thickness of less than 5 μm[1,3,16–21] and thus is lower than the target ohmic resistance (0.15 Ω cm^2),[14] as shown in **Figure 3-13**.

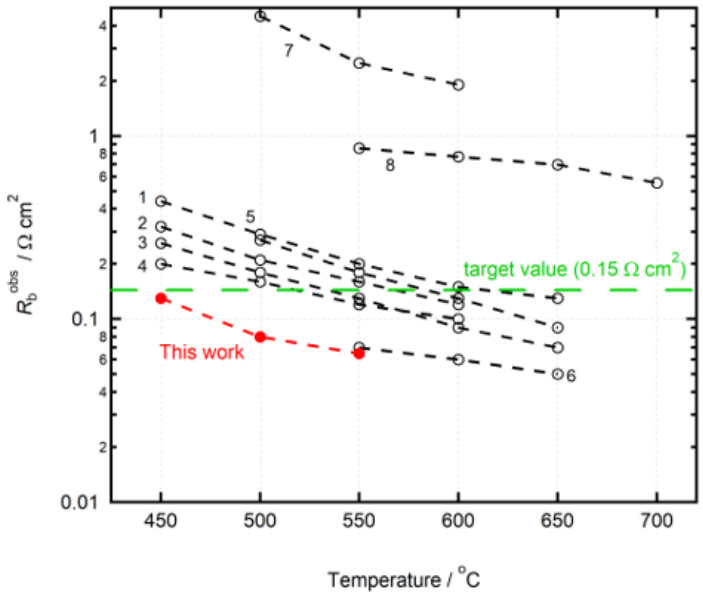

Figure 3-13. Ohmic resistances of HMFC and reported values for thin film PCFCs with BZCY membranes with thicknesses lower than 5 μm. (1. Bae et al.[18], 2. Bae et al.[17], 3. An et al.[1], 4. Bae et al.[16], 5. Choi et al.[19], 6. Bae et al.[3], 7. Pergolesi et al.[20], 8. Nasani et al.[21])

3.5.2. Enhanced cathode reaction kinetics owing to proton pumping

The DC dependences of cathode polarization resistances (R_p^{obs}) were different for the two cells. R_p^{obs} of HMFC decreases sharply with an increase in the DC current while R_p^{obs} of PAFC increases (**Figure 3-14d**). Recently, an elementary reaction model has been proposed for the cathode reactions that occur in PCFCs.[22] As per this model, the reaction process consists of the following eight steps[19,22]: 1) the dissociative adsorption of O_2 molecules, 2) the first transfer of electrons to the oxygen adatoms, 3) the diffusion of the adsorbed O^- towards the TPB, 4) the second transfer of electrons to the absorbed O^-, 5) the interfacial transfer of H^+ from the electrolyte to the TPB, 6) the association of the adsorbed O^{2-} and H^+ at the TPB, 7) the association of the OH^- and H^+ at the TPB, and 8) the desorption of the formed H_2O (**Figure 3-14a**). Of these eight steps, the interfacial proton transfer step (i.e., step 5) is considered as the rate-determining one for the cathode reactions that occur in PCFCs because the confined TPB zone requires the relatively long-distant transfer of H^+ near the cathodic surface.[22,23] This is consistent with the DC-dependent increase in the R_p^{obs} of the PAFC (**Figure 3-14d**), as mass-transfer-limited reactions require larger overpotentials to increase the DC output (**Figure 3-14b**).[24] Meanwhile, the R_p^{obs} of the HMFC decreased with the DC output, meaning that the charge-transfer steps (i.e., steps 2 and 4) control the overall reaction rate since the kinetics of these steps are in terms of $\exp(-EF/2RT)$ (electrochemical potential, E; Faraday constant, F; and gas constant, R) (**Figure 3-14b**). Hence, the related R_p^{obs} decreases with the cathode overpotential, that is, the DC output. These results confirm that the interfacial transfer of H^+ is fast and thus does not

limit the cathode reaction rates in HMFCs even though they may have the same cathode/electrolyte interfaces as those in PAFCs.

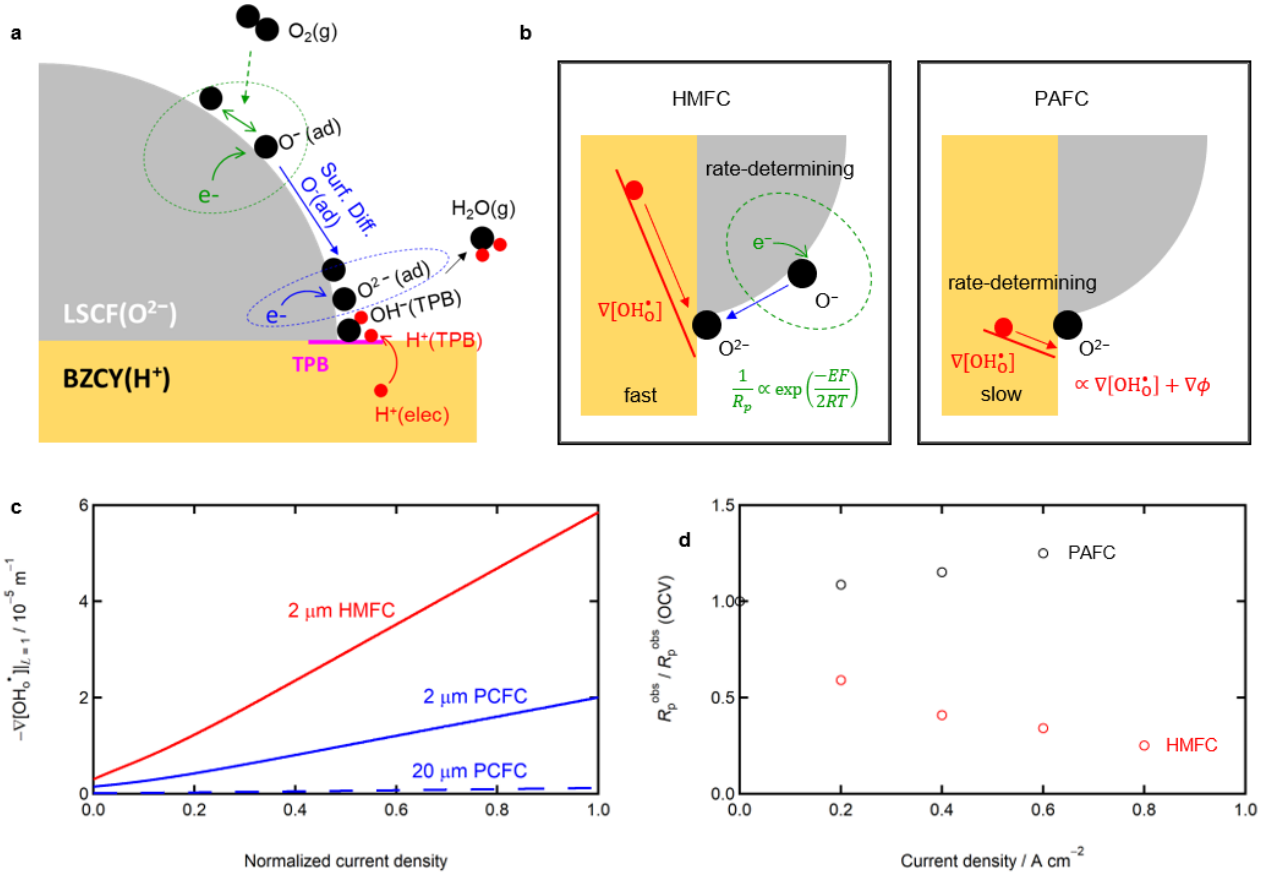

Figure 3-14. DC dependency of polarization resistances of HMFC and PAFC. **a,** the schematic cathode electrode reaction model. **b,** correlation of proton concentration gradient at cathode surface with rate-determining steps in cathodic reaction in both HMFC and PAFC. **c,** proton concentration gradient ($\log(-\nabla[OH_O^\bullet])$) at cathode surface calculated for HMFC and PAFC at 500°C and **d,** External-current dependency of relative polarization resistances (R_p^{obs} / R_p^{obs} (OCV)) measured for HMFC and PAFC.

The "negative" concentration gradient of the $OH_O^{\bullet}$ defects ($\nabla[OH_O^{\bullet}]$) in the vicinity of the cathode side surface is crucial for promoting the diffusion of protons toward the TPB. The value of $\nabla[OH_O^{\bullet}]$ calculated from $[OH_O^{\bullet}]$ at L = 1 confirmed that the HMFC membranes exhibited more favourable $\nabla[OH_O^{\bullet}]$ gradients than did those of the PAFC for interfacial proton diffusion near the TPB (**Figure 3-14c**). For the same thickness, the values for the HMFC membranes were much higher than those of the PCFC membranes (**Figure 3-14c**). This was because of the formation of a relatively large $[OH_O^{\bullet}]$ gap between the bulk and the cathode side surface owing to proton pumping (**Figures 3-4c** and **3-4d**). For a 2-μm-thick HMFC membrane, the gradient, that is, $\nabla[OH_O^{\bullet}]$, in the vicinity of the cathode became steeper with an increase in the DC current (**Figure 3-14c**), owing to the increase in proton pumping with $\nabla\phi$. This probably led to the rapid interfacial transfer of H^+, resulting in a large DC output. However, the increase in $\nabla[OH_O^{\bullet}]$ near the cathode with the DC output was less pronounced in the PAFC with a 20-μm-thick membrane (**Figure 3-14c**). Consequently, the $\nabla[OH_O^{\bullet}]$ values of the 20-μm-thick PAFC membranes were 40 and 60 times smaller than those of the 2-μm-thick HMFC membrane at 0 and 1.0 A cm^{-2}, respectively. This was because the contribution of the interfacial proton transfer on R_p^{obs} in PAFCs and HMFCs is large and small, respectively.

The experimental and simulation results unambiguously confirmed that the HMFC configuration is better suited for power generation in the intermediate temperature around 500 °C as it results in significantly lower polarization and electrolyte resistances. Based on the aforementioned results, it can be concluded that the simulated defect profiles were in accordance with not only the electrolyte

resistance but also the cathode polarization resistance of the HMFC, thus confirming the crucial role played by the modified defects profile in determining the power generation performance. It can also be concluded that the blocking of the oxide ions at the heterointerface boosts the energy conversion efficiency of HMFCs.

3.5.3. Proton pumping model

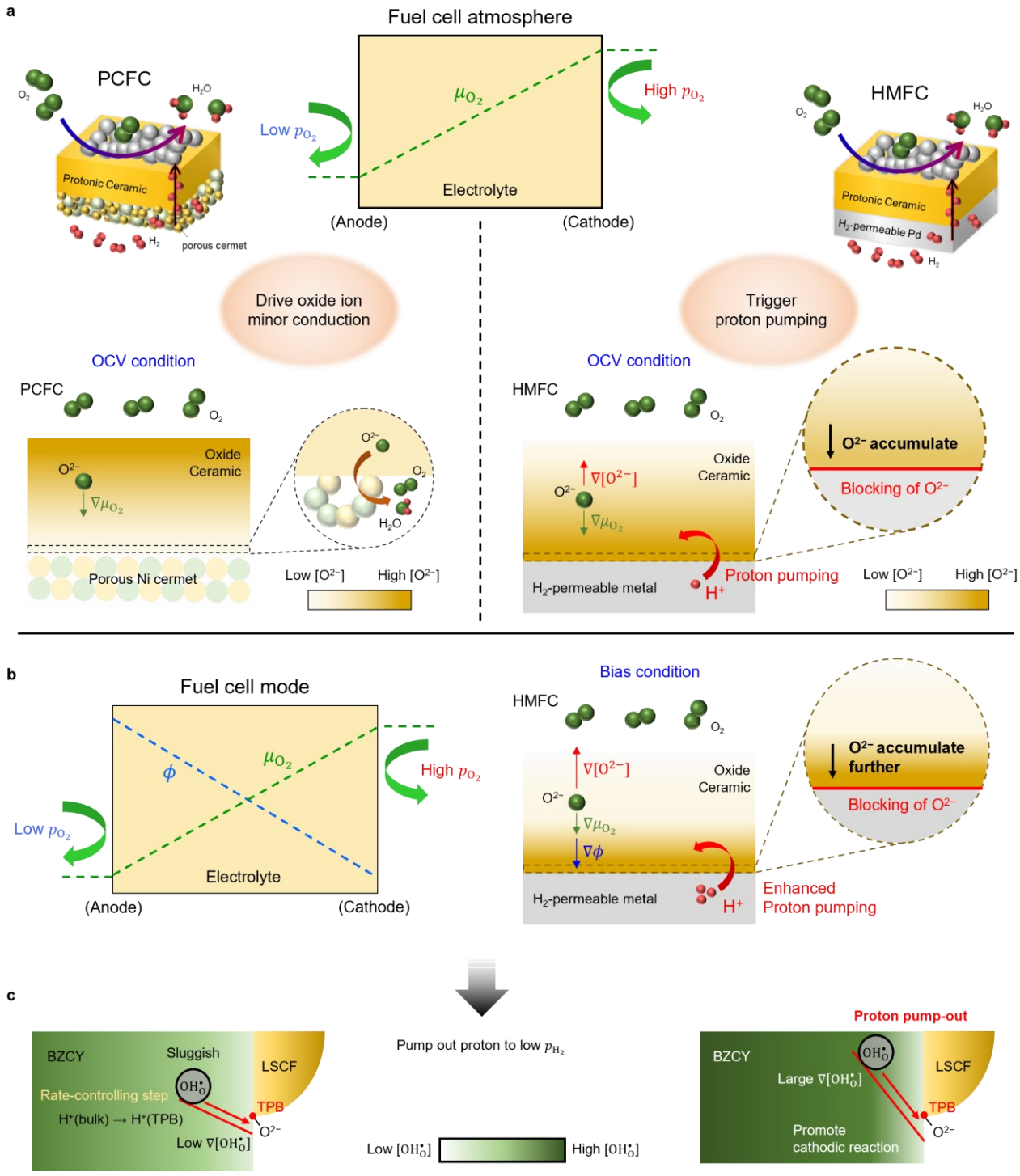

Figure 3-15. Proton pumping in HMFC, triggered by the blocking of secondary (oxide-ion) conduction at oxide ceramic/metal heterointerfaces. (a) Comparison of [O^{2-}] profiles between PCFC and HMFC and proton pumping in HMFC driven by harnessing the oxygen chemical potential (μ_{O2})

under OCV. (b) Enhancement o proton pumping in HMFC by applied electrostatic potential (ϕ). (c) Proton pump-out toward cathode via water formation reaction.

It has been demonstrated that oxide-ion blocking at the anodic heterointerface results in an increase in the number of protons in the cell membrane. A simplified model of this phenomenon is displayed in **Figure 3-15**. In the HMFC, the number of $V_O^{\bullet\bullet}$ defects decrease rapidly as one moves away from the cathode and is very small in the bulk because of the blocking of the oxide ions. This decline in $[V_O^{\bullet\bullet}]$ leads to an increase in $[OH_O^{\bullet}]$ owing to charge neutrality. Hence, in the HMFC, the "pumping up" of protons occurs with a decrease in the bulk resistance. Based on this fact, one can say that the HMFC membrane is "frustrated", as it is highly hydrated, with $[OH_O^{\bullet}]$ in the bulk being higher than that of the BZCY membrane equilibrated with wet air. Hence, a steep gradient, $\nabla[OH_O^{\bullet}]$, develops near the cathode side surface to "pump out" the protons (and thus ease the frustration) at the cathode side via water formation reactions (**Figure 3-15c**). This promotes the interfacial diffusion of proton towards the TPB for the cathode reactions. These phenomena of proton pumping are aided by the DC output as a greater number of $OH_O^{\bullet}$ defects accumulate within the membrane with an increase in $\nabla\phi$ (**Figure 3-15b**).

3.5.4. Thermodynamic understanding of power generation mechanism of HMFC

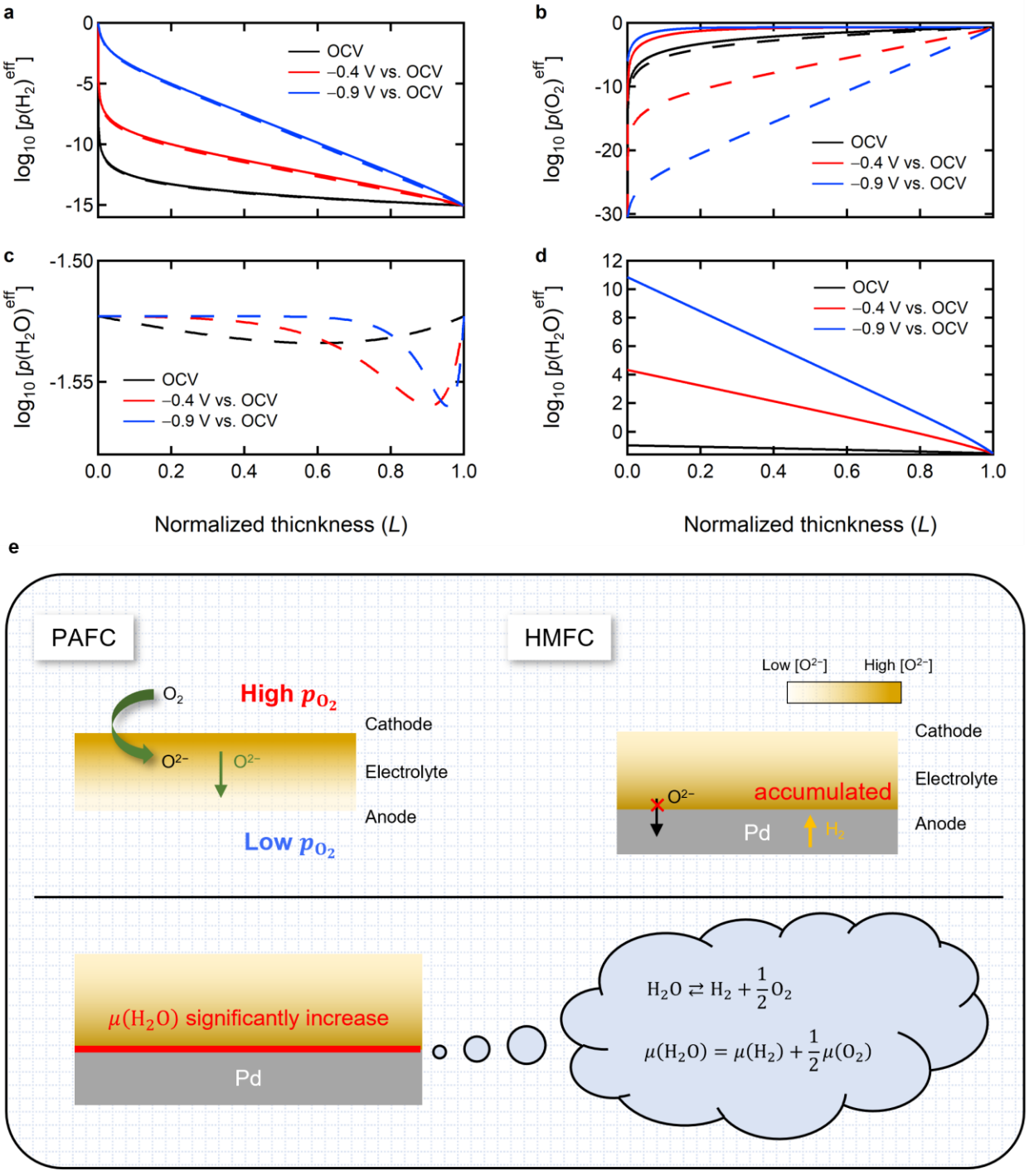

Figure 3-16. Simulated effective partial pressure profiles of each gas within membranes of PAFC and HMFC under various cell bias conditions and the thermodynamic understanding of power generation mechanism of HMFC: Proton pumping. Profiles of logarithmic effective partial pressure

of (**a**) H_2, $\log_{10}[p(H_2)^{eff}]$, (**b**) O_2, $\log_{10}[p(O_2)^{eff}]$, (**c**,**d**) H_2O, $\log_{10}[p(H_2O)^{eff}]$ under standard fuel cell atmosphere: Wet H_2 (H_2O/H_2 = 3/97) at anode and wet air ($H_2O/O_2/Ar$ = 3/19.4/77.6) at 500 °C. Solid lines show results for HMFC while dashed ones do those for PAFC. The cell bias was determined by subtracting the OCV from the corresponding cell voltage, representing the relative potential of the anode to cathode. (**e**) Summary of thermodynamic elucidation in cartoon form.

Figure 3-16 shows simulated effective partial pressure profiles of each gas within membranes, which is related to the chemical potentials with the equation of $\mu_k = \mu_k^\circ + RT\ln p_k^{\mathrm{eff}}$; μ_k° is chemical potential under standard conditions for species *k*. As shown in **Figure 3-16**, hydrogen chemical potentials, μ_{H2}, are similar each other between PAFC and HMFC, but oxygen chemical potentials, μ_{O2}, are higher in HMFC in PAFC under every bias condition and the differences are enhanced by cell bias due to the difference in concentration profiles of oxide ion. The increment of μ_{O2} in HMFC results in significant enhancement of chemical potential of water vapor, μ_{H2O}, as the chemical potentials water vapor are determined by both μ_{H2} and μ_{O2}, as shown in **Figure 3-16e**. Thus, as shown in **Figures 3-16c** and **3-16d**, the calculated p_{H2O}^{eff} are much higher in HMFC than in PAFC. The p_{H2O}^{eff} at the anode is about 6 orders of magnitude higher in HMFC than that in PAFC at the −0.4 V vs. OCV, leading to significant enhancement of effective μ_{H2O} at the anode in HMFC; this induce

proton pumping. These findings show that the mechanism of power generation in HMFC — proton pumping — can be thermodynamically understood by enhanced μ_{H2O} at the anodic heterointerfaces.

3.6. Conclusion

In conclusion, the superior performance of HMFCs can be attributed to their oxygen vacancy and proton defect profiles, which are determined by the blocking of the secondary conduction, namely, that related to the oxide ions, in the mixed-ionic-conduction electrolyte membrane. It is worth noting that HMFCs based on nonstoichiometric oxides are also feasible since oxides that exhibit oxide-ion conduction and hydration ability could also result in proton pumping owing to the oxygen chemical potential and electrostatic potential within the fuel cell. The results of this study should help improve the power generation performance of protonic oxide fuel cells at temperatures lower than 500 °C.

3.7. References

1. H. An, H. W. Lee, B. K. Kim, J. W. Son, K. J. Yoon, H. Kim, D. Shin, H. I. Ji and J. H. Lee, "A 5×5 cm^2 protonic ceramic fuel cell with a power density of 1.3 W cm^{-2} at 600 °C" *Nat. Energy* **2018**, 3, 870.

2. S. Choi, C. Kucharczyk, Y. Liang, X. Zhang, I. Takeuchi, H. I. Ji and S. M. Haile, "Exceptional Power Density and Stability at Intermediate Temperatures in Protonic Ceramic Fuel Cells" *Nat. Energy* **2018**, 3, 202.

3. K. Bae, D. H. Kim, H. J. Choi, J. W. Son and J. H. Shim, "High-Performance Protonic Ceramic Fuel Cells with 1 μm Thick Y:Ba(Ce, Zr)O_3 Electrolytes" *Adv. Energy Mater.* **2018**, *8*, 1801315.

4. N. Ito, M. Iijima, K. Kimura and S. Iguchi, "New Intermediate Temperature Fuel Cell with Ultra-Thin Proton Conductor Electrolyte" *J. Power Sources* **2005**, 152, 200.

5. R. J. Kee, H. Zhu, B. W. Hildenbrand, E. Vøllestad, M. D. Sanders and R. P. O'Hayre, "Modeling the Steady-State and Transient Response of Polarized and Non-Polarized Proton-Conducting Doped-Perovskite Membranes" *J. Electrochem. Soc.* **2013**, 160, F290.

6. H. Zhu, R. J. Kee, "Membrane Polarization in Mixed-Conducting Ceramic Fuel Cells and Electrolyzers" *Int. J. Hydrogen Energy* **2016**, 41, 2931.

7. H. Zhu, S. Ricote, C. Duan, R. P. O'Hayre, D. S. Tsvetkov and R. J. Kee, "Defect Incorporation and Transport within Dense $BaZr_{0.8}Y_{0.2}O_{3-\delta}$ (BZY20) Proton-Conducting Membranes" *J. Electrochem. Soc.* **2018**, 165, F581.

8. C. Duan, R. Kee, H. Zhu, N. Sullivan, L. Zhu, L. Bian, D. Jennings and R. O'Hayre, "Highly efficient reversible protonic ceramic electrochemical cells for power generation and fuel production" *Nat. Energy* **2019**, 4, 230.

9. H. Zhu, S. Ricote, W. G. Coors and R. J. Kee, "Interpreting Equilibrium-Conductivity and Conductivity-Relaxation Measurements to Establish Thermodynamic and Transport Properties for Multiple Charged Defect Conducting Ceramics" *Faraday Discuss.* **2015**, 182, 49.

10. Y. Aoki, T. Yamaguchi, S. Kobayashi, D. Kowalski, C. Zhu and H. Habazaki, "High-Efficiency Direct Ammonia Fuel Cells Based on $BaZr_{0.1}Ce_{0.7}Y_{0.2}O_{3-\delta}$/Pd Oxide-Metal Junctions" *Global Challenges* **2018**, 2, 1700088.

11. B. Wang, L. Bi and X. S. Zhao, "Exploring the Role of NiO as a Sintering Aid in $BaZr_{0.1}Ce_{0.7}Y_{0.2}O_{3-\delta}$ Electrolyte for Proton-Conducting Solid Oxide Fuel Cells" *J. Power. Sources* **2018**, 399, 207.

12. B. Wang, X. Liu, L. Bi and X. S. Zhao, “Fabrication of High-Performance Proton-Conducting Electrolytes from Microwave Prepared Ultrafine Powers for Solid Oxide Fuel Cells” *J. Power. Sources* **2019**, 412, 664.

13. Y. Aoki, S. Kobayashi, T. Yamaguchi, E. Tsuji, H. Habazaki, K. Yashiro, T. Kawada and T. Ohtsuka, “Electrochemical Impedance Spectroscopy of High-Efficiency Hydrogen Membrane Fuel Cells Based on Sputter-Deposited $BaCe_{0.8}Y_{0.2}O_{3-\delta}$ Thin Films” *J. Phys. Chem. C* **2016**, *120*, 15976.

14. Z. Gao, L. V. Mogni, E. C. Miller, J. G. Railsback and S. A. Barnett, “A Perspective on Low-Temperature Solid Oxide Fuel Cells” *Energy Environ. Sci.* **2016**, 9, 1602.

15. A. Jun, J. Kim, J. Shin and G. Kim, “Perovskite as a Cathode Material: A Review of Its Role in Solid-Oxide Fuel Cell Technology” *ChemElectroChem* **2016**, 3, 511.

16. K. Bae, D. Y. Jang, H. J. Choi, D. Kim, J. Hong, B. K. Kim, J. H. Lee, J. W. Son and J. H. Shim, “Demonstrating the Potential of Yttrium-Doped Barium Zirconate Electrolyte for High-Performance Fuel Cells” *Nat. Commun.* **2017**, 8, 14553.

17. K. Bae, S. Lee, D. Y. Jang, H. J. Kim, H. Lee, D. Shin, J. W. Son and J. H. Shim, “High-Performance Protonic Ceramic Fuel Cells with Thin-Film Yttrium-Doped Barium Cerate–Zirconate Electrolytes on Compositionally Gradient Anodes” *ACS Appl. Mater. Interfaces* **2016**, 8, 9097.

18. K. Bae, H. S. Noh, D. Y. Jang, J. Hong, H. Kim, K. J. Yoon, J. H. Lee, B. K. Kim, J. H. Shim and J. W. Son, “High-Performance Thin-Film Protonic Ceramic Fuel Cells Fabricated on Anode Supports with a Non-Proton-Conducting Ceramic Matrix” *J. Mater. Chem. A* **2016**, 4, 6395.

19. S. M. Choi, H. An, K. J. Yoon, B. K. Kim, H. W. Lee, J. W. Son, H. Kim, D. Shin, H. I. Ji and J. H. Lee, “Electrochemical Analysis of High-Performance Protonic Ceramic Fuel Cells Based on a Columnar-Structured Thin Electrolyte” *Appl. Energy* **2019**, *233–234,* 29.

20. D. Pergolesi, E. Fabbri and E. Traversa, “Chemically Stable Anode-Supported Solid Oxide Fuel Cells Based on Y-Doped Barium Zirconate Thin Films Having Improved Performance” *Electrochem. Commun.* **2010**, 12, 977.

21. N. Nasani, D. Ramasamy, S. Mikhalev, A. V. Kovalevsky, D. P. Fagg, “Fabrication and Electrochemical Performance of a Stable Anode Supported Thin $BaCe_{0.4}Zr_{0.4}Y_{0.2}O_{3-\delta}$ Electrolyte Protonic Ceramic Fuel Cell” *J. Power Sources* **2015**, 278, 582.

22. F. He, T. Wu, R. Peng, C. Xia, “Cathode Reaction Models and Performance Analysis of $Sm_{0.5}Sr_{0.5}CoO_{3-\delta}$–$BaCe_{0.8}Sm_{0.2}O_{3-\delta}$ Composite Cathode for Solid Oxide Fuel Cells with Proton Conducting Electrolyte” *J. Power Sources* **2009**, 194, 263.

23. X. Wang, Z. Ma, T. Zhang, J. Kang, X. Ou, P. Feng, S. Wang, F. Zhou and Y. Ling, “Charge-Transfer Modeling and Polarization DFT Analysis of Proton Ceramic Fuel Cells Based on Mixed

Conductive Electrolyte with the Modified Anode–Electrolyte Interface" *ACS Appl. Mater. Interfaces* **2018**, 10, 35047.

24. Bard, A. J.; Faulkner, L. R. Electrochemical Methods: Fundamentals and Applications, 2nd edition. JOHN WILEY & SONS, INC. (2000).

Chapter 4

Enhancement of proton pumping in hydrogen-permeable metal-support-type fuel cell with highly-oxygen deficient electrolytes

4.1. Objective of chapter 4

In the chapter 3, it is demonstrated that electrolyte membranes on hydrogen-permeable metal-support-type fuel cells (HMFCs) are capable of exhibiting higher proton conductivity than those on porous-anode-support-type fuel cells (PAFCs) owing to a thermodynamic process called 'proton pumping,' triggered by the retardation of the minor oxide ion conduction at hydrogen permeable metal and oxide membrane heterointerfaces.

This finding provides a hint for realizing more efficient fuel cells with proton pumping: A greater counter O^{2-} flux is achieved with more $V_O^{\bullet\bullet}$, so HMFCs comprising highly oxygen-deficient oxide electrolytes could undergo enhanced proton pumping. Among various proton conductors, the $BaZr_{1-x}Sc_xO_{3-x/2}$ family is an attractive target for verifying this concept because it allows a relatively wide range of x, that is, $0 \leq x \leq 0.6$.

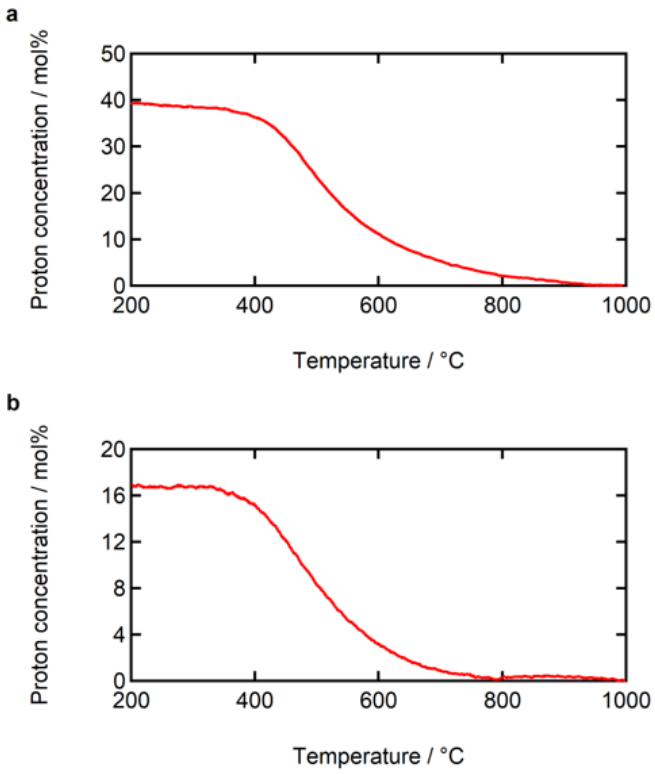

Figure 4-1. Proton concentrations of (a) Sc50 and (b) Sc20 electrolyte materials, determined from the mass gains via hydration with cooling from 1000 to 200 °C in wet 2% O_2/Ar ($pH_2O = 0.023p_0$).

Figure 4-1 shows $[OH_O^{\bullet}]$ of x = 0.5 (Sc50) and 0.2 (Sc20) electrolytes, measured by thermogravimetry (TG). Sc50 electrolyte possesses an $[OH_O^{\bullet}]$ of 0.36, whereas Sc20 electrolyte has an $[OH_O^{\bullet}]$ of 0.15 at 400 °C under a wet atmosphere ($pH_2O = 0.023\ p_0$). Assuming that the hole concentration is very low, Sc50 and Sc20 electrolytes have $[V_O^{\bullet\bullet}]$ of 0.07 and 0.025, respectively, at 400 °C, confirming that Sc50 retains a greater $[V_O^{\bullet\bullet}]$ than Sc20 in a wet atmosphere.

In this chapter, the cathode reaction resistances of the $BaZr_{1-x}Sc_xO_{3-x/2}$ base HMFC were investigated in terms of proton pumping by comparing the behavior of x = 0.2 and 0.5. As a result, it is demonstrated that HMFC can drive the fast cathode reaction cycles in the TPBs without long-range

diffusion of O adatoms because of the development of a very steep proton concentration gradient at the cathode side, and the interfacial proton diffusion thus promotes the regeneration of the catalytic sites at the TPB. A systematic study combining numerical simulations and electrochemical analysis of cells with $BaZr_{0.5}Sc_{0.5}O_{3-\delta}$ (Sc50) and $BaZr_{0.8}Sc_{0.2}O_{3-\delta}$ (Sc20) electrolytes verified that HMFCs comprising highly oxygen-deficient oxide electrolytes could increase the concentration gradient at the cathode/electrolyte interfaces on the application of a bias voltage. Thus, the reaction resistance of a Sc50-cell with the conventional $La_{0.6}Sr_{0.4}Co_{0.2}Fe_{0.8}O_{3-\delta}$ (LSCF) cathode decreased from 1.35 to 0.54 Ω cm^2 with increasing cell bias from open circuit voltage (OCV) to −0.4 V at 400 °C.

4.2. Simulation of proton pumping

The local concentration of three mobile defects: Oxygen vacancies $V_O^{\bullet\bullet}$, proton defects $OH_O^{\bullet}$, and electron holes $O_O^{\bullet}$ were numerically calculated for one-dimensional $BaZr_{1-x}Sc_xO_{3-x/2}$ (x = 0.2 and 0.5; Sc20 and Sc50, respectively) membranes on HMFC based on the Nernst–Planck diffusion model (**Figure 4-2a**). The details of the calculation methods are described in the chapter 3. The flux of each defect carrier was simulated only along the direction of thickness, and the coordinates within the electrolyte membrane were defined by the normalized thickness (L), setting the anode and cathode surfaces as 0 and 1, respectively. Electrostatic potentials were implicitly imposed on the membranes in terms of the current density, which was considered as the sum of all fluxes of the charged defects within the membrane. The cell bias was determined by subtracting the OCV from the corresponding cell voltage, representing the relative potential of the anode to cathode.

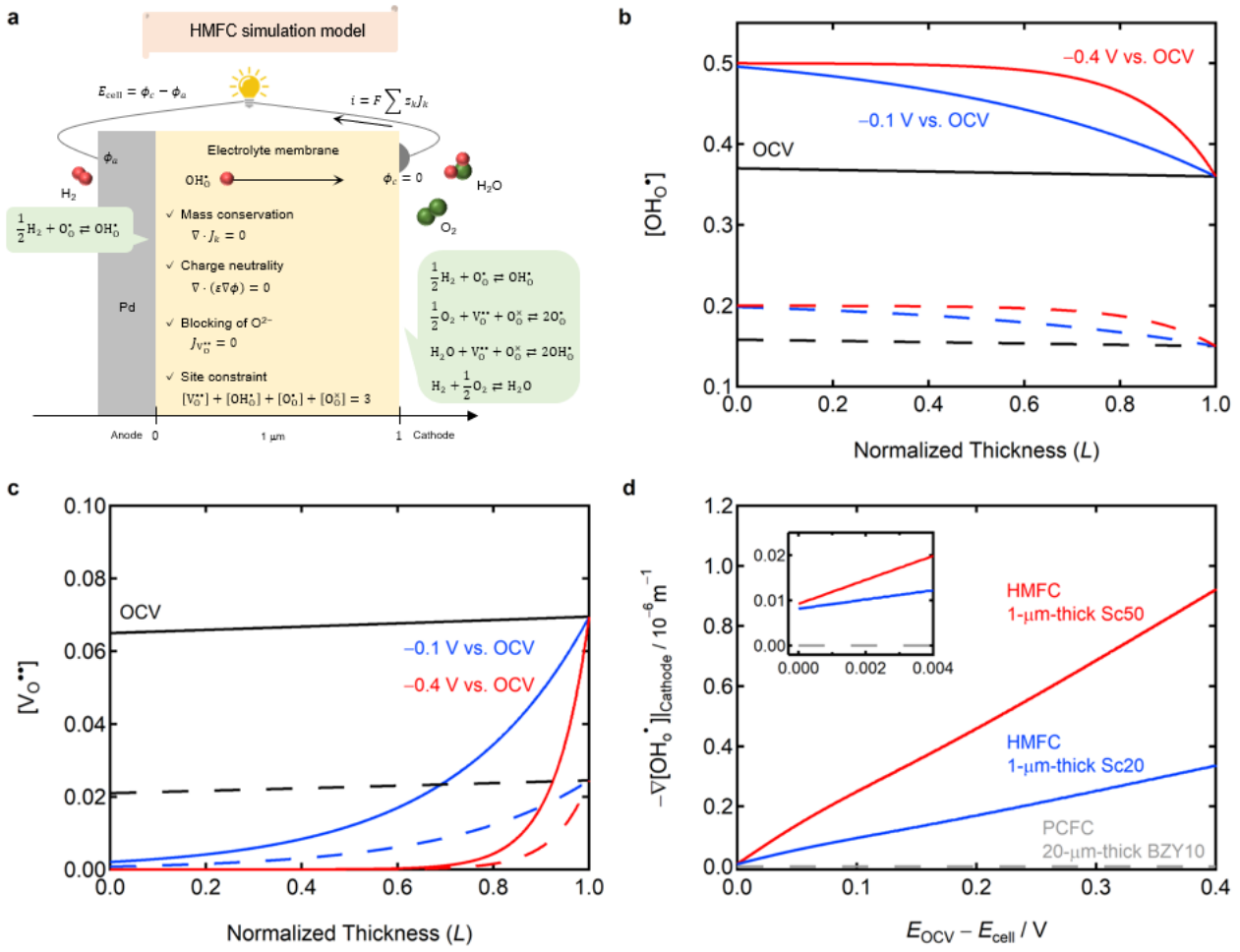

Figure 4-2. Simulated concentration profiles of mobile defects along the direction of thickness for 1-μm-thick $BaZr_{0.5}Sc_{0.5}O_{3-\delta}$ (Sc50) and $BaZr_{0.8}Sc_{0.2}O_{3-\delta}$ (Sc20) membranes on the HMFC fed with pure H_2 at the anode and wet air ($H_2O/O_2/N_2$ = 3/19.4/77.6) at the cathode at 400 °C. (a) One-dimensional model used for the simulation of HMFC. Concentration profiles of (b) proton ($OH_O^{\bullet}$) and (c) oxygen vacancies ($V_O^{\bullet\bullet}$) at 400 °C along the normalized thickness direction. Solid and dashed lines represent results of Sc50 and Sc20 base HMFCs, respectively. Black, blue and red represent a bias of 0, −0.1 and −0.4 V vs. OCV, respectively. (d) Concentration gradient of proton defects ($\nabla[OH_O^{\bullet}]$) in the vicinity of the cathode interface for HMFCs with Sc50 and Sc20. The corresponding data for a $BaZr_{0.9}Y_{0.1}O_{3-\delta}$ (BZY10) membrane on PAFC is also shown for comparison.

For the PAFC, the defect concentrations at the membrane surfaces were determined by assuming a state of equilibrium between the electrolyte membrane and the gas phase; the calculation methods are described in the chapter 3. In HMFC, the concentrations of each defect at the cathode side can be determined by the gas-membrane equilibrium, but those at the anodic surface were undefined because the surface was sealed by the dense metal anode and hence was not in equilibrium with water vapor (**Figure 4-2a**). The nominal hydrogen partial pressure (p_{H_2}) at the metal/electrolyte interface can be fixed at 1.0 atm because the Pd anode is equilibrated with pure H_2 gas. Meanwhile, the flux of $V_O^{\bullet\bullet}$ defects was set to 0 for the HMFC membrane because the diffusion of $V_O^{\bullet\bullet}$ defects was blocked. However, the $OH_O^{\bullet}$ and $O_O^{\bullet}$ defects could diffuse across the interface of the electrolyte membrane and the solid metal anode. This allowed the boundary conditions at the anodic surface to be determined.

The thermodynamic parameters of $BaZr_{1-x}Sc_xO_{3-x/2}$ are unknown; therefore, the $[V_O^{\bullet\bullet}]$ and $[OH_O^{\bullet}]$ at the cathode side (L = 1) were obtained from TG results in wet air (**Figure 4-1**), and the value of $[O_O^{\bullet}]$ was assumed to be that of $BaZr_{0.9}Y_{0.1}O_3$ (BZY10).[1] The diffusion constants of the three mobile defects also use the values of BZY10.[1] Based on these approximations, I roughly calculated the defect concentration profiles for 1-μm-thick Sc50 and Sc20 electrolytes on HMFC (**Figure 4-2**). As predicted, Sc50 can accumulate a greater amount of $OH_O^{\bullet}$ near the electrolyte/Pd interface than Sc20 owing to its relatively high $[V_O^{\bullet\bullet}]$ (**Figure 4-2b** and **4-2c**); therefore, the former undergoes more pronounced proton pumping than the latter. With the significant reduction of $[V_O^{\bullet\bullet}]$ (**Figure 4-2c**),

$[OH_O^{\bullet}]$ of the Sc50 HMFC increases by approximately 0.15, and that of Sc20 increases by approximately 0.04, in the *L* range from 0 to 0.8, on applying a cell bias of −0.4 V at 400 °C (**Figure 4-2b**).

The simulation results indicate another important effect of proton pumping: HMFC involves a much steeper gradient of proton concentration, $\nabla[OH_O^{\bullet}]$, at the cathode/electrolyte interface than PAFC because $[OH_O^{\bullet}]$ in the electrolyte bulk of HMFC is greater than that at the cathode interface owing to proton pumping, whereas that in the electrolyte bulk of PAFC tends to be flat throughout the membrane owing to the equilibration with water vapor (**Figure 4-2d**). This indicates that the HMFC membranes can develop more favorable $\nabla[OH_O^{\bullet}]$ than PAFCs for the cathode reactions at TPBs because $\nabla[OH_O^{\bullet}]$ is crucial for promoting the interfacial proton diffusion at the cathode (**Figure 4-2d**); i.e., proton pumping is effective not only for the reduction of ohmic resistance but also for lowering the cathode polarization resistance. Although the $\nabla[OH_O^{\bullet}]$ of Sc50 and Sc20 HMFCs in the vicinity of the cathode linearly increases with the cell bias, the increase of $\nabla[OH_O^{\bullet}]$ for Sc50 is greater than that for Sc20, and thus the value of the former is 2.7 times that of the latter at a cell bias of −0.4 V vs. OCV (**Figure 4-2d**). This implies that the cathode reaction resistance of the Sc50 HMFC should more efficiently decrease with the cell bias than that of Sc20 because of the pronounced proton pumping. Hereafter, the polarization behavior is analyzed for HMFCs comprising Sc50 and Sc20 electrolytes by the electrochemical method.

4.3. Experimental

4.3.1. Preparation of targets for pulsed laser deposition

BZSc20 and BZSc50 targets were prepared to perform pulsed-laser deposition. Stoichiometric amounts of starting materials: $BaCO_3$ (High Purity Chemicals, 99.95%), ZrO_2 (High Purity Chemicals, 98%), and Sc_2O_3 (High Purity Chemicals, 99.9%) were ball-milled in ethanol at 350 rpm for 12 h using planetary mills and subsequently dried at 100 °C. The obtained mixed powders were calcined at 1300 °C for 10 h at a ramp rate of 10 °C min^{-1} in ambient air. The calcined powders were then crushed and calcined again at 1500 °C for 12 h at a ramp rate of 10 °C min^{-1} in ambient air. Subsequently, the calcined powders were uniaxially pressed into green pellets (21 mm in diameter, 4–5 mm in thickness) under 20 MPa, and then pressed under a hydrostatic pressure of 100 MPa in an isostatic press. The green pellets were then sintered at 1600 °C for 8 h, covered with the single-phase powder calcined at 1500 °C.

4.3.2. Fabrication of Sc50 and Sc20 base cells

The HMFCs were fabricated by depositing BZSc films with a thickness of 1 μm on a Pd foil (0.05×12×12 mm, Tanaka Co.). The foil was polished with alumina particles (1.0 mm diameter) and cleaned by ultrasonication in acetone and pure water before deposition. BZSc films were grown on Pd foil using the pulsed-laser deposition technique with an Ulvac UPS-1000S ultravacuum chamber system. The substrate temperature was set to 700 °C. The oxygen pressure in the chamber was set to 27 Pa. During deposition, a 248 nm KrF excimer laser (Coherence Comp109) ablated the targets with

laser energy at a repetition rate of 5 Hz. The laser energy was approximately 102 mJ per a pulse. The growth rates were found to be approximately 15 nm min^{-1} for both BZSc50 and BZSc20. Finally, a $La_{0.6}Sr_{0.4}Co_{0.2}Fe_{0.8}O_{3-\delta}$ (LSCF) button electrode (7 mmϕ) was screen-printed on the surfaces of the BZSc films as a porous cathode using a commercial LSCF paste (FuelcellMaterials), with subsequent heating by a heat gun for 2 min.

4.3.3. Characterization of Sc50 and Sc20 base cells

The crystal structure and phase purity of the deposited films were determined by XRD analysis in the 2θ range between 10° and 80° at a scan rate of 1° min^{-1} using a RIGAKU diffractometer (RIGAKU Rint2000). The morphologies were examined using field-emission scanning electron microscopy (SIGMA500, ZEISS). The chemical compositions were determined by energy-dispersive X-ray spectroscopy (XFlash Detector 630, Bruker). Scanning transmission electron microscopy (TEM) was carried out using a HITACHI HD-2000 instrument to observe the cross-section of the samples. The specimens for the TEM observation were prepared by focused ion beam microfabrication (HITACHI FB-2100) using post-test samples with scrapped LSCF cathodes. Thermogravimetric analysis was carried out using an STA2500 Regulus thermogravimetric analyzer (Netzsch) on the crushed sintered pellets. The samples were heated to 1000 °C at a rate of 50 °C min^{-1} under a flow of dry 2% O_2/Ar at 100 sccm min^{-1}, and then the temperature was fixed at 1000 °C to dehydrate the samples. After thermal equilibrium was attained, the atmosphere was switched from dry 2% O_2/Ar to wet 2% O_2/Ar ($pH_2O = 0.023p_0$). The samples were then cooled to 30 °C at a rate of

2 °C min^{-1}. The proton concentrations were calculated based on the assumption that weight gain from the dehydrated samples was in accordance with the hydration reaction $H_2O + V_O^{\bullet\bullet} + O_O^{\times} \rightarrow 2OH_O^{\bullet}$. The baselines were set to plateaus after switching to a wet atmosphere.

4.3.4. Electrochemical assessment of Sc50 and Sc20 base cells

The performance of the HMFCs was evaluated by measuring the current–voltage (*I–V*) relationship and electrochemical impedance spectra at elevated temperatures. The specimen was sealed in a specially designed sample holder with a mica gasket (FuelcellMaterials). Both the cathode and anode were contacted with Pt meshes, and a thermocouple was placed in close proximity to the cell to obtain the temperature data as accurately as possible. Dry H_2 was fed to the Pd anode at a flow rate of 50 sccm min^{-1}, and wet air gas was fed to the cathode side at a rate of 50 sccm min^{-1}. The wet gas (pH_2O = 0.023 p_0) was prepared by passing the gases through water at 20 °C. The pH_2 and pO_2 of the anode and cathode gases, respectively, were adjusted using Ar balance gas. Electrochemical impedance spectra and *I–V* characteristics were obtained using a Solartron 1260/1287 system in the frequency range from 10^6 to 0.1 Hz with an AC amplitude of 30 mV under several DC bias voltages. The impedance spectra were fitted using the ZSimpWin software. The DRT results were obtained with DRTtools, MATLAB GUI toolbox, which was developed by Dr. T. Wan and Prof. F. Ciucci.[2]

4.4. Results and discussion

4.4.1. Evaluation of Sc50 and Sc20 HMFCs

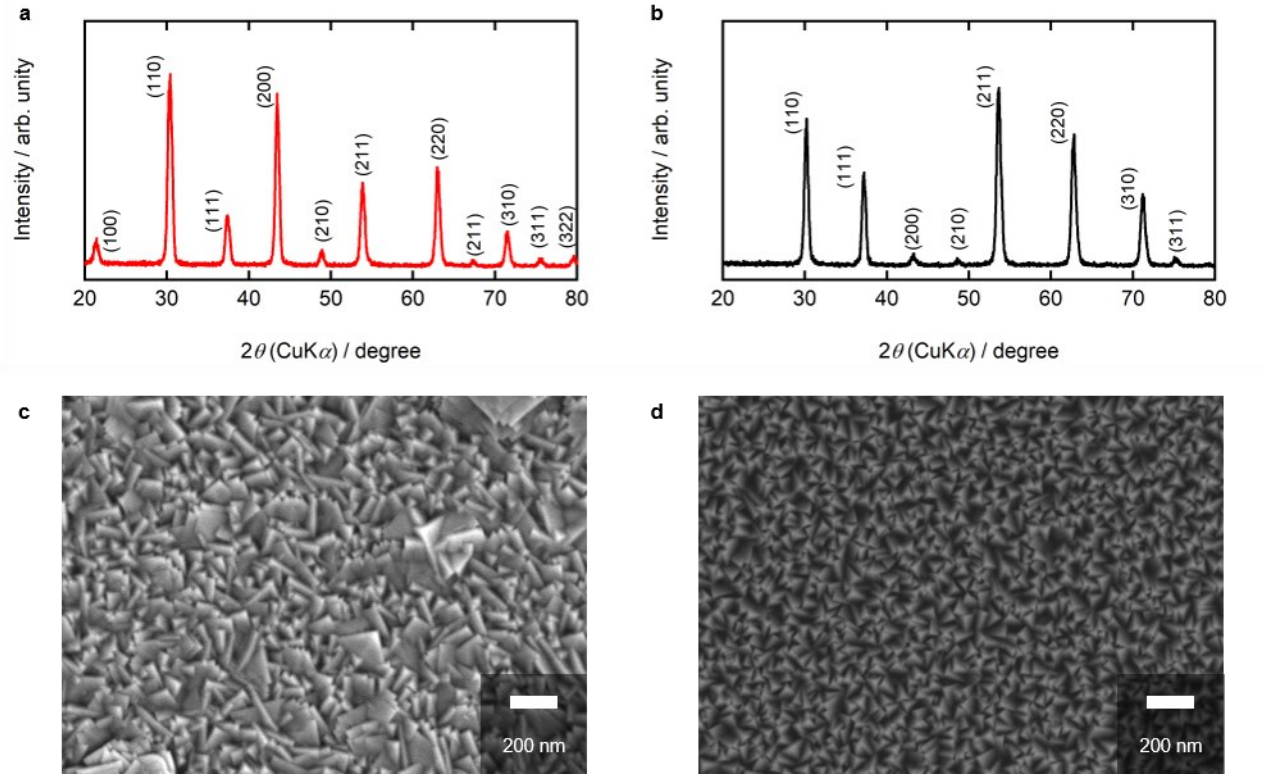

Figure 4-3. Characterizations of deposited thin films by pulsed laser deposition. XRD patterns of (a) Sc50 and (b) Sc20 electrolyte films. Surface SEM images of the (c) Sc50 and (d) Sc20 electrolyte films.

Figure 4-3a and **3b** show the X-ray diffraction (XRD) patterns of the 1-μm-thick Sc50 and Sc20 films fabricated by pulsed-laser deposition (PLD) at 700 °C. All peaks in the pattern were indexed to a cubic perovskite structure, confirming the formation of single-phase BZSc films. Both are crack-free films with densely packed rectangular columns of hundreds of nanometers in width (**Figure 4-**

3c and **3d**). Energy-dispersive X-ray spectroscopy analysis confirmed that their chemical compositions were identical to those of the target materials.

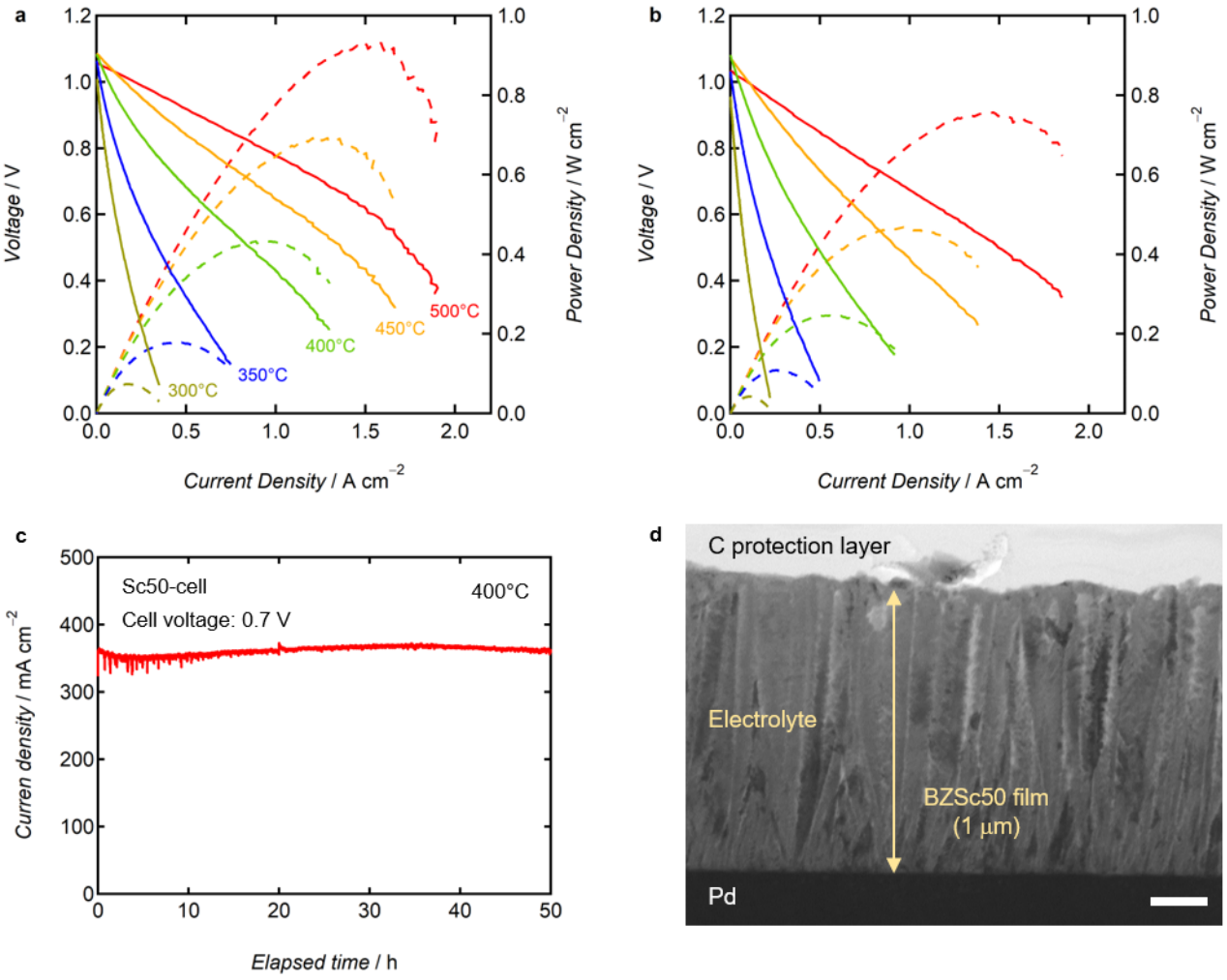

Figure 4-4. *I–V* (solid lines) and *I–P* (dashed lines) characteristics of (a) Sc50-cell and (b) Sc20-cell in the fuel cell atmosphere: Dry 100% H_2 at anode and wet air ($H_2O/O_2/Ar$ = 3/19.4/77.6) at the cathode. The voltage drops associated with equipment resistances were corrected in the *I–V* curves. (c) Long-term durability test of Sc50-cell at a constant cell voltage of 0.7 V at 400 °C. (d) Cross-sectional TEM images of the Sc50-cell obtained after the fuel cell test. The scale bars correspond to 200 nm.

Figure 4-4 shows the fuel cell performances of HMFCs based on 1-μm-thick Sc50 and Sc20 electrolyte films, denoted as Sc50- and Sc20-cell, respectively. Interestingly, the Sc50-cell yielded a 23–76% better electrochemical performance than the Sc20-cell in the entire temperature range (**Figure 4-4a** and **4-4b**). The Sc50-cell exhibited PPDs of 73, 178, 433, 692 and 931 mW cm^{-2} at 300, 350, 400, 450 and 500 °C, respectively, while maintaining an OCV of over 1.05 V. The PPD values were higher than those of HMFCs based on $BaZr_{0.1}Ce_{0.7}Y_{0.2}O_{3-\delta}$ (BZCY) electrolyte thin films, obtained in the chapter 3. The Sc20-cell with a 1-μm-thick Sc20 yielded PPDs of 42, 108, 246, 469 and 757 mW cm^{-2} at 300, 350, 400, 450 and 500 °C, respectively, while maintaining an OCV of more than 1.0 V. The Sc50-cell exhibits excellent stability under potentiostatic power generation at 0.7 V and 400 °C for 50 h (**Figure 4-4c**), yielding a stable current density of approximately 0.36 A cm^{-2} for 50 h. The BZSc50 films tightly adhered to the Pd substrate without delamination even after the 50 h test (**Figure 4-4d**). Energy-dispersive X-ray spectroscopy mapping confirmed that the electrolyte films maintained a sharp interface with the anode, indicating that no chemical interdiffusion occurred at the interface (**Figure 4-5**). These results demonstrate that the anode interface remains robust during long-term operation.

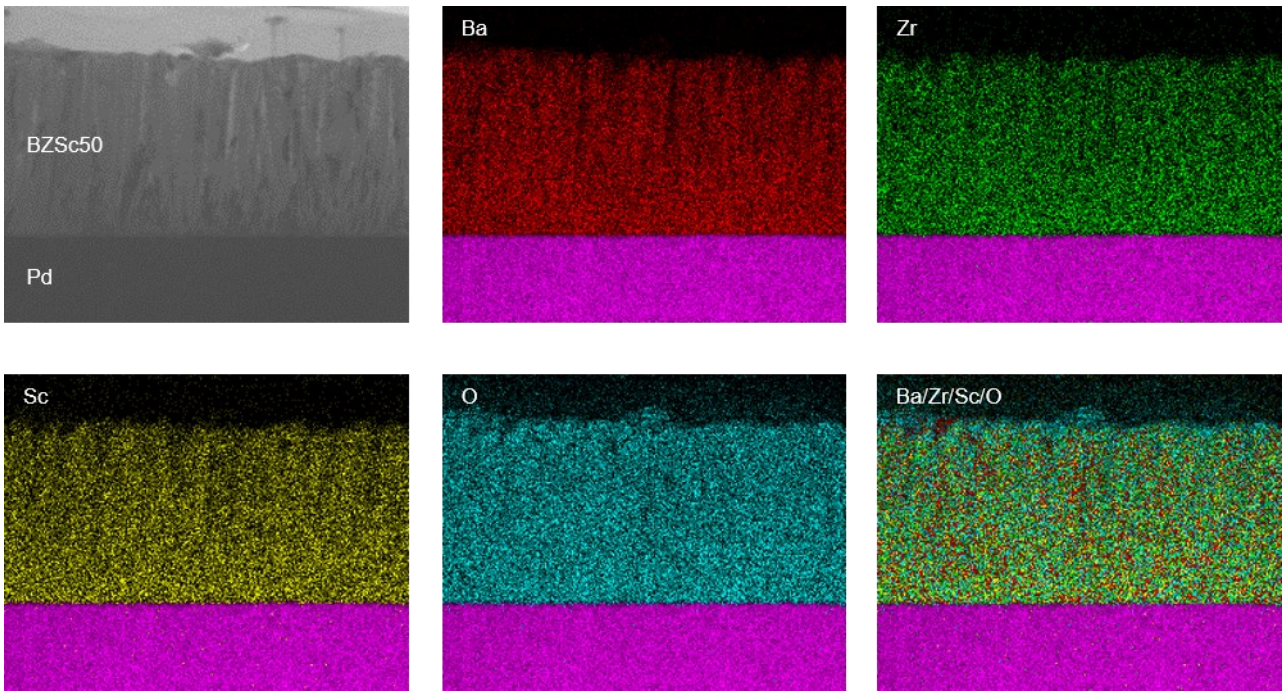

Figure 4-5. Energy-dispersive X-ray spectroscopy mapping results of cross-sectional TEM images obtained after fuel cell test. Red, green, blue, cyan and pink represent Ba, Zr, Sc, O and Pd elements, respectively.

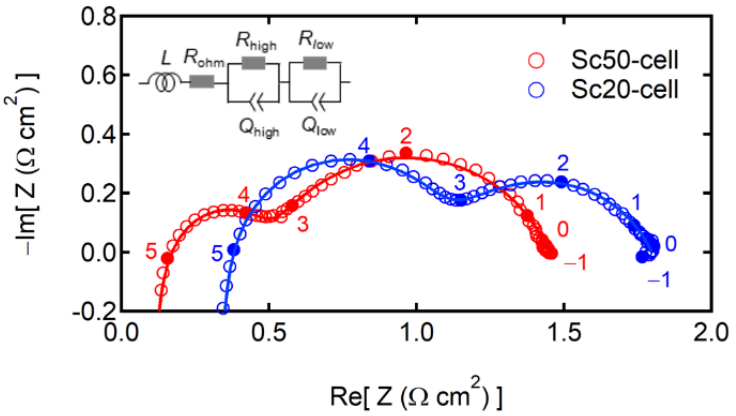

Figure 4-6. Electrochemical impedance spectra for Sc50- and Sc20-cells under OCV cell in the fuel cell atmosphere: Dry 100% H_2 at the anode and wet air ($H_2O/O_2/Ar$ = 3/19.4/77.6) at the cathode at 400 °C. The inset shows an equivalent circuit used for fitting analysis.

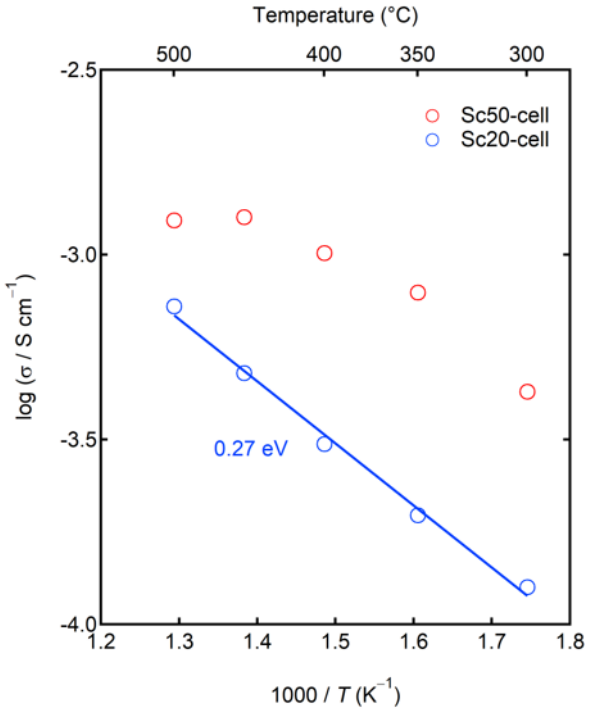

Figure 4-7. Arrhenius plots of electrolyte film conductivity of Sc50- and Sc20-cells, determined by their R_{ohm} and thickness.

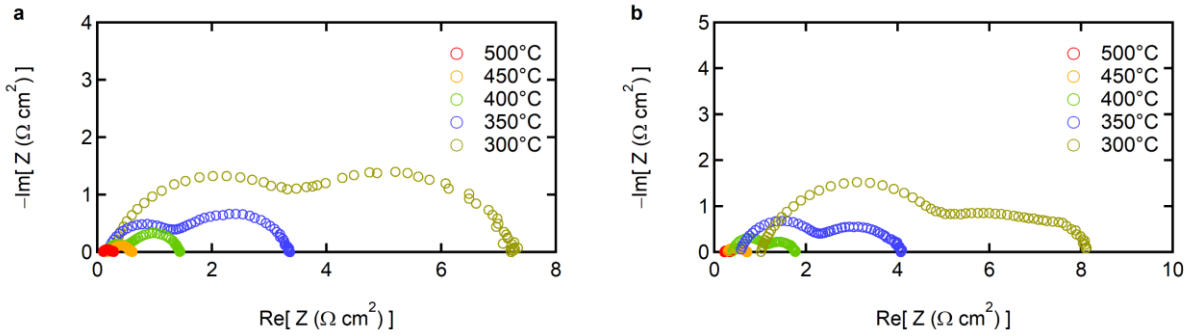

Figure 4-8. Impedance spectra for (a) Sc50-cell and (b) Sc20-cell obtained at each measured temperature under OCV in the fuel cell atmosphere: Pure H_2 at the anode and wet air ($H_2O/O_2/Ar$ = 3/19.4/77.6) at the cathode.

The polarization behavior was evaluated using electrochemical impedance spectroscopy. **Figure 4-6** shows the electrochemical impedance spectra of both Sc50- and Sc20-cells under OCV at 400 °C. In typical Nyquist plots of fuel cells, the *x*-intercept at a high frequency represents the ohmic resistance (R_{ohm}), which typically corresponds to electrolyte resistance, and the broad capacitive semicircle after the intercept corresponds to the polarization resistance (R_p). **Figure 4-7** shows the Arrhenius plot of the film conductivity (σ) determined for the R_{ohm} of Sc50- and Sc20-cells at different temperatures (**Figure 4-8**). The σ of Sc20-cell shows a linear Arrhenius relationship with the related activation energy (E_a) of 0.27 eV, which agrees with the previously reported E_a of protonic ceramic thin films.[3] The σ of Sc50-cell is apparently greater than that of the Sc20-cell at all temperatures, with a value of 10^{-3} S cm^{-1} at 400 °C, deviating downward above 400 °C, which can be attributed to the decline of protonic carriers because of dehydration at elevated temperatures.[4]

Both cells show similar electrochemical responses, including inductive behavior at very high frequencies (> 10^5 Hz) and two distinct capacitive semicircles in the high- and low-frequency regions around 10^5–10^3 Hz and 10^3–10^0 Hz, respectively, which were defined as S_{high} and S_{low}, respectively. As both cells were composed the same electrode materials, the different impedance responses may indicate the interfacial/bulk proton transfer of the electrolyte materials and/or properties of the electrolyte/electrode interfaces. Equivalent circuit analysis was conducted with the model of $LR_{ohm}(Q_{high}R_{high})(Q_{low}R_{low})$ (inset of **Figure 4-6**) to deconvolute the impedance responses, where the ($Q_{high}R_{high}$) and ($Q_{low}R_{low}$) components represent the S_{high} and S_{low} semicircles, respectively. All fitted

parameters in this chapter are listed in **Table 4-1–5**. Based on the correlation between the electrochemical capacitances of various fuel cell reaction steps,[5–9] the capacitances of S_{high} (1.3–1.5 × 10^{-5} F cm^{-2}) are related to proton transfer at the cathode/electrolyte interfaces,[5–9] and those of S_{low} (1.61.8 × 10^{-3} F cm^{-2}) to electrochemical reactions at the interfaces.

Table 4-1. Fitting data of the impedance spectra under OCV at 400°C for Sc50- and Sc20-cells.

	Sc50-cell	Sc20-cell
L / H	3.74×10^{-6}	3.64×10^{-6}
R_{ohm} / Ω cm^2	0.10	0.33
R_{high} / Ω cm^2	0.40	0.77
f_{high} / Hz	2.8×10^{4}	1.6×10^{4}
C_{high} / F cm^{-2}	1.5×10^{-5}	1.3×10^{-5}
R_{low} / Ω cm^2	0.95	0.70
f_{low} / Hz	1.0×10^{2}	1.2×10^{2}
C_{low} / F cm^{-2}	1.6×10^{-3}	1.8×10^{-3}

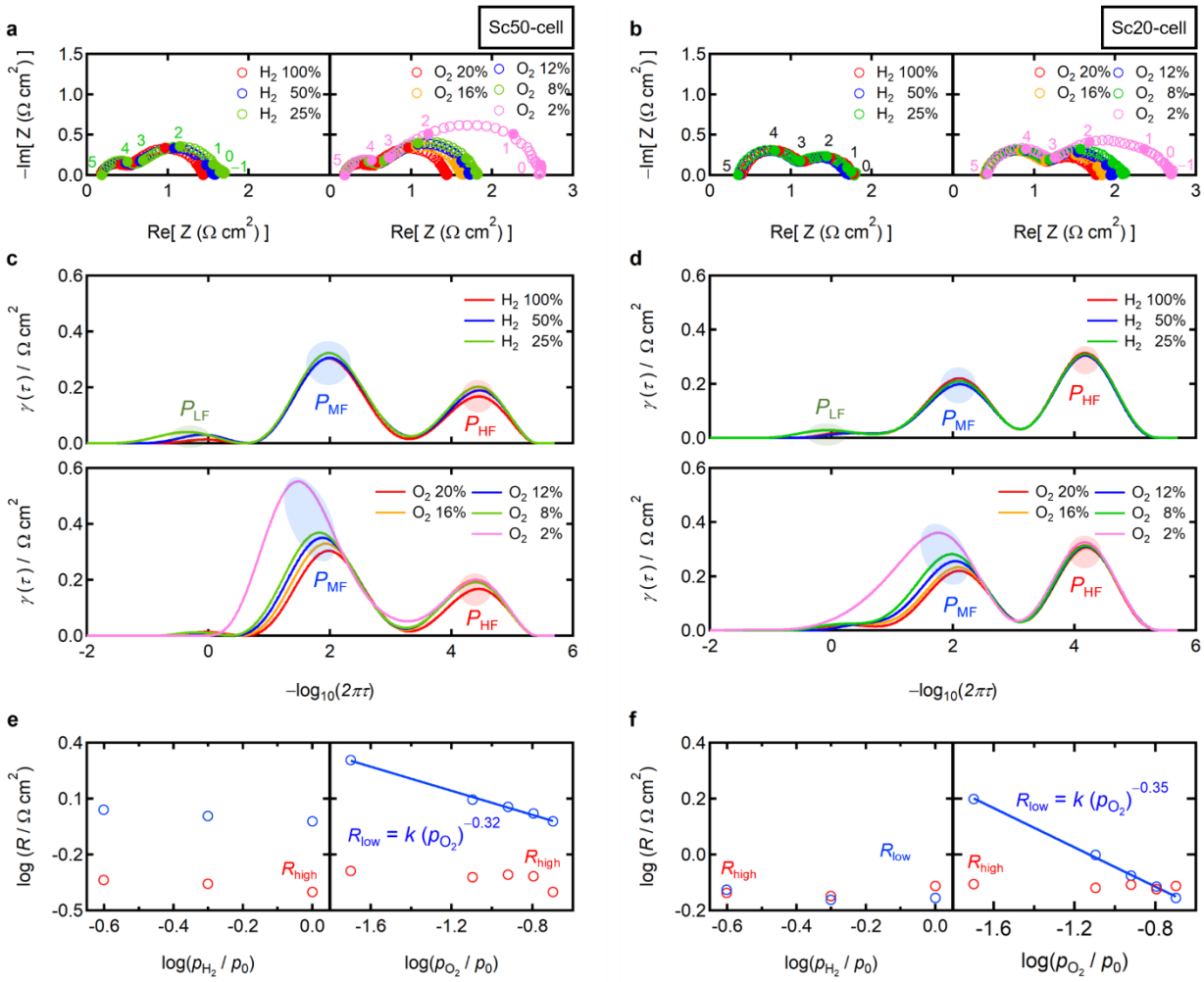

Figure 4-9. Gaseous atmosphere dependence of electrochemical impedance spectra of Sc50- and Sc20-cells at 400 °C. Nyquist plots as a function of the hydrogen partial pressure (pH_2) at the anode and oxygen partial pressure (pO_2) at the cathode under OCV for (a) Sc50- and (b) Sc20-cells. (c–d) DRT analysis for the impedance spectra of (c) Sc50- and (d) Sc20-cells. pO_2 and pH_2 dependence of polarization resistances for (e) Sc50- and (f) Sc20-cells.

Table 4-2. Fitting data of the impedance spectra in various gaseous atmosphere under OCV at 400°C for Sc50-cell.

	H_2 dependence (pO_2 = 0.20p_0)			O_2 dependence (pH_2 = 1.0p_0)				
	100%	50%	25%	20%	16%	12%	8%	2%
L / H	3.74×10^{-6}	3.69×10^{-6}	3.71×10^{-6}	3.74×10^{-6}	3.75×10^{-6}	3.64×10^{-6}	3.64×10^{-6}	3.67×10^{-6}
R_{ohm} / Ω cm^2	0.10	0.11	0.12	0.10	0.10	0.10	0.10	0.11
R_{high} / Ω cm^2	0.40	0.44	0.46	0.40	0.48	0.49	0.48	0.52
f_{high} / Hz	2.8×10^{4}	2.9×10^{4}	2.8×10^{4}	2.8×10^{4}	2.4×10^{4}	2.4×10^{4}	2.4×10^{4}	2.3×10^{4}
C_{high} / F cm^{-2}	1.5×10^{-5}	1.3×10^{-5}	1.2×10^{-5}	1.5×10^{-5}	1.4×10^{-5}	1.4×10^{-5}	1.4×10^{-5}	1.3×10^{-5}
R_{low} / Ω cm^2	0.95	1.01	1.10	0.95	1.04	1.14	1.25	2.03
f_{low} / Hz	1.0×10^{2}	1.1×10^{2}	1.0×10^{2}	1.0×10^{2}	9.1×10^{1}	8.2×10^{1}	7.3×10^{1}	3.9×10^{1}
C_{low} / F cm^{-2}	1.6×10^{-3}	1.4×10^{-3}	1.4×10^{-3}	1.6×10^{-3}	1.7×10^{-3}	1.7×10^{-3}	1.7×10^{-3}	2.0×10^{-3}

Table 4-3. Fitting data of the impedance spectra in various gaseous atmosphere under OCV at 400°C for Sc20-cell.

	H_2 dependence (pO_2 = 0.20p_0)			O_2 dependence (pH_2 = 1.0p_0)				
	100%	50%	25%	20%	16%	12%	8%	2%
L / H	3.64×10^{-6}	3.57×10^{-6}	3.68×10^{-6}	3.64×10^{-6}	3.57×10^{-6}	3.55×10^{-6}	3.56×10^{-6}	3.56×10^{-6}
R_{ohm} / Ω cm^2	0.33	0.32	0.30	0.33	0.33	0.35	0.35	0.36
R_{high} / Ω cm^2	0.77	0.71	0.73	0.77	0.75	0.78	0.76	0.78
f_{high} / Hz	1.6×10^{4}	1.6×10^{4}	1.6×10^{4}	1.6×10^{4}	1.6×10^{4}	1.6×10^{4}	1.6×10^{4}	1.6×10^{4}
C_{high} / F cm^{-2}	1.3×10^{-5}	1.4×10^{-5}	1.3×10^{-5}	1.3×10^{-5}	1.3×10^{-5}	1.3×10^{-5}	1.3×10^{-5}	1.3×10^{-5}
R_{low} / Ω cm^2	0.70	0.69	0.75	0.70	0.77	0.84	1.0	1.58
f_{low} / Hz	1.2×10^{2}	1.3×10^{2}	1.3×10^{2}	1.2×10^{2}	1.2×10^{2}	1.0×10^{2}	8.8×10^{1}	4.6×10^{1}
C_{low} / F cm^{-2}	1.8×10^{-3}	1.7×10^{-3}	1.6×10^{-3}	1.8×10^{-3}	1.8×10^{-3}	1.9×10^{-3}	1.8×10^{-3}	2.2×10^{-3}

To deconvolute the spectra more precisely, the impedance responses of the Sc50- and Sc20-cells were evaluated in terms of the hydrogen and oxygen partial pressures (pH_2 and pO_2) at the anode and cathode, respectively, as shown in **Figure 4-9a** and **4-9b**. **Figure 4-9c** and **4-9d** display the corresponding distribution of relaxation times (DRTs), which deconvolutes the total polarization into

its individual processes. In DRT analysis, the integral area of the peak represents the specific resistance of the process. The DRT results show that both cells involve three electrochemical processes, which appear at approximately 10^4, 10^2 and 10^0 Hz, defined as P_{HF}, P_{MF} and P_{LF}, respectively. This indicates that S_{low} includes two electrochemical processes related to P_{MF} and P_{LF} as the P_{HF} is identical to the R_{high} of S_{high}. P_{LF} is not sensitive to pO_2 at the cathode, but apparently increases with decreasing pH_2 at the anode. A previous study clarified that HMFCs exhibit impedance semicircles in the frequency range from 10 to 0.1 Hz owing to the limits of H diffusion in Pd metal;[10] thus, the P_{LF} is assigned to the delay of the anode reaction caused by H bulk diffusion. P_{LF} is negligibly small at relatively high pH_2, so the P_{MF} mainly contributes to the R_{low} in fuel cell conditions. P_{MF} significantly decreased with decreasing pO_2 at the cathode, while it did not respond to pH_2 at the anode (**Figure 4-9c** and **4-9d**), indicating that S_{low} represents the cathode reactions at the TPBs. Based on these results, S_{high} and S_{low} feature elementary steps in the cathode reaction, and the Nyquist plot of HMFCs can thus be analyzed by the equivalent circuit model depicted in **Figure 4-6**.

Figure 4-9e and **4-9f** show the pH_2- and pO_2-dependences of R_{high} and R_{low} for Sc50- and Sc20-cells, revealing that the R_{low} of Sc50- and Sc20-cells is proportional to pO_2^{-m} with m = 0.32 and 0.35, respectively (**Figure 4-9e** and **4-9f**). Recently, an elementary step reaction order analysis was conducted for the cathode reaction on protonic ceramic fuel cells with mixed ionic and electronic conducting (MIEC) cathodes,[11–13] which allows the determination of the rate-controlling steps of the reaction from the pO_2^{-m} dependence of the related resistances. In general, the cathode reaction of

protonic ceramic fuel cells with MIEC cathodes proceeds via the elementary steps: (1) adsorption and dissociation of O_2 molecules, (2) first electron transfer to the oxygen adatoms with (3) subsequent diffusion to the TPB, (4) second electron transfer to the absorbed O^-, (5) interfacial transfer of H^+ from the electrolyte to the TPB, (6) association of the adsorbed O^- and H^+ and (7) OH^- and H^+ at the TPB and (8) desorption of the H_2O (**Figure 4-10a**). The *m* and *n* indices for pO_2 and pH_2O are summarized for each elementary step in **Figure 4-10b**. The reaction orders of R_{low}, *m*, are 0.32–0.35, which are very close to the *m* (0.375) of step 2, but extremely different from the values of other steps. Consequently, the first charge transfer to the oxygen adatoms is speculated to be the rate-controlling step, and thus contributes to R_{low}. R_{high} is not sensitive to pO_2 at the cathode, i.e., $m = 0$ (**Figure 4-9e** and **4-9f**), which agrees with the value of the interfacial proton transfer step (**Figure 4-10b**), confirming that R_{high} is attributable to the proton transfer resistance.

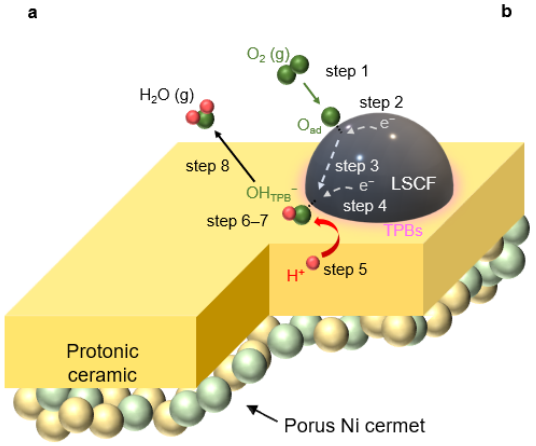

	Elementary reaction	Reaction Kinetic, r_i	$\frac{\partial r_i}{\partial P_{O_2}}$
Step 1	$O_2\,(g) \rightarrow 2O_{ad}$	$k_1 P_{O_2} - k_1' a_{O_{ad}}{}^2$	1
Step 2	$O_{ad} + e^- \rightarrow O^-_{ad}$	$k_2 a_{O_{ad}}{}^2 e^{-\frac{FE}{2RT}} - k_2' a_{O^-_{ad}} e^{\frac{FE}{2RT}}$	3/8
Step 3	$O^-_{ad} \rightarrow O^-_{TPB}$	$k_3 a_{O^-_{ad}} - k_3' a_{O^-_{TPB}}$	1/4
Step 4	$O^-_{TPB} + e^- \rightarrow O^{2-}_{TPB}$	$k_4 a_{O^-_{ad}} e^{-\frac{FE}{2RT}} - k_4' a_{O^{2-}_{ad}} e^{\frac{FE}{2RT}}$	1/8
Step 5	$H^+_{ele} \rightarrow H^+_{TPB}$	$k_5 a_{H^+_{ele}} - k_5' a_{H^+_{TPB}}$	0
Step 6	$H^+_{TPB} + O^{2-}_{TPB} \rightarrow OH^-_{TPB}$	$k_6 a_{H^+_{TPB}} a_{O^{2-}_{TPB}} - k_6' a_{OH^-_{TPB}}$	0
Step 7	$H^+_{TPB} + OH^-_{TPB} \rightarrow H_2O_{TPB}$	$k_7 a_{H^+_{ele}} a_{OH^-_{TPB}} - k_7' a_{H_2O_{TPB}}$	0
Step 8	$H_2O_{TPB} \rightarrow H_2O\,(g)$	$k_8 a_{H_2O_{TPB}} - k_8' P_{H_2O}$	0

Figure 4-10. (a) Reaction models for cathode reaction with mixed ionic and electronic conducting $La_{0.6}Sr_{0.4}Co_{0.2}Fe_{0.8}O_{3-\delta}$ (LSCF) cathode based on proton-conducting ceramics and (b) each reaction step with respect to pO_2.

4.4.2. Systematic demonstration of proton pumping in HMFCs

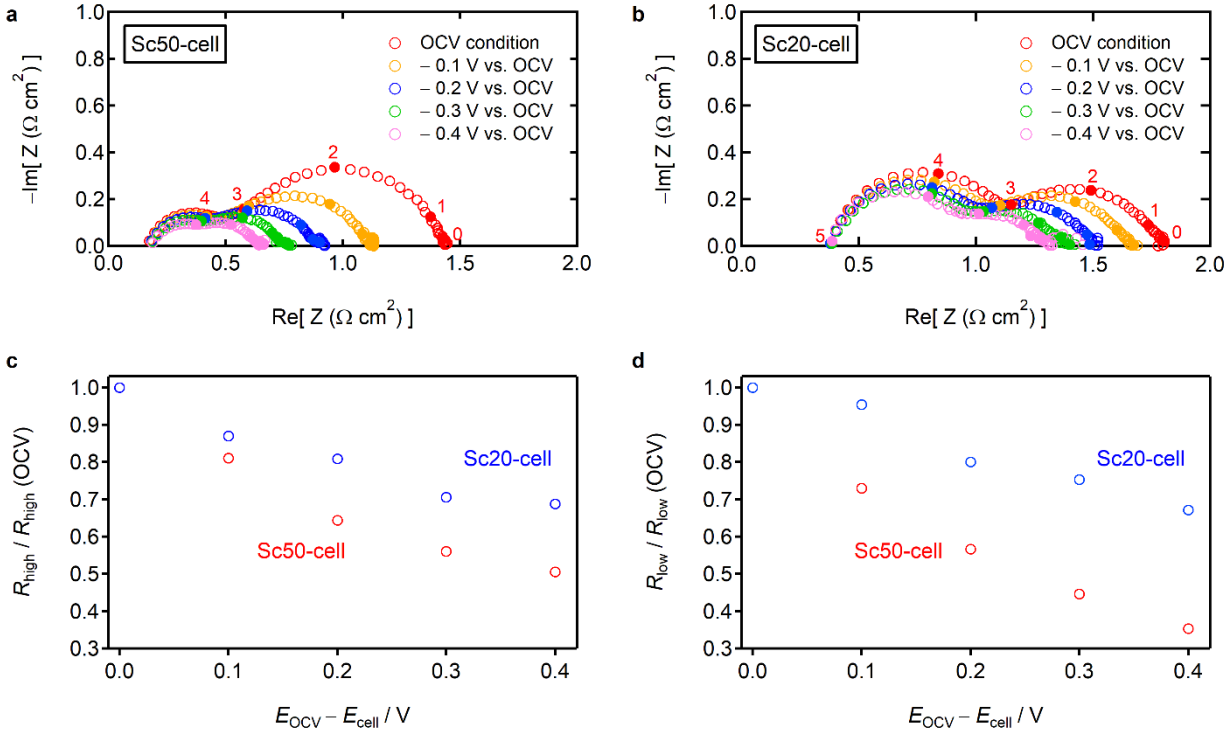

Figure 4-11. Bias-dependence of electrochemical impedance spectra. Nyquist impedance plots of the (a) Sc50-cell and (b) Sc20-cell at 400 °C under various cell bias values. (c) R_{high} and (d) R_{low} at different cell bias values, normalized by the values at OCV.

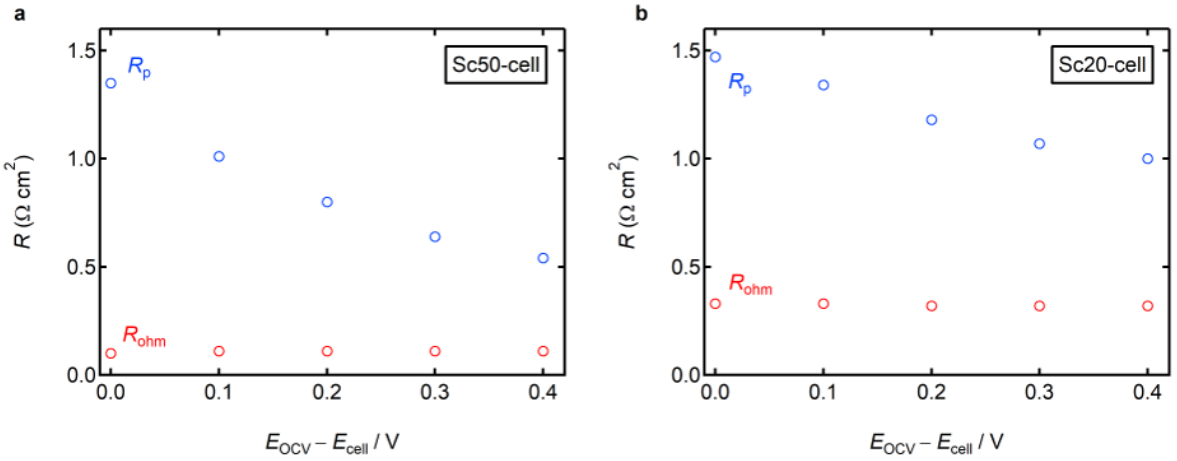

Figure 4-12. R_{ohm} and R_p at different bias conditions for (a) Sc50-cell and (b) Sc20-cell at 400 °C.

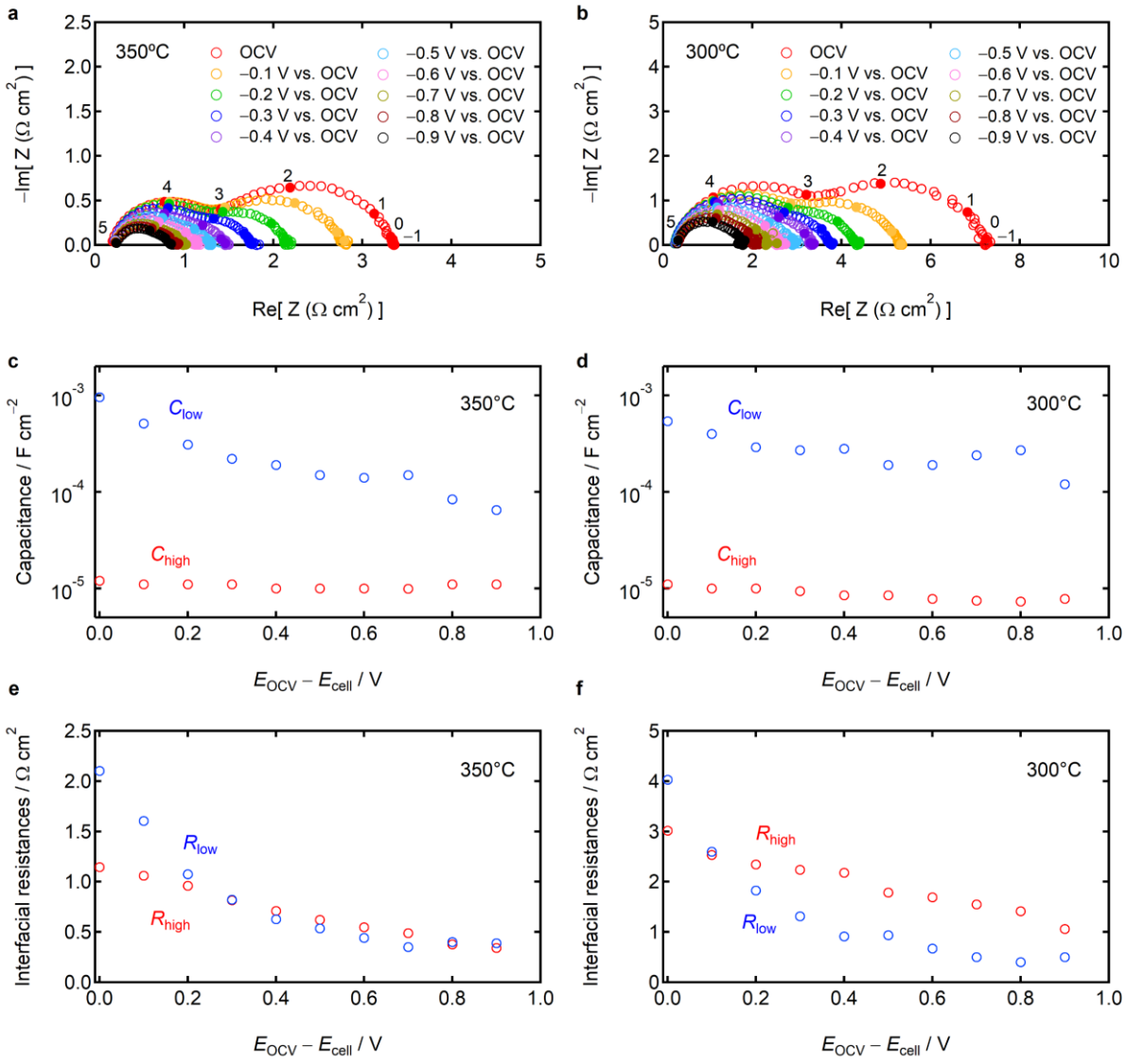

Figure 4-13. Dependence of electrochemical impedance spectra of Sc50-cell on cathodic bias at (a) 350 °C and (b) 300 °C in the fuel cell atmosphere: Pure H_2 at anode and wet air ($H_2O/O_2/N_2$ = 3/19.4/77.6). The impedance spectra were fitted using the equivalent circuit $LR_{ohm}(R_{high}Q_{high})(R_{low}Q_{low})$. The corresponding capacitances at (c) 350 °C and (d) 300 °C. The corresponding interfacial resistances at (e) 350 °C and (f) 300 °C.

As described in the chapter 3, proton pumping is characterized by the bias dependence of R_{ohm} and interfacial proton transfer resistance, i.e., R_{high}. Impedance spectra were collected under various cell biases to verify the proton pumping of Sc20- and Sc50-cells at 400 °C. The cell bias is calculated by subtracting the OCV from the cell voltage, representing the relative potential of the cathode and anode, respectively. R_{ohm} for both cells remained unchanged with the cell bias, which was attributed to the small voltage loss of bulk transport owing to the relatively low R_{ohm} compared with R_p (**Figure 4-11a** and **Figure 4-12**). Meanwhile, R_{high} monotonically decreased with increasing negative cell bias in Sc50- and Sc20-cells at temperatures below 400 °C (**Figures 4-11a** and **Figure 4-13e** and **4-13f**), revealing that the proton concentration gradient that drives the interfacial transfer increases with the cell bias. This agrees with the numerical simulation results that predict that $\nabla[OH_O^{\bullet}]$ linearly increases with cell bias (**Figure 4-2d**). Normally, the ionic conductivity is independent of the applied field as per the linear response theory because the electrical potential difference between two adjacent ion sites, $E_{pot} = q \cdot l \cdot E_{field}$ (where l is the lattice constant), is weak compared with the thermal energy $k_B T$,[14,15] and thus the overpotential for ionic transfer does not affect the mobility itself. The cathode reaction resistances of conventional PAFCs, rate-limited by interfacial proton transfer, have been reported to be bias-independent.[7] This strongly suggests that $\nabla[OH_O^{\bullet}]$ near the cathode is not modified by bias in conventional PAFCs, which agrees with the simulation results for $\nabla[OH_O^{\bullet}]$ of PAFC with 20-μm-thick BZY10 (**Figure 4-2d**). Accordingly, the bias-induced reduction of R_{high} (**Figure 4-11c**) proves the increase in interfacial $\nabla[OH_O^{\bullet}]$ because of applied bias, demonstrating that

proton pumping takes place in HMFCs. The R_{high} of the Sc50-cell decreased by 50% while that of Sc20-cell decreases only by 31% at a cell bias of −0.4 V at 400 °C (**Figure 4-11c**), which is in agreement with the simulation results that display a larger increment of $\nabla[OH_O^{\bullet}]$ for Sc50-cell than that for Sc20-cell because of proton pumping enhancement by relatively high $[V_O^{\bullet\bullet}]$ (**Figures 4-2c** and **4-2d**). These results systematically demonstrate the robustness of the proton-pumping model.

R_{low} exponentially decreases with increasing negative cell bias in both Sc50- and Sc20-cells (**Figure 4-11b** and **Figure 4-13e** and **4-13f**), which is consistent with the features of the charge transfer step because the electrochemical charge transfer kinetics includes exponential terms ($\propto \exp(-E_a/kT)$) based on the Butler–Volmer equation; the applied bias can directly decrease the E_a.[11,16] In addition to R_{high}, the reduction of R_{low} in Sc50 is greater than that in Sc20: R_{low} of Sc20-cell decreases by 33% relative to R_{low} at OCV (R_{low}(OCV)) after applying a cell bias of −0.4 V. However, the R_{low} of Sc50-cell decreases by 65% even when using the same LSCF cathode. This implies that fast interfacial proton transfer facilitates charge-transfer reactions near TPBs.

Table 4-4. Fitting data of the impedance spectra under various negative bias conditions at 400°C for Sc50-cell.

	Sc50-cell (standard fuel cell atmosphere)				
Bias / vs. OCV	0 V	−0.1 V	−0.2 V	−0.3 V	−0.4 V
L / H	3.74×10^{-6}	3.67×10^{-6}	3.68×10^{-6}	3.68×10^{-6}	3.68×10^{-6}
R_{ohm} / Ω cm^2	0.10	0.11	0.11	0.11	0.11
R_{high} / Ω cm^2	0.40	0.32	0.26	0.22	0.20
f_{high} / Hz	2.8×10^{4}	3.5×10^{4}	4.2×10^{4}	4.7×10^{4}	5.1×10^{4}
C_{high} / F cm^{-2}	1.5×10^{-5}	1.4×10^{-5}	1.5×10^{-5}	1.5×10^{-5}	1.6×10^{-5}
R_{low} / Ω cm^2	0.95	0.69	0.54	0.42	0.34
f_{low} / Hz	1.0×10^{2}	2.8×10^{2}	7.1×10^{2}	1.4×10^{2}	2.0×10^{3}
C_{low} / F cm^{-2}	1.6×10^{-3}	8.2×10^{-4}	4.1×10^{-4}	2.8×10^{-4}	2.4×10^{-4}

Table 4-5. Fitting data of the impedance spectra under various negative bias conditions at 400°C for Sc20-cell.

	Sc20-cell (standard fuel cell atmosphere)				
Bias / vs. OCV	0 V	−0.1 V	−0.2 V	−0.3 V	−0.4 V
L / H	3.64×10^{-6}	3.61×10^{-6}	3.61×10^{-6}	3.64×10^{-6}	3.62×10^{-6}
R_{ohm} / Ω cm^2	0.33	0.33	0.32	0.32	0.32
R_{high} / Ω cm^2	0.77	0.67	0.62	0.54	0.53
f_{high} / Hz	1.6×10^{4}	1.8×10^{4}	2.1×10^{4}	2.4×10^{4}	2.6×10^{4}
C_{high} / F cm^{-2}	1.3×10^{-5}	1.3×10^{-5}	1.2×10^{-5}	1.2×10^{-5}	1.2×10^{-5}
R_{low} / Ω cm^2	0.70	0.67	0.56	0.53	0.47
f_{low} / Hz	1.2×10^{2}	1.9×10^{2}	2.7×10^{2}	3.9×10^{2}	5.0×10^{2}
C_{low} / F cm^{-2}	1.8×10^{-3}	1.3×10^{-3}	1.1×10^{-3}	7.8×10^{-4}	6.8×10^{-4}

4.4.3. Mechanism of fast cathode reactions in HMFCs

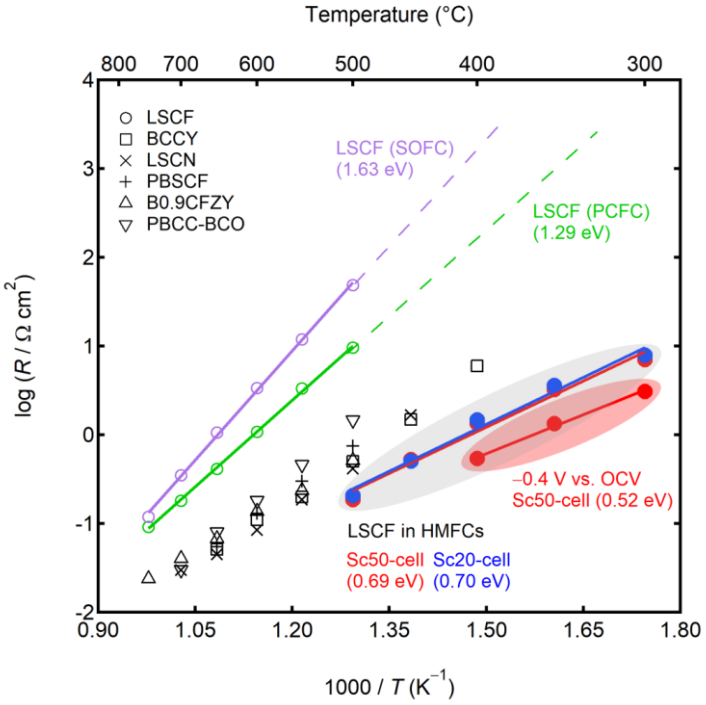

Figure 4-14. Arrhenius plots of the R_p (solid plot in grey-shade region) in this work and comparison with the reported R_p of $La_{0.6}Sr_{0.4}Co_{0.2}Fe_{0.8}O_{3-\delta}$ (LSCF; ○) for PAFC[17] and SOFC[18], and recently reported triple-conducting ($H^+/O^{2-}/e^-$) cathode materials (black hollow plot): $BaCo_{0.7}(Ce_{0.8}Y_{0.2})_{0.3}O_{3-\delta}$ (□; BCCY[19]), $La_{0.8}Sr_{0.2}Co_{0.7}Ni_{0.3}O_{3-\delta}$ (×; LSCN[20]), $PrBa_{0.5}Sr_{0.5}Co_{1.5}Fe_{0.5}O_{5+\delta}$ (┼; PBSCF[21]), $Ba_{0.9}Co_{0.4}Fe_{0.4}Zr_{0.1}Y_{0.1}O_{3-\delta}$ (△; B0.9CFZY[22]), and $PrBa_{0.8}Ca_{0.2}Co_2O_{5+d}$-$BaCoO_{3-\delta}$ composite (▽; PBCC-BCO[23]). The plots in the red-shaded region represent the R_p of Sc50-cell at −0.4 V vs. OCV.

As shown in **Figure 4-14**, the current HMFCs were found to exhibit a lower cathode reaction resistance R_p and related E_a than the conventional thin film PAFCs and SOFCs with the same LSCF

cathode materials. The R_p of the HMFC is calculated by the sum of R_{high} and R_{low}. LSCF shows poor cathode performance compared with advanced multifunctional cathodes owing to the sluggish surface kinetics.[21,24,25] The PAFC with LSCF cathode exhibits an R_p of 9.64 Ω cm^2 at 500 °C with an E_a of 1.29 eV[17] and the SOFC exhibits an R_p of 48.7 Ω cm^2 at 500 °C with an E_a of 1.63 eV.[18] The R_p of these PAFCs and SOFCs significantly increased with decreasing temperature and were extrapolated to 177 and 1977 Ω cm^2 at 400 °C (**Figure 4-14**). However, HMFCs using the same LSCF cathode exhibit much lower R_p and E_a values. The R_p of Sc50- and Sc20-cells is 1.35 and 1.47 Ω cm^2, respectively, even at 400 °C, which is 2–3 orders of magnitude lower than those of the PAFC and SOFC. The related E_a is approximately 0.7 eV for both Sc50- and Sc20-cells, and it significantly decreases to 0.52 eV after applying a cell bias of −0.4 V (**Figure 4-14**). Although it should be noted that R_p may include non-negligible anodic resistances at such low temperatures in the case of PAFCs, cathodic resistances should be much larger than anodic ones because of sluggish kinetics of cathode reactions. The E_a and R_p in HMFCs are much smaller than those in PAFCs with electrolyte thin film (1–2.5 μm in thickness) and similar cathode material, $La_{0.6}Sr_{0.4}CoO_{3-\delta}$.[3,26] Further, our data are compared with other PAFC reports with various electrolyte/cathode interfaces and it is found that R_p of HMFCs are smaller than those of PAFCs regardless of electrolyte/cathode interfaces, as shown in **Table 4-6**. These results unequivocally demonstrate that the cathode reaction on HMFCs takes different reaction pathways or energy landscape from those of PAFCs and SOFCs, thereby resulting in different rate-controlling steps, despite using the similar LSCF cathode.

Table 4-6. Comparison of performances of HMFC in this study with those of PAFC in other reports.

Cell type	Anode	Electrolyte	Electrode	Temperature [°C]	R_p [Ω cm^2]	Cell bias	E_a of R_p [eV]	Reference
HMFC	Pd	Sc50 (1 μm)	LSCF	400	1.35	OCV	0.69	This work
					0.54	−0.4	0.52	
		Sc20 (1 μm)			1.47	OCV	0.70	
					1.00	−0.4	0.50	
PAFC	Ni-BZY15 (40/60; v/v)	BZY15 (2.5 μm)	LSC	450	4.55	OCV	1.21	26
PAFC	NiO-YSZ	BZCY3 (1 μm)	LSC	550	0.55	OCV	1.18	3
PAFC	NiO-BZCYYb (60/40; w/w)	BZCYYb (4 μm)	BSCF-BZCYYb	600	0.275	OCV	0.85	27
PAFC	NiO-BZCYYb (60/40; w/w)	BZCYYb (~ 25μm)	BCZY63-BCFZY	400	0.94	OCV	0.69	28
PAFC	NiO-BZCY3 (55/45; w/w)	BZCY3 (5 μm)	BSCF	500	0.64	OCV	1.14	29
PAFC	NiO-BZCYYb (70/30; w/w)	BZCYYb (16.1 μm)	BCCY	550	0.25	OCV	0.84	19
PAFC	NiO-BZCYYb (65/35; w/w)	BZCYYb (14.7 μm)	NBSCF	600	0.28	OCV	0.93	30
PAFC	Ni-BZY15 (40/60; v/v)	BZCY4 (5 μm)	PNO	550	3.86	OCV	1.07	31
PAFC	NiO-BZCY1 (60/40; w/w)	BZCY1 (40 μm)	B0.9CFZY	500	0.52	OCV	0.84	22
PAFC	NiO-BZCYYb4 (65/35; w/w)	BZCYYb4 (~ 15 μm)	PBSCF	500	0.75	OCV	1.07	21
PAFC	NiO-BZCYYb	BZCYYb (~ 10 μm)	PBCC-BCO	500	1.45	OCV	1.23	23
PAFC	NiO-BZCYYb	BZCYYb (~ 20 μm)	SFMZ	650	0.34	OCV	0.96	32
PAFC	NiO-BZCY4 (60/40; w/w)	BZCY4 (24 μm)	LSCN	450	1.68	OCV	0.97	20
PAFC	NiO-BZCY4 (60/40; w/w)	BZCY4 (19 μm)	LSMN	500	3.44	OCV	1.13	33
			LSCF	500	4.56	OCV	1.54	33
PAFC	NiO-BZCY1 (65/35; w/w)	BZCY1 (55 μm)	LSCF	500	9.64	OCV	1.29	17
PAFC	NiO-BZCY4 (70/30; w/w)	BZCY4 (20 μm)	BZCY4-BSCFT	550	3.27	OCV	1.04	34
PAFC	NiO-BZCYYb (65/35; w/w)	BZCYYb (15 μm)	BPI	600	0.49	OCV	1.41	35
PAFC	NiO-BZCYYb (60/40; w/w)	BZCYYb (15 μm)	BCFNb	600	0.76	OCV	1.40	36
PAFC	NiO-BZCYYb (60/40; w/w)	BZCYYb (25 μm)	SFSb	550	2.14	OCV	1.23	37

PAFC	NiO-BZCYYb (65/35; w/w)	BZCYYb (~ 60 μm)	BCFZ	500	2.10	OCV	0.79	38
PAFC	NiO-BZCY181 (60/40; w/w)	BZCY181 (9 μm)	BZCY181-SSC	600	0.421	OCV	1.06	39
PAFC	NiO-BZCYYb (60/40; w/w)	BZCYYb (15 μm)	SSFCu-SDC	500	2.62	OCV	0.92	40
			SSC-SDC	500	3.74	OCV	1.19	40
			BSF-SDC	500	3.66	OCV	1.23	40
PAFC	NiO-BZCYYb (60/40; w/w)	BZCYYb (15 μm)	PBF	600	0.86	OCV	1.15	41
PAFC	NiO-BZCY1 (60/40; w/w)	BZCY1 (10 μm)	PBC	600	0.92	OCV	1.33	42

※ Abbreviation: $BaZr_{0.5}Sc_{0.5}O_{3-\delta}$ (Sc50), $BaZr_{0.8}Sc_{0.2}O_{3-\delta}$ (Sc20), $La_{0.6}Sr_{0.4}Co_{0.2}Fe_{0.8}O_{3-\delta}$ (LSCF), $BaZr_{0.85}Y_{0.15}O_{3-\delta}$ (BZY15), $La_{0.6}Sr_{0.4}CoO_{3-\delta}$ (LSC), $Zr_{0.92}Y_{0.08}O_{1.96}$ (YSZ), $BaZr_{0.3}Ce_{0.55}Y_{0.15}O_{3-\delta}$ (BZCY3), $BaZr_{0.1}Ce_{0.7}Y_{0.1}Yb_{0.1}O_{3-\delta}$ (BZCYYb), $Ba_{0.5}Sr_{0.5}Co_{0.8}Fe_{0.2}O_{3-\delta}$ (BSCF), $BaCe_{0.6}Zr_{0.3}Y_{0.1}O_{3-\delta}$ (BCZY63), $BaCo_{0.4}Fe_{0.4}Zr_{0.1}Y_{0.1}O_{3-\delta}$ (BCFZY), $BaCo_{0.7}(Ce_{0.8}Y_{0.2})_{0.3}O_{3-\delta}$ (BCCY), $NdBa_{0.5}Sr_{0.5}Co_{1.5}Fe_{0.5}O_{5+\delta}$ (NBSCF), $Pr_2NiO_{4+\delta}$ (PNO), $BaZr_{0.4}Ce_{0.4}Y_{0.2}O_{3-\delta}$ (BZCY4), $BaZr_{0.1}Ce_{0.7}Y_{0.2}O_{3-\delta}$ (BZCY1), $Ba_{0.9}Co_{0.4}Fe_{0.4}Zr_{0.1}Y_{0.1}O_{3-\delta}$ (B0.9CFZY), $BaZr_{0.4}Ce_{0.4}Y_{0.1}Yb_{0.1}O_{3-\delta}$ (BZCYYb4), $PrBa_{0.5}Sr_{0.5}Co_{1.5}Fe_{0.5}O_{5+\delta}$ (PBSCF), $PrBa_{0.8}Ca_{0.2}Co_2O_{5+\delta}$ (PBCC), $BaCoO_{3-\delta}$ (BCO), $Sr_2Fe_{1.5}Mo_{0.4}Zr_{0.1}O_{6-\delta}$ (SFMZ), $La_{0.8}Sr_{0.2}Co_{0.7}Ni_{0.3}O_{3-\delta}$ (LSCN), $La_{0.7}Sr_{0.3}Mn_{0.7}Ni_{0.3}O_{3-\delta}$ (LSMN), $Ba_{0.5}Sr_{0.5}(Co_{0.8}Fe_{0.2})_{0.9}Ti_{0.1}O_{3-\delta}$ (BSCFT), $BaPr_{0.8}In_{0.2}O_{3-\delta}$ (BPI), $Ba_{0.9}Co_{0.7}Fe_{0.2}Nb_{0.1}O_{3-\delta}$ (BCFNb), $SrFe_{0.9}Sb_{0.1}O_{3-\delta}$ (SFSb), $BaCo_{0.4}Fe_{0.4}Zr_{0.2}O_{3-\delta}$ (BCFZ), $BaZr_{0.1}Ce_{0.8}Y_{0.1}O_{3-\delta}$ (BZCY181), $Sm_{0.5}Sr_{0.5}CoO_{3-\delta}$ (SSC), $Sm_{0.5}Sr_{0.5}Fe_{0.8}Cu_{0.2}O_{3-\delta}$ (SSFCu), $Ce_{0.8}Sm_{0.2}O_{2-\delta}$ (SDC), $Ba_{0.5}Sr_{0.5}FeO_{3-\delta}$ (BSF), $PrBaFe_2O_{5+\delta}$ (PBF), $PrBaCo_2O_{5+\delta}$ (PBC).

Surprisingly, the R_p of HMFCs is lower than that of the PAFCs when using triple-conducting ($H^+/O^{2-}/e^-$) cathode materials[19–23] (**Figure 4-14**). As widely recognized, protonic ceramic fuel cells with triple-conducting cathodes have lower cathodic R_p than cells with MIEC cathodes because the effective reaction areas of the former extend to the overall electrode surface owing to the proton conductivity, whereas those of the latter are limited only to the TPB. Nevertheless, the R_p values of the current HMFCs are remarkably lower than those of the triple-conducting cathode PAFCs, regardless of the limited TPB areas of the poor proton-conducting LSCF cathode,[43] which provides a clear verification for the much faster reaction frequency at TPBs in HMFCs than that in conventional PAFCs.

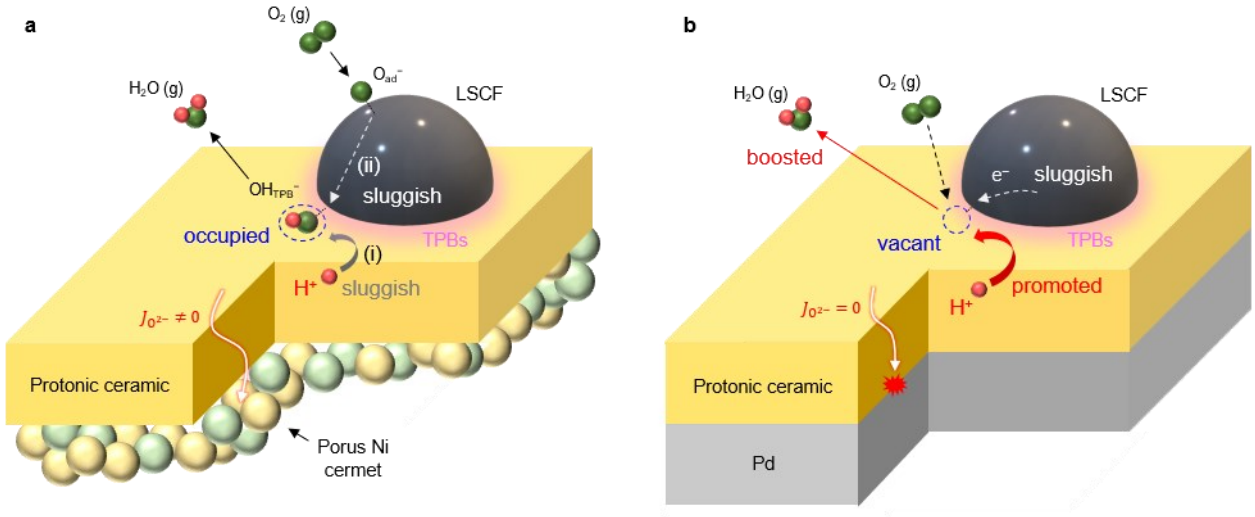

Figure 4-15. (a) Cathode reaction mechanism for conventional porous Ni cermet anode support thin film PAFCs. (b) Proposed mechanism of the fast cathode reaction at TPB in HMFCs.

Previous systematic studies[9,11,12] have clarified that the rate-controlling steps of various MIEC cathode materials including LSCF for PAFCs could be assigned to (i) the interfacial proton transfer to TPBs (**Figure 4-15a**) and (ii) the diffusion of O_{ad}^{-} from catalytic sites to TPBs (**Figure 4-15a**) with a characteristic capacitance of ~10^{-5} F cm^{-2} and ~10^{-2}–10^{-1} F cm^{-2}, respectively. Apparently, O diffusion is not rate-limiting for the cathode reaction in HMFCs. The effective electrode reaction area for the oxygen reduction reaction on MIEC cathodes is related to the characteristic length, D/k, where D and k denote the tracer diffusion coefficient and oxygen surface exchange coefficient, respectively.[24,44] These results indicate that the oxygen surface exchange near the TPB is sufficiently fast in HMFCs, and the cathode reaction is thus completed within TPB zones without via the long-range diffusion of O adatoms.

Combining these results and previous data gives an insight into the difference between PAFC and HMFC for the cathode reaction, as shown in **Figure 4-15**. Since mass-transfer processes from the electrolyte (H^{+}) and cathode (O adatoms) to TPB are sluggish in PAFCs, the catalytic sites on TPBs must be occupied by reaction intermediaries for a relatively long period before proceeding to the subsequent reaction step, as shown in **Figure 4-15a**, which may result in a stagnant cathode reaction. Meanwhile, a high turnover frequency of the cathode reaction cycle at TPBs is realized in HMFCs, assisted by the enhanced proton transfer to TPBs (**Figure 4-15b**). Although the proton transfer involves large overpotentials in both PAFCs[5–9,11,12,45] and HMFCs, that in HMFCs is faster than that in PAFCs because of the much higher interfacial $\nabla[OH_O^{\bullet}]$ of the former than that of the

latter because of proton pumping **(Figure 4-2d)**. The fast proton transfer to TPBs boosts the water formation and the subsequent desorption at TPBs, accelerating the regeneration of catalytic sites (**Figure 4-15b**), which leads to an increase in the rate of oxygen surface exchange and enhances the turnover frequency at TPBs. As a result, the cathode reactions in the vicinity of TPBs can progress without the requirement of long-range oxygen diffusion if the relatively slow reaction steps, namely, proton and electron transfer, progress smoothly with a reasonable overpotential. The resultant reaction pathway significantly reduces the E_a of the cathode reaction and results in a much lower E_a than in conventional cells with an LSCF cathode (**Figure 4-14a**). These results indicate that proton pumping modifies the cathode reaction pathway by promoting interfacial proton transfer to TPBs, thus enabling fast cathode reactions in HMFCs.

The kinetics of the cathode reaction modified by proton pumping are controlled by electron transfer, in addition to proton transfer to TPBs. Consequently, overpotential synergically reduces the R_p of HMFCs, which becomes only 0.54 Ω cm^2 after applying a cell bias of −0.4 V for Sc50-cell at 400 °C, which is one-order of magnitude lower than the value of recently reported triple-conducting materials for PAFCs:[19] $BaCo_{0.7}(Ce_{0.8}Y_{0.2})_{0.3}O_{3-\delta}$ (5.96 Ω cm^2) and $BaCo_{0.4}Fe_{0.4}Zr_{0.1}Y_{0.1}O_{3-\delta}$ (11.7 Ω cm^2) at 400 °C, but it is still higher than the benchmark[46] of HMFCs (0.21 Ω cm^2). These discriminative, outstanding features of bias-dependent R_p in HMFCs should open a new route for the design of electrochemical devices that can achieve close-to-zero polarization even at temperatures below 400 °C.

4.4.4. Comparison of HMFCs with LT-SOFCs

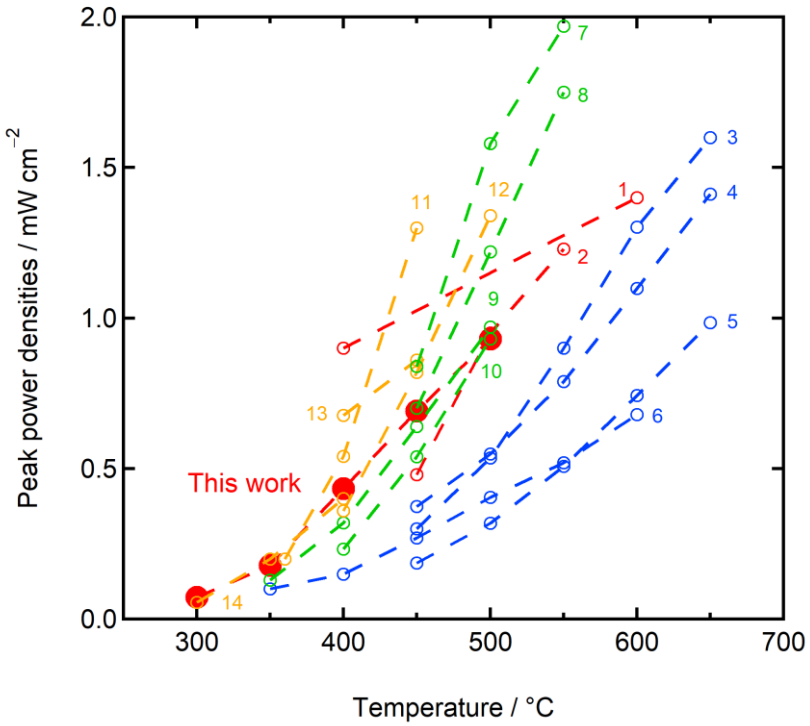

Figure 4-16. Comparison of the peak power densities of the current HMFC (solid plot) with those of previously reported LT-SOFCs (hollow plot): HMFCs (red), SOFCs (green), micro-SOFCs (orange), and PAFCs (blue). The numbers indicate the following references: 1. N. Ito et al.,[46] 2. S. W. Jeong et al.,[Chapter 3] 3. H. An et al.,[29] 4. S. Choi et al.,[21] 5. Y. Song et al.,[19] 6. C. Duan et al.,[28] 7. J. Lee et al.,[47] 8. M. Li et al.,[48] 9. C. Duan et al.,[49] 10. S. S. Shin et al.,[50] 11. J. An et al.,[51] 12. C. Chao et al.,[52] 13. P. C. Su et al.,[53] and 14. H. Huang et al.[54].

The aforementioned results unambiguously demonstrated that the Sc50-cell with higher oxygen vacancies can yield a comparatively high PPD of 0.4 W cm^{-2} at 400 °C owing to proton pumping.

The performances are compared with those of other key approaches: Oxide ion conducting solid oxide fuel cells (SOFCs) with innovative materials and micro-SOFCs that have submicron-thick electrolyte films. **Figure 4-16** summarizes the PPDs of our Sc50-cell (solid plot) and the previously reported ceramic fuel cells, including HMFCs (red),[20] SOFCs (green),[47–50] micro-SOFCs[51–54] (orange) and PAFCs[19,21,28,29] (blue) for a comparison. Although the PPDs in current cells do not reach the benchmark of HMFCs at 400 °C,[46] our cell outperforms previously reported PAFCs and SOFCs at temperatures below 400 °C. The Sc50-cells possess an R_p of 1.34 and 3.09 Ω cm^2 with a cell bias of −0.4 V (**Figure 4-13**), and thus gain PPDs of 178 and 73 mW cm^{-2} with OCV of more than 1.0 V at 350 and 300 °C (**Figure 4-4a**), respectively, which are comparable to those of micro-SOFCs based on Pt cathode and YSZ nanofilms. The low-temperature performance may be improved through material and process optimization by accounting for the gap between the HMFCs' benchmark and our cells. For commercial use in HMFCs, it is imperative to make the Pd anode much thinner or to develop HMFCs based on non-Pd hydrogen-permeable metals, such as vanadium[55,56] and titanium[57] base alloys in future research.

4.5. Conclusion

In this study, I demonstrated that proton pumping because of oxide ion blocking at H_2-permeable metal anodes promotes proton transfer to TPBs at cathode interfaces and thus involves the switching of the reaction pathway and the reduction of the overall cathode reaction resistance. The enhanced proton transfer accelerates the associative desorption of water with the regeneration of catalytic sites

near TPBs, thereby enabling the cathode reaction cycle to progress at TPB without the need for the long surface diffusion of O adatoms. The rate-controlling step of the cathode reaction in conventional PAFCs has been attributed to the surface diffusion of O adatoms in addition to interfacial proton transfer, but that in HMFCs changes to a bias-controlling charge transfer reaction. Hence, the polarization resistances of the HMFCs decrease significantly with bias, leading to their excellent electrochemical performance. The Sc50-cell is capable of driving enhanced proton pumping owing to the relatively high oxygen vacancy concentration under a wet atmosphere, thus achieving an R_p of 0.54 Ω cm^2 at 400 °C under a DC condition of −0.4 V vs. OCV with the conventional LSCF cathode. Furthermore, these values are one order of magnitude lower than those of recently reported triple-conducting cathode materials. These findings strongly suggest that proton pumping modifies the nature of cathodic TPBs to enable fast cathode reactions at low temperatures; thus, the HMFC configuration may offer an alternative solution for the inherent technological challenge of low-temperature protonic ceramic fuel cell cathodes without relying on the ion conductivity of electrode materials. The discriminative features of bias-dependent R_p in HMFCs will open a new route for the design of electrochemical devices that can achieve close-to-zero polarization even at temperatures below 400 °C.

4.6. References

1. H. Zhu and R. J. Kee, "Membrane polarization in mixed-conducting ceramic fuel cells and electrolyzers" *Int. J. Hydrogen Energy* **2016**, 41, 2931.

2. T. H. Wan, M. Saccoccio, C. Chen and F. Ciucci, "Influence of Discretization Methods on the Distribution of Relaxation Times Deconvolution: Implementing Radial Basis Functions with DRTtools" *Electrochimica Acta* **2015**, 184, 483.

3. K. Bae, D. H. Kim, H. J. Choi, J. W. Son and J. H. Shim, "High-Performance Protonic Ceramic Fuel Cells with 1 μm Thick Y:Ba(Ce, Zr)O_3 Electrolytes" *Adv. Energy Mater.* **2018**, 8, 1801315.

4. J. Hyodo, K. Kitabayashi, K. Hoshino, Y. Okuyama and Y. Yamazaki, "Fast Stable Proton Conduction in Heavily Scandium-Doped Polycrystalline Barium Zirconate at Intermediate Temperatures" *Adv. Energy Mater.* **2020**, 10, 2000213.

5. T. Wu, Y. Zhao, R. Peng and C. Xia, "Nano-sized $Sm_{0.5}Sr_{0.5}CoO_{3-\delta}$ as the cathode for solid oxide fuel cells with proton-conducting electrolytes of $BaCe_{0.8}Sm_{0.2}O_{2.9}$" *Electrochimica Acta* **2009**, 54, 4888.

6. J. Dailly, S. Fourcade, A. Largeteau, F. Mauvy, J. C. Grenier and M. Marrony, "Perovskite and A_2MO_4-type oxides as new cathode materials for protonic solid oxide fuel cells" *Electrochimica Acta* **2010**, 55, 5847.

7. J. Dailly, F. Mauvy, M. Marrony, M. Pouchard and J. C. Grenier, "Electrochemical properties of perovskite and A_2MO_4-type oxides used as cathodes in protonic ceramic half cells" *J. Solid State Electrochem.* **2011**, 15, 245.

8. S. Ricote, N. Bonanos, P. M. Rorvik and C. Haavik, "Microstructure and performance of $La_{0.58}Sr_{0.4}Co_{0.2}Fe_{0.8}O_{3-\delta}$ cathodes deposited on $BaCe_{0.2}Zr_{0.7}Y_{0.1}O_{3-\delta}$ by infiltration and spray pyrolysis" *J. Power Sources* **2012**, 209, 172.

9. S. Ricote, N. Bonanos, F. Lenrick and R. Wallenberg, "$LaCoO_3$: Promising cathode material for protonic ceramic fuel cells based on a $BaCe_{0.2}Zr_{0.7}Y_{0.1}O_{3-\delta}$ electrolyte" *J. Power Sources* **2012**, 218, 313.

10. Y. Aoki, S. Kobayashi, T. Yamaguchi, E. Tsuji, H. Habazaki, K. Yashiro, T. Kawada and T. Ohtsuka, "Electrochemical Impedance Spectroscopy of High-Efficiency Hydrogen Membrane Fuel Cells Based on Sputter-Deposited $BaCe_{0.8}Y_{0.2}O_{3-\delta}$ Thin Films" *J. Phys. Chem. C* **2016**, 1210, 15976.

11. F. He, T. Wu, R. Peng and C. Xia, "Cathode reaction models and performance analysis of $Sm_{0.5}Sr_{0.5}CoO_{3-\delta}$–$BaCe_{0.8}Sm_{0.2}O_{3-\delta}$ composite cathode for solid oxide fuel cells with proton conducting electrolyte" *J. Power Sources* **2009**, 194, 263.

12. R. Peng, T. Wu, W. Liu, X. Liu and G. Meng, "Cathode processes and materials for solid oxide

fuel cells with proton conductors as electrolytes" *J. Mater. Chem.* **20** (2010) 6218.

13. S. M. Choi, H. An, K. J. Yoon, B. K. Kim, H. W. Lee, J. W. Son, H. Kim, D. Shin, H. I. Ji and J. H. Lee, "Electrochemical analysis of high-performance protonic ceramic fuel cells based on a columnar-structured thin electrolyte" *Applied Energy* **2019**, 233–234, 29.

14. G. E. Murch, "The haven ratio in fast ionic conductors" *Solid State Ionics* **1982**, 7, 177.

15. B. O. H. Grope, T. Zacherle, M. Nakayama and M. Martin, "Oxygen ion conductivity of doped ceria: A Kinetic Monte Carlo study" *Solid State Ionics* **2012**, 225, 476.

16. Bard, A. J.; Faulkner, L. R. *Electrochemical Methods*: *Fundamentals and Applications*, 2nd ed.; John Wiley & Sons, Inc.: 2000.

17. L. Yang, Z. Liu, S. Wang, Y. M. Choi, C. Zuo and M. Liu, "A mixed proton, oxygen ion, and electron conducting cathode for SOFCs based on oxide proton conductors" *J. Power Sources* **2010**, 195, 471.

18. E. Perry, M. J. Sever and S. A. Barnett, "Electrochemical performance of (La,Sr)(Co,Fe)O_3–(Ce,Gd)O_3 composite cathodes" *Solid State Ionics* **2002**, 148, 27.

19. Y. Song, Y. Chen, W. Wang, C. Zhou, Y. Zhong, G. Yang, W. Zhou, M. Liu and Z. Shao, "Self-Assembled Triple-Conducting Nanocomposite as a Superior Protonic Ceramic Fuel Cell Cathode" *Joule* **2019**, 3, 1.

20. N. Wang, H. Toriumi, Y. Sato, C. Tang, T. Nakamura, K. Amezawa, S. Kitano, H. Habazaki and Y. Aoki, "$La_{0.8}Sr_{0.2}Co_{1-x}Ni_xO_{3-\delta}$ as the Efficient Triple Conductor Air Electrode for Protonic Ceramic Cells" *ACS Appl. Energy Mater.* **2021**, 4, 554.

21. S. Choi, C. J. Kucharczyk, Y. Liang, X. Zhang, I. Takeuchi, H. I. Ji and S. M. Haile, "Exceptional power density and stability at intermediate temperatures in protonic ceramic fuel cells" *Nat. Energy* **2018**, 3, 202.

22. R. Ren, Z. Wang, C. Xu, W. Sun, J. Qiao, D. W. Rooney and K. Sun, "Tuning the defects of the triple conducting oxide $BaCo_{0.4}Fe_{0.4}Zr_{0.1}Y_{0.1}O_{3-\delta}$ perovskite toward enhanced cathode activity of protonic ceramic fuel cells" *J. Mater. Chem. A* **2019**, 7, 18365.

23. Y. Zhou, E. Liu, Y. Chen, Y. Liu L. Zhang, W. Zhang, Z. Luo, N. Kane, B. Zhao, L. Soule, Y. Niu, Y. Ding, H. Ding, D. Ding and M. Liu, "An Active and Robust Air Electrode for Reversible Protonic Ceramic Electrochemical Cells" *ACS Energy Lett.* **2021**, 6, 1511.

24. Z. Gao, L. V. Mogni, E. C. Miller, J. G. Railsback and S. A. Barnett, "A perspective on low-temperature solid oxide fuel cells" *Energy Environ. Sci.* **2016**, 9, 1602.

25. Y. L. Lee, J. Kleis, J. Rossmeisl, Y. S. Horn and D. Morgan, "Prediction of solid oxide fuel cell cathode activity with first-principles descriptors" *Energy Environ. Sci.* **2011**, 4, 3966.

26. K. Bae, D. Y. Jang, H. J. Choi, D. Kim, J. Hong, B. K. Kim, J. H. Lee, J. W. Son and J. H. Shim,

"Demonstrating the potential of yttrium-doped barium zirconate electrolyte for high-performance fuel cells" *Nat. Commun.* **2017**, 8, 14553.

27. G. Taillades, P. Pers, V. Mao and M. Taillades, "High performance anode-supported proton ceramic fuel cell elaborated by wet powder spraying" *Int. J. Hydrogen Energy* **2016**, 41, 12330.

28. C. Duan, J. Tong, M. Shang, S. Nikodemski, M. Sanders, S. Ricote, A. Almansoori and R. O'Hayre, "Readily processed protonic ceramic fuel cells with high performance at low temperatures" *Science* **2015**, 349, 1321.

29. H. An, H. W. Lee, B. K. Kim, J. W. Son, K. J. Yoon, H. Kim, D. Shin, H. I. Ji and J. H. Lee, "A 5×5 cm^2 protonic ceramic fuel cell with a power density of 1.3 W cm^{-2} at 600 °C" *Nat. Energy* **2018**, 3, 870.

30. J. Kim, S. Sengodan, G. Kwon, D. Ding, J. Shin, M. Liu and G. Kim, "Triple-Conducting Layered Perovskites as Cathode Materials for Proton-Conducting Solid Oxide Fuel Cells" *ChemSusChem* **2014**, 7, 2811.

31. N. Nasani, D. Ramasamy, S. Mikhalev, A. V. Kovalevsky and D. P. Fagg, "Fabrication and electrochemical performance of a stable, anode supported thin $BaCe_{0.4}Zr_{0.4}Y_{0.2}O_{3-\delta}$ electrolyte Protonic Ceramic Fuel Cell" *J. Power Sources* **2015**, 278, 582.

32. R. Ren, Z. Wang, X. Meng, X. Wang, C. Xu, J. Qiao, W. Sun and K. Sun, "Tailoring the Oxygen Vacancy to Achieve Fast Intrinsic Proton Transport in a Perovskite Cathode for Protonic Ceramic Fuel Cells" *ACS Appl. Energy Mater.* **2020**, 3, 4914.

33. N. Wang, S. Hinokuma, T. Ina, C. Zhu, H. Habazaki and Y. Aoki, "Mixed proton–electron–oxide ion triple conducting manganite as an efficient cobalt-free cathode for protonic ceramic fuel cells" *J. Mater. Chem. A* **2020**, 8, 11043.

34. L. Bi, E. Fabbri and E. Traversa, "Effect of anode functional layer on the performance of proton-conducting solid oxide fuel cells (SOFCs)" *Electrochem. Commun.* **2012**, 16, 37.

35. Z. Wang, M. Liu, W. Sun, D. Ding, Z. Lu and M. Liu, "A mixed-conducting $BaPr_{0.8}In_{0.2}O_{3-d}$ cathode for proton-conducting solid oxide fuel cells" *Electrochem. Commun.* **2013**, 27, 19.

36. S. Wang, L. Zhang, L. Zhang, K. Brinkman and F. Chen, "Two-step sintering of ultrafine-grained barium cerate proton conducting ceramics" *Electrochim. Acta* **2013**, 87, 194.

37. Y. Ling, X. Zhang, S. Wang, L. Zhao, B. Lin and X. Liu, "A cobalt-free $SrFe_{0.9}Sb_{0.1}O_{3-d}$ cathode material for proton-conducting solid oxide fuel cells with stable $BaZr_{0.1}Ce_{0.7}Y_{0.1}Yb_{0.1}O_{3-\delta}$ electrolyte" *J. Power Sources* **2010**, 195, 7042.

38. M. Shang, J. Tong and R. O'Hayre, "A promising cathode for intermediate temperature protonic ceramic fuel cells: $BaCo_{0.4}Fe_{0.4}Zr_{0.2}O_{3-\delta}$" *RSC Adv.* **2013**, 3, 15769.

39. J. Dailly, G. Taillades, M. Ancelin, P. Pers and M. Marrony, "High performing

$BaCe_{0.8}Zr_{0.1}Y_{0.1}O_{3-\delta}$–$Sm_{0.5}Sr_{0.5}CoO_{3-\delta}$ based protonic ceramic fuel cell" *J. Power Sources* **2017**, 361, 221.

40. Y. Ling, J. Yu, B. Lin, X. Zhang, L. Zhao and X. Liu, "A cobalt-free $Sm_{0.5}Sr_{0.5}Fe_{0.8}Cu_{0.2}O_{3-\delta}$–$Ce_{0.8}Sm_{0.2}O_{2-\delta}$ composite cathode for proton-conducting solid oxide fuel cells" *J. Power Sources* **2011**, 196, 2631.

41. H. Ding and X. Xue, "$BaZr_{0.1}Ce_{0.7}Y_{0.1}Yb_{0.1}O_{3-\delta}$ electrolyte-based solid oxide fuel cells with cobalt-free $PrBaFe_2O_{5+\delta}$ layered perovskite cathode" *J. Power Sources* **2010**, 195, 7038.

42. L. Zhao, B. He, B. Lin, H. Ding, S. Wang, Y. Ling, R. Peng, G. Meng and X. Liu, "High performance of proton-conducting solid oxide fuel cell with a layered $PrBaCo_2O_{5+\delta}$ cathode" *J. Power Sources* **2009**, 194, 835.

43. H. I. Ji, S. M. Choi, K. J. Yoon, J. W. Son, B. K. Kim, H. W. Lee and J. H. Lee, "Influence of wet atmosphere on electrical and transport properties of lanthanum strontium cobalt ferrite cathode materials for protonic ceramic fuel cells" *Solid State Ionics* **2013**, 249–250, 112.

44. S. B. Adler, "Electrode Kinetics of Porous Mixed-Conducting Oxygen Electrodes" *J. Electrochem. Soc.* **1996**, 143, 3554.

45. A. Grimaud, F. Mauvy, J. M. Bassat, S. Fourcade, L. Rocheron, M. Marrony and J. C. Grenier, "Hydration Properties and Rate Determining Steps of the Oxygen Reduction Reaction of Perovskite-Related Oxides" *J. Electrochem. Soc.* **2012**, 159, B683.

46. N. Ito, M. Iijima, K. Kimura and S. Iguchi, "New intermediate temperature fuel cell with ultra-thin proton conductor electrolyte" *J. Power Sources* **152** (2005) 200.

47. J. G. Lee, J. H. Park and Y. G. Shul, "Tailoring gadolinium-doped ceria-based solid oxide fuel cells to achieve 2 W cm^{-2} at 550 °C" *Nat. Commun.* **2014**, 5, 4045.

48. M. Li, M. Zhao, F. Li, W. Zhou, V. K. Peterson, X. Xu, Z. Shao, I. Gentle and Z. Zhu, "A niobium and tantalum co-doped perovskite cathode for solid oxide fuel cells operating below 500 °C" *Nat. Commun.* **2017**, 8, 13990.

49. C. Duan, D. Hook, Y. Chen, J. Tong and R. O'Hayre, "Zr and Y co-doped perovskite as a stable, high performance cathode for solid oxide fuel cells operating below 500 °C" *Energy Environ. Sci.* **2017**, 10, 176.

50. S. S. Shin, J. H. Kim, K. Y. Bae, K. T. Lee, S. M. Kim, J. W. Son, M. Choi and H. Kim, "Multiscale structured low-temperature solid oxide fuel cells with 13 W power at 500 °C" *Energy Environ. Sci.* **2020**, 13, 3459.

51. J. An, Y. B. Kim, J. Park, T. M. Gur and F. B. Prinz, "Three-Dimensional Nanostructured Bilayer Solid Oxide Fuel Cell with 1.3 W/cm^2 at 450 °C" *Nano Lett.* **2013**, 13, 4551.

52. C. C. Chao, C. M. Hsu and Y. C. F. B. Prinz, "Improved Solid Oxide Fuel Cell Performance with

Nanostructured Electrolytes" *ACS Nano* **2011**, 5, 5692.

53. P. C. Su, C. C. Chao, J. H. Shim, R. Fasching and F. B. Prinz, "Solid Oxide Fuel Cell with Corrugated Thin Film Electrolyte" *Nano Lett*. **2008**, 8, 2289.

54. H. Huang, M. Nakamura, P. Su, R. Fasching, Y. Saito and F. B. Prinz, "High-Performance Ultrathin Solid Oxide Fuel Cells for Low-Temperature Operation" *J*. *Electrochem*. *Soc*. **2007**, 154, B20.

55. C. Nishimura, M. Komaki, S. Hwang and M. Amano, "V–Ni alloy membranes for hydrogen purification" *J*. *Alloys Compd*. **2002**, 330–332, 902.

56. T. Ozaki, Y. Zhang, M. Komaki and C. Nishimura, "Hydrogen permeation characteristics of V–Ni–Al alloys" *Int*. *J*. *Hydrogen Energy*, **2003**, 28, 1229.

57. K. Hashi, K. Ishikawa, T. Matsuda and K. Aoki, "Hydrogen permeation characteristics of multi-phase Ni–Ti–Nb alloys" *J*. *Alloys Compd*. **2004**, 368, 215.

Chapter 5

Development of hydrogen-permeable metal-support-type fuel cell based on Pd-alternative hydrogen permeable anode

5.1. Objective of chapter 5

In the chapters 3 and 4, it is demonstrated that the configuration of hydrogen-permeable metal-support-type fuel cell (HMFC) is favorable for efficient power generation at low temperature regime (300–500 °C). The conventional HMFC uses a bulk Pd foils in the hydrogen permeable anode, and the resource scarcity of Pd precludes large-scale applications of HMFC. Hence, it is strongly required to develop HMFCs based on Pd-alternative hydrogen permeable metals.

The group V metals such as V, Nb and Ta are attractive candidates for Pd-alternative hydrogen permeable materials in terms of cost and hydrogen permeability. In fact, they exhibit greater hydrogen permeability than Pd-based alloys, because the formers have body centered cubic (BCC) and the relatively large free volume of the structure allows high hydrogen solubility and diffusivity, compared with face centered body cubic structure of Pd.[1,2] However, such BCC metals suffer from severe hydrogen embrittlement,[3] thereby difficulty encountered in their practical applications. In addition, the BCC metals have no catalytic ability to dissociate hydrogen molecules.[1] To alleviate these issues, Pd-plated BCC alloys have been studied intensively.[4–11] A recent study has demonstrated that Pd-plated V– 15% Ni alloy, $V_{0.85}Ni_{0.15}$, exhibits excellent durability, yielding stable hydrogen

permeability for 2 weeks at 300 °C.[11] In this chapter, HMFCs based on transition metal base hydrogen-permeable anode, i.e., the V–Ni alloy foils, were fabricated to replace the Pd anode.

5.2. Experimental

5.2.1. Preparation of the target for pulsed laser deposition

The $BaZr_{0.1}Ce_{0.7}Y_{0.1}Yb_{0.1}O_{3-\delta}$ (BZCYYb) target was prepared to perform pulsed-laser deposition (PLD). Stoichiometric amounts of starting materials: $BaCO_3$ (High Purity Chemicals, 99.95%), ZrO_2 (High Purity Chemicals, 98%), CeO_2 (High Purity Chemicals, 99.99%), Y_2O_3 (High Purity Chemicals, 99.99%) and Yb_2O_3 (High Purity Chemicals, 99.9%) were ball-milled in ethanol at 350 ppm for 10 h using planetary mills and subsequently dried at 100 °C. The obtained mixed powders were calcined at 1300 °C for 10 h at a ramp rate of 10 °C min^{-1} in ambient air. To ensure the formation of phases, milling and calcination were repeated. Subsequently, the calcined powders were uniaxially pressed into green pellets (21 mm in diameter, 4–5 mm in thickness) under 20 MPa and then pressed under a hydrostatic pressure of 100 MPa in an isostatic press. The green pellets were then sintered at 1500 °C for 8h.

5.2.2. Fabrication of HMFCs

The HMFCs were fabricated by depositing BZCYYb films on a V–Ni alloy ($V_{0.95}Ni_{0.05}$) foil with PdAg coating of 90 nm thickness. The $V_{0.95}Ni_{0.05}$ foils (100 × 100 × 0.1 *d* mm) with 180 nm-thick PdAg coating (180 nm *d*) on both faces were purchased from Taiyo-Kohsan Co. Ltd. The foil was

cleaned by ultrasonication in acetone before deposition. BZCYYb films were grown on V–Ni foil using the pulsed-laser deposition technique with an Ulvac UPS-1000S ultravacuum chamber system. The substrate temperature was set to 300 °C. The oxygen partial pressure in the chamber was set to 1.0 Pa. A 248 nm KrF excimer laser (Coherence COMPEX 109) ablated the targets at a repetition rate of 5 Hz. The laser energy was approximately 105 mJ per a pulse. Finally, a $La_{0.6}Sr_{0.4}Co_{0.2}Fe_{0.8}O_{3-\delta}$ (LSCF) button electrode (7 mmϕ) was screen-printed on the surfaces of the BZCYYb films as a porous cathode using a commercial LSCF paste (FuelcellMaterials). The cell thus obtained is denoted as V–Ni base HMFC. On the other hand, the identical electrolyte film was also deposited on a 50-μm-thick Pd foil for the reference sample. The cell was fabricated by the same process with V–Ni base HMFC. It is denoted as Pd base cell.

5.2.3. Characterization of Sc50 and Sc20 base cells

The crystal structure and phase purity of the deposited films were determined by XRD analysis in the 2θ range between 10° and 80° at a scan rate of 1° min^{-1} using a RIGAKU diffractometer (RIGAKU Rint2000). Scanning transmission electron microscopy (TEM) was carried out using a HITACHI HD-2000 instrument to observe the cross-section of the samples. The specimens for the TEM observation were prepared by focused ion beam microfabrication (HITACHI FB-2100) using post-test samples with scrapped LSCF cathodes.

5.2.4. Electrochemical assessment of HMFCs

The performance of the HMFCs was evaluated by measuring the current–voltage (*I–V*)

relationship and electrochemical impedance spectra at the temperature range of 300–400 °C. The specimen was sealed in a specially designed sample holder with a mica gasket (FuelcellMaterials). Anode and Cathode were contacted with Ni alloy and Pt meshes, respectively, and a thermocouple was placed in close proximity to the cell to obtain the temperature data as accurately as possible. Dry H_2 was fed to the V–Ni anode at a flow rate of 50 sccm min^{-1} and wet air gas was fed to the cathode side at a rate of 50 sccm min^{-1}. The wet gas (pH_2O = 0.023 p_0) was prepared by passing the gases through water at 20 °C. The pH_2 and pO_2 of the anode and cathode gases, respectively, were adjusted using Ar balance gas. Electrochemical impedance spectra and *I–V* characteristics were obtained using a Solartron 1260/1287 system in the frequency range from 10^6 to 0.1 Hz with an AC amplitude of 30 mV under several DC bias voltages.

5.3. Results and discussion

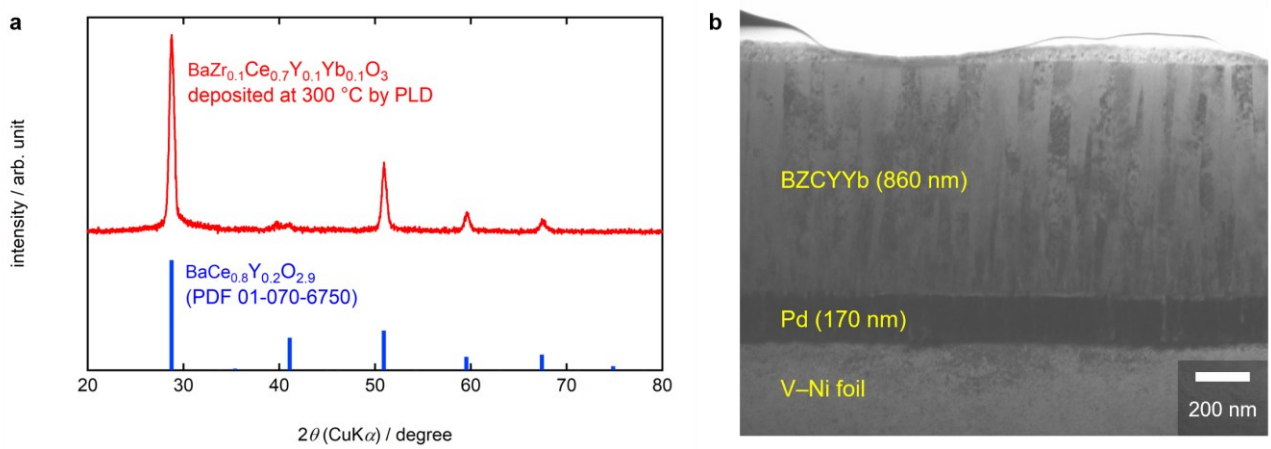

Figure 5-1. (a) XRD pattern of the BZCYYb thin film deposited at 300 °C by PLD. (b) A cross-sectional TEM image of V–Ni base HMFC.

To prevent oxidation of V–Ni substrate, the BZCYYb film was deposited at low temperature of 300 °C under oxygen pressure of 1.0 Pa. **Figure 5-1a** represents XRD pattern of the BZCYYb thin film fabricated by PLD at 300 °C. All peaks in the pattern were assigned to a perovskite structure, confirming the formation of single-phase polycrystalline BZCYYb films. As shown in **Figure 5-1b**, the TEM image confirmed that that the densely packed, clack-free thin films of BZCYYb electrolytes were uniformly formed with the thickness of 860 nm over a wide area of the V–Ni foil anode.

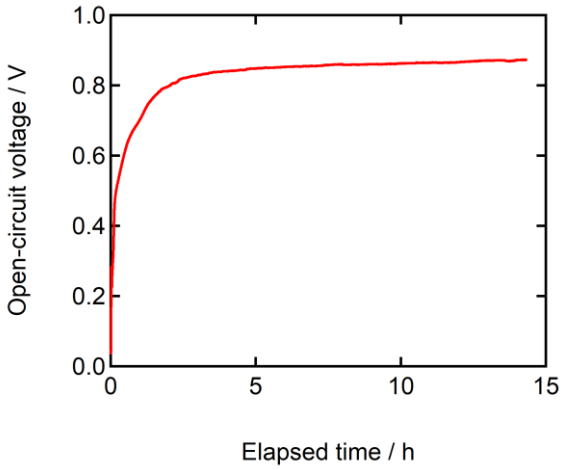

Figure 5-2. A open-circuit voltage profile at 300 °C for the V−Ni base HMFC with the BZCYYb thin film. The anode and cathode atmosphere was suddenly changed at 0 s from 3% wet Ar to the fuel cell atmosphere: Dry pure H_2 at the anode and wet air ($H_2O/O_2/Ar$ = 3/19.4/77.6) at the cathode.

Figure 5-2 shows the open-circuit voltage (OCV) profile after a supply of fuel cell gases at 300 °C for the V–Ni base HMFC with the BZCYYb thin film. The OCV slowly increases and reaches about 0.8 V after 2 h from the atmosphere change, which indicates that V−Ni base cells need to be activated with some thermodynamical processes in order to conduct the cathode and anode reactions at a reasonable overpotential at low temperatures. Then, OCV was maintained at around 0.8 V for over 10 h, which confirms that V–Ni base HMFC is stable under fuel cell atmosphere at 300 °C without undesirable phenomena such as corrosion of V–Ni foil anode.

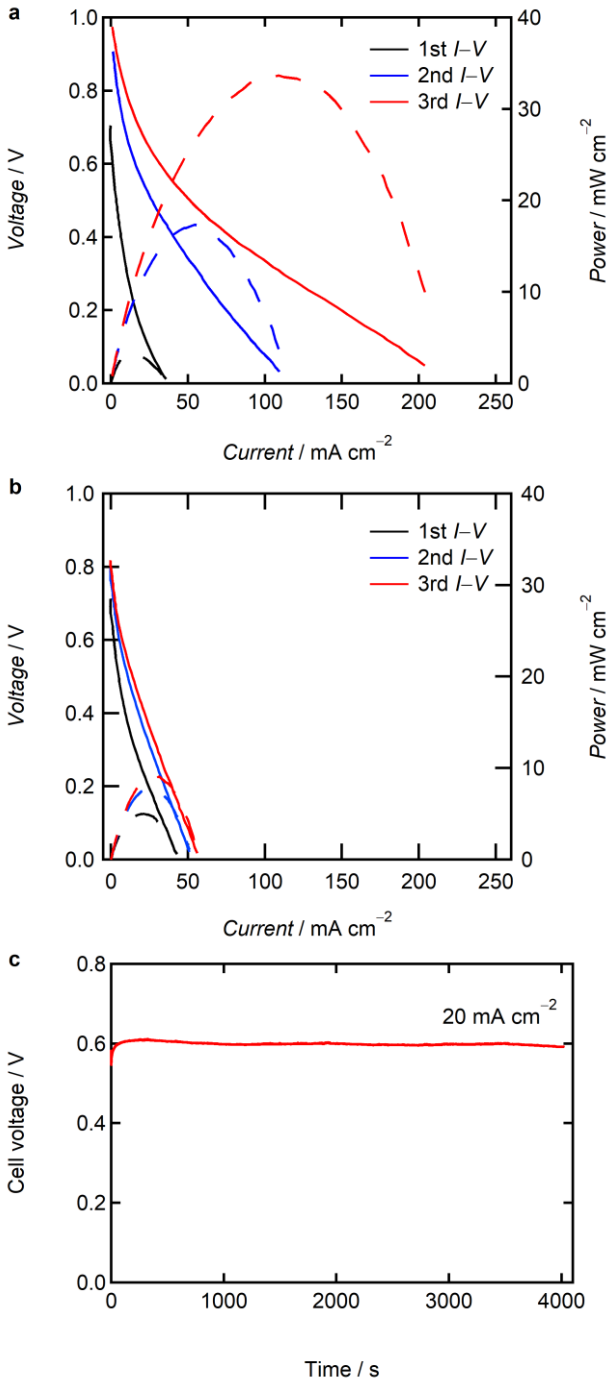

Figure 5-3. *I–V* (solid lines) and *I–P* (dashed lines) characteristics of (a) the V–Ni base HMFC and (b) Pd base HMFC at 300 °C in the fuel cell atmosphere: Dry 100% H_2 at anode and wet air ($H_2O/O_2/Ar = 3/19.4/77.6$) at cathode. The voltage drops associated with equipment resistances were corrected in the *I–V* curves. (c) Chronopotentiometry at a current density of 20 mA cm^{-2} at 300 °C

after the 2nd *I–V* measurement.

Figure 5-3 shows the fuel cell performances of V–Ni and Pd base HMFCs with BZCYYb thin films. Interestingly, both OCV and power increased in step-by-step with successive *I–V* measurements for both V–Ni and Pd base HMFCs, which suggests that electrode reactions were activated with the dc polarization. The OCVs of the V–Ni base HMFC significantly increases from 0.7 V at the first *I–V* measurement to 0.98 V at the third one and the peak power densities were about 10 times enhanced from 3 mW cm^{-2} to 34 mW cm^{-2} with the successive polarization at 300 °C (**Figure 5-3a**). Such tendencies were also observed in the Pd base HMFC, but the enhancement was weaker than those of V–Ni base HMFC (**Figure 5-3b**). The OCVs of the Pd base HMFC increased from 0.7 V to 0.82 V by 3 times *I–V* measurements and the peak power densities from 5 to 9 mW cm^{-2}. It is worth noticing that V–Ni base HMFC exhibited higher peak power densities than Pd base one. The chronopotentiometry confirms that the V–Ni base HMFC yields the current density of 20 mA cm^{-2} with no deterioration for x h, demonstrating that the cell can stably operate at 300 °C even under biased conditions (**Figure 5-3c**).

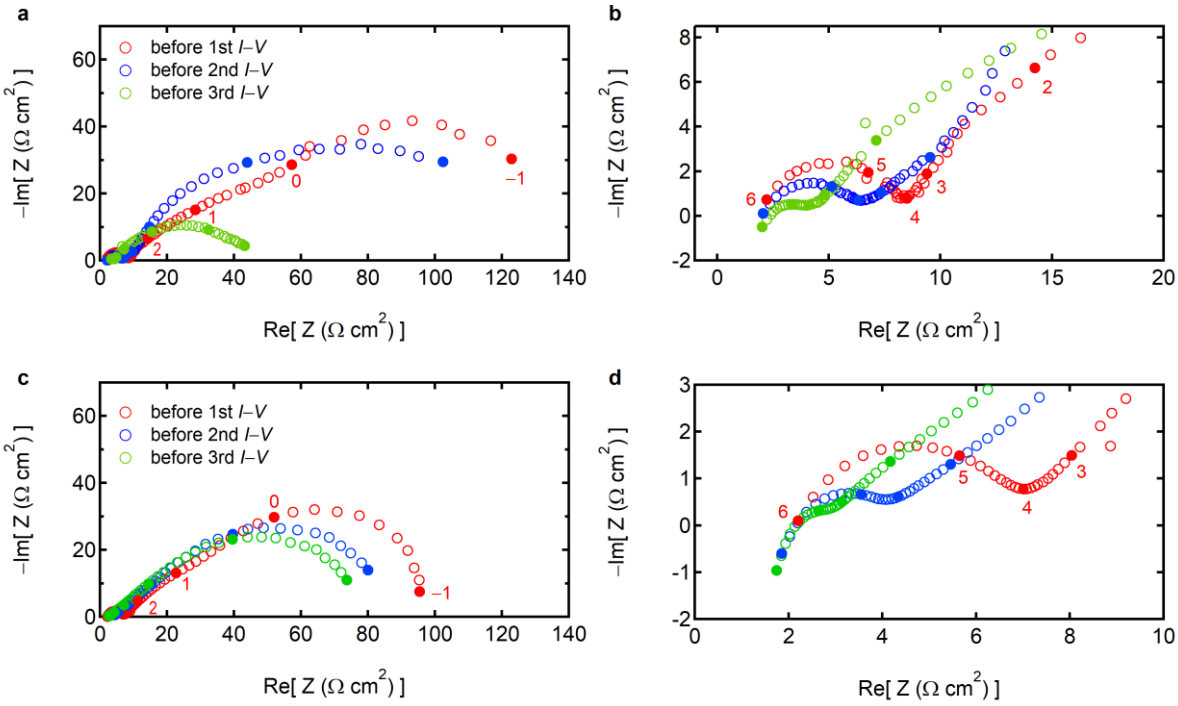

Figure 5-4. Electrochemical impedance spectra for (a, b) V–Ni base HMFC and (c, d) Pd base HMFC under OCV at 300 °C in the fuel cell atmosphere: Dry 100% H_2 at the anode and wet air (H_2O/O_2/Ar = 3/19.4/77.6) at the cathode. (b) and (d) are the magnification in the high frequency region around 10^6–10^4 Hz These were obtained before starting each *I*–*V* measurement shown in **Figure 5-3a** and **b**.

The cell resistances were evaluated using electrochemical impedance spectroscopy to further verify the fuel cell performances. In Nyquist plots of fuel cells, the *x*-intercept at a high frequency represents the ohmic resistance and the broad capacitive semicircle after the intercept corresponds to the polarization resistance. **Figure 5-4** shows the electrochemical impedance spectra of both V–Ni and Pd base HMFCs under OCV condition at 300 °C. Both cells show similar electrochemical responses, including a distinct capacitive semicircle at high frequency regions around 10^6–10^4 Hz and

broad semicircles at low frequency regions around 10^4–10^{-1} Hz. The semicircles at the high frequency regions (10^6–10^4 Hz) are characterized by low capacitors (~ 10^{-7} F cm^{-2}) and thus assigned to electrolyte resistances (R_{ele}); the semicircles at the low frequency regions (10^4–10^{-1} Hz) are probably assigned to interfacial polarization resistances (R_p). With the successive *I–V* measurements, R_{ele} and R_p under OCV condition obviously decrease in both V–Ni and Pd base HMFCs (**Figure 5-4**), which results in the improvement of the *I–V* characteristics (**Figure 5-3**). The reduction of R_p suggests that the electrode reactions were sufficiently activated with dc polarizations, and this activation must cause the increases of OCVs (**Figure 5-3**). The reduction of R_{ele} indicates the increment of bulk proton conductivity of the BZCYYb films, suggesting that proton concentration increased in the electrolyte films due to acquisition of excess amounts of protons by bias-enhanced *proton pumping* during the *I–V* polarizations (see chapter 2) and the 'overhydrated' states thus created were maintained due to the slow relaxation at the low temperature of 300 °C.

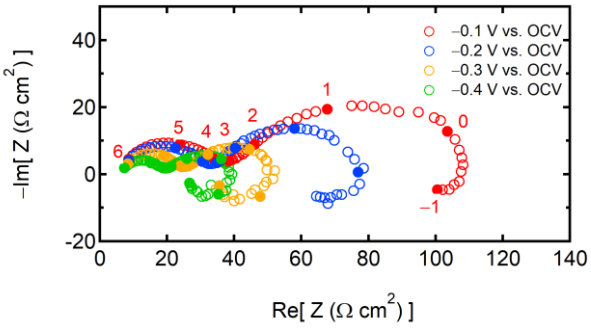

Figure 5-5. Bias-dependence of electrochemical impedance spectra. Nyquist impedance plots of the V–Ni base HMFC at 300 °C under various cell bias values.

As described in the previous chapters, HMFCs are characterized by bias-dependent R_{ele} and R_p due to *proton pumping*, which will be manifested irrespective of any hydrogen-permeable metals according to mathematical model. Impedance spectra were collected under various cell biases to verify the proton pumping of V–Ni base HMFC at 300 °C. The cell bias is calculated by subtracting the OCV from the cell voltage, representing the relative potential of the cathode and anode, respectively. As shown in **Figure 5-5**, the R_{ele} and R_p decreased with increasing negative cell bias, which demonstrates that *proton pumping* occurs in the V–Ni base HMFC. The spectra at 300 °C °C is featured by inductive loops in the low frequency regions (10^0–10^{-1} Hz), which is different behavior from the spectra at higher temperatures. The origins of low frequency inductive loop were not evident in this work, and should be clarified in the future work.

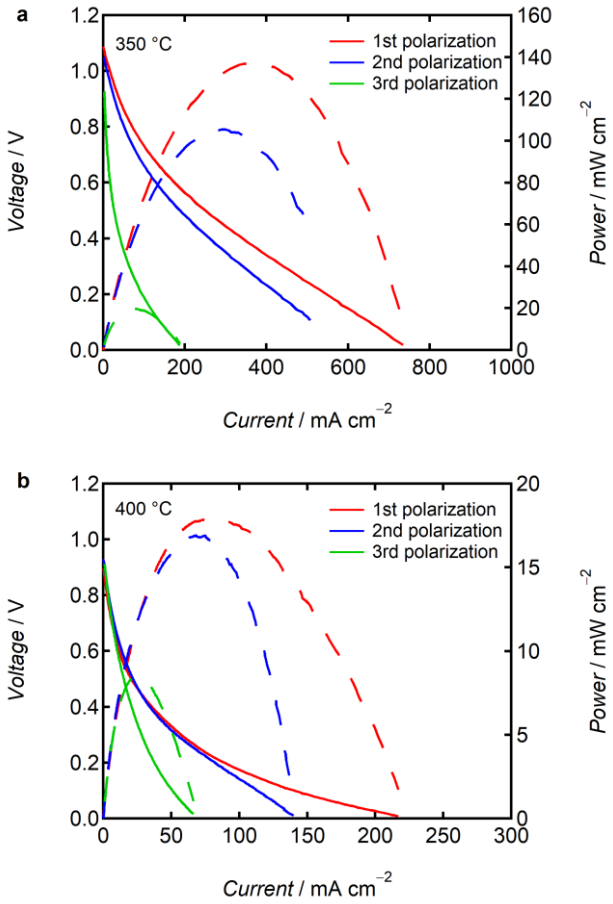

Figure 5-6. *I–V* (solid lines) and *I–P* (dashed lines) characteristics of the V–Ni base HMFC at (a) 350 and (b) 400 °C in the fuel cell atmosphere: Dry 100% H_2 at anode and wet air ($H_2O/O_2/Ar$ = 3/19.4/77.6) at cathode. The voltage drops associated with equipment resistances were corrected in the *I–V* curves.

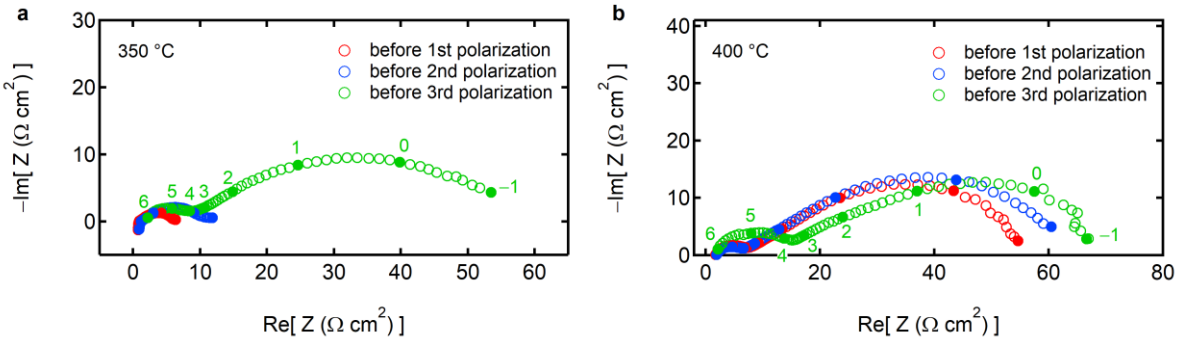

Figure 5-7. Electrochemical impedance spectra for V–Ni base HMFC under OCV cell in the fuel cell atmosphere: Dry 100% H_2 at the anode and wet air ($H_2O/O_2/Ar$ = 3/19.4/77.6) at the cathode at (a) 350 and (b) 400 °C. They were obtained before *I–V* measurements that were shown in **Figure 5-6**.

The V–Ni base HMFC were evaluated at the higher temperatures, i.e., 350 and 400 °C (**Figure 5-6**). The cell exhibited a noticeable peak power density as high as 137 mW cm^{-2} at 350 °C with OCV of more than 1.0 V in the first *I–V* measurement (**Figure 5-6a**). Unfortunately, the peak power densities abruptly deteriorated with the additional *I–V* measurements and thus became 19 mW cm^{-2} in the third *I–V* measurement (**Figure 5-6a**). Similar performance deterioration also occurred at 400 °C: The peak power densities at 400 °C decreased from 18 to 8 mW cm^{-2} by three time I-V measurements. **Figure 5-7** shows the electrochemical impedance spectra of V–Ni base HMFC under OCV at 350 and 400 °C. R_{ele} and R_p at 350 °C were relatively small, equaling to 0.83 and 6.0 Ω cm^2, respectively, before the first *I–V* measurement, indicating that the proton conductivity and electrode reaction kinetics were improved by elevated temperature. However, both largely increased with the additional *I–V* measurements (**Figure 5-7a**), resulting the deteriorated performances. At 400 °C, R_{ele}

largely increased after the2nd *I–V* measurement, as shown in **Figure 5-7b**. These results indicate that V–Ni base HMFC is unstable at temperatures above 350 °C due to the prominent degradations of R_{ele} and R_p. However, it is impressive that V–Ni base HMFC could high peak power density of 137 mW cm^{-2} at 350 °C although it was transient, which demonstrates the possibility of high-power HMFCs without the Pd anode operating in low temperature region.

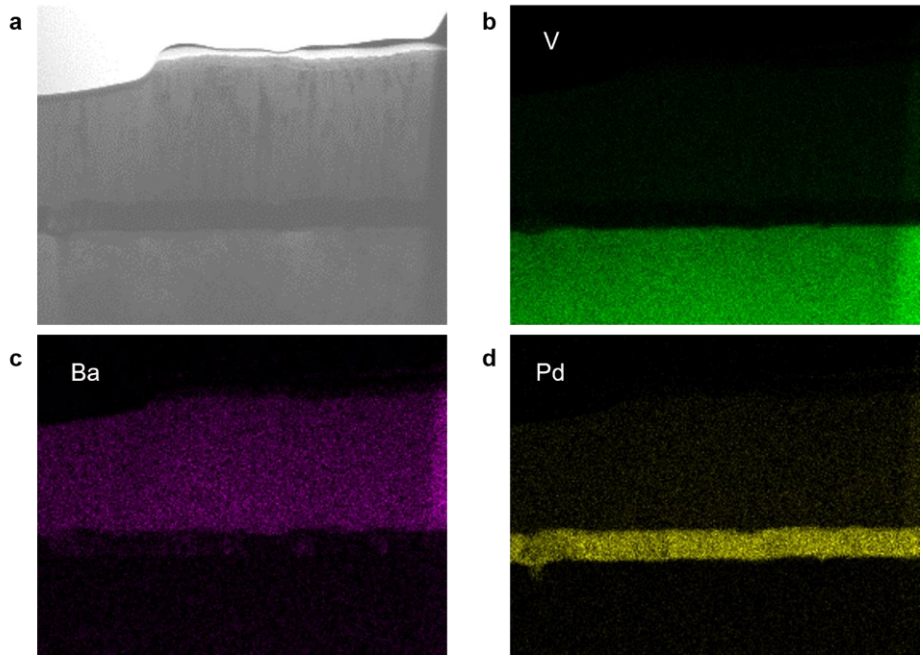

Figure 5-8. Energy-dispersive X-ray spectroscopy mapping results of cross-sectional TEM images of the V–Ni base HMFC obtained after fuel cell test.

Figure 5-8 shows cross-sectional TEM images and their energy-dispersive X-ray spectroscopy mapping results for V–Ni base HMFC that were obtained after fuel cell test. The results show that the electrolyte films maintained a sharp interface with the anode and there was no apparent chemical interdiffusions at the interface (**Figure 5-8**). Thus, it was found that the cell degradations were not attributed to the severe oxidation of V–Ni anode foil.

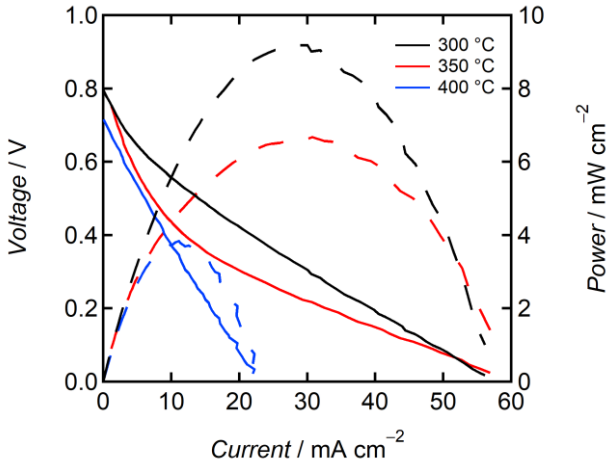

Figure 5-9. *I–V* (solid lines) and *I–P* (dashed lines) characteristics of the Pd base HMFC at 300, 350 and 400 °C in the fuel cell atmosphere: Dry 100% H_2 at anode and wet air ($H_2O/O_2/Ar$ = /19.4/77.6) at cathode. The voltage drops associated with equipment resistances were corrected in the *I–V* curves.

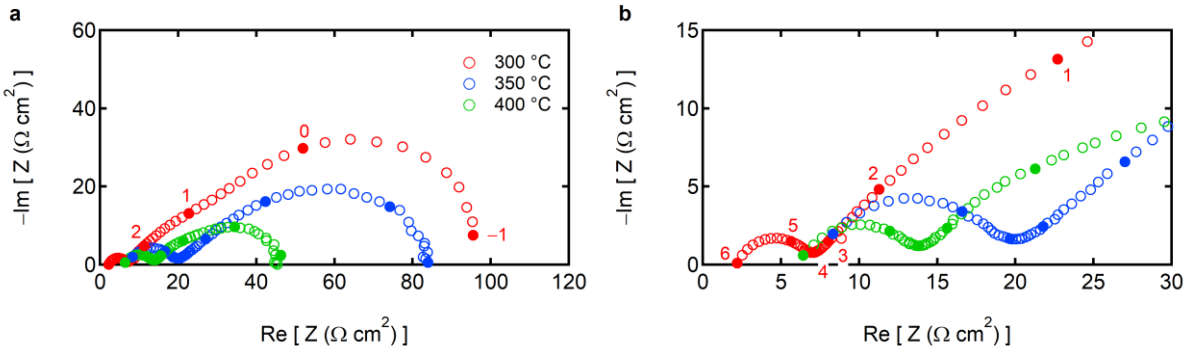

Figure 5-10. (a) Electrochemical impedance spectra for Pd base HMFC under OCV cell in the fuel cell atmosphere: Dry 100% H_2 at the anode and wet air ($H_2O/O_2/Ar$ = 3/19.4/77.6) at the cathode at 300, 350 and 400 °C. (b) the magnified spectra at the high frequency around 10^6–10^4 Hz.

The Pd base HMFC were also evaluated at f 350 and 400 °C, as shown in **Figure 5-9**. The peak power densities deteriorated with increasing the operating temperatures from 9 mW cm^{-2} to 6 to 4

mW cm^{-2} with elevating temperature from 300 °C to 350 to 400 °C, respectively (**Figure 5-9**). The peak power density of the cells were not enhanced with temperatures. **Figure 5-10** shows electrochemical impedance spectra for Pd base HMFC under OCV cell in the fuel cell atmosphere at 300, 350 and 400 °C. The electrolyte resistance, R_{ele}, at the frequency range of 10^6–10^4 Hz obviously increased with increasing. These results confirmed that HMFCs with the BZCYYb thin films deposited at 300 °C undergo degradation at temperatures above 350 °C regardless of anode materials due to the increase of R_{ele}. The origins of the lessened conductivity of the electrolyte is unclear. Although the TEM results could not confirm the chemical interdiffusion and/or delamination at the anodic interfaces for V–Ni base HMFC (**Figure 5-8**), such phenomena would locally occur.

5.4. Conclusion

In this chapter, the prototype of HMFCs based on hydrogen-permeable transition metal anode, i.e., V–Ni alloy foils, were demonstrated. Their power generation properties were improved with successive polarization and thus the peak power density reached 34 mW cm^{-2} at 300 °C. In addition, they exhibited excellent stability under OCV and biased conditions. Proton pumping was also demonstrated with the V–Ni alloy anode, which confirms robustness of the HMFC mathematical model that was described in the chapter 3. Further, they showcased noticeable peak power density of 137 mW cm^{-2} at 350 °C. However, they suffered severe performance degradations due to the deteriorations of R_{ele} and R_p at temperatures above 350 °C. These results demonstrate the possibility of high-power Pd-free HMFCs operating in low temperature region, although there exists still some challenges. These findings marked a milestone in the HMFC technologies and will pave the way for the development of technologically feasible HMFCs.

5.5. References

1. D. A. Cooney, J. D. Way and C. A. Wolden, “A comparison of the performance and stability of Pd/BCC metal composite membranes for hydrogen purification” *Int. J. Hydrogen Energy* **2014**, 39, 19009.

2. V. N. Alimov, A. O. Busnyuk, M. E. Notkin and A. I. Livshits, “Pd–V–Pd composite membranes: Hydrogen transport in a wide pressure range and mechanical stability” *J. Membr. Sci.* **2014**, 457, 103.

3. D. M. Viano, M. D. Dolan, F. Weiss and A. Adibhatla, “Asymmetric layered vanadium membranes for hydrogen separation” *J. Membr. Sci.* **2015**, 487, 83.

4. J. H. Shim, W. S. Ko, K. H. Kim, H. S. Lee, Y. S. Lee, J. Y. Suh, Y. W. Cho and B. J. Lee, “Prediction of hydrogen permeability in V–Al and V–Ni alloys” *J. Membr. Sci.* **2013**, 430, 234.

5. S. Kozhakhmetov, N. Sidorov, V. Piven, I. Sipatov, I. Gabis and B. Arinov, “Alloys based on Group 5 metals for hydrogen purification membranes” *J. Alloys Compd.* **2015**, 645, S36.

6. M. D. Dolan, G. Song, K. G. McLennan, M. E. Kellam and D. Liang, “The effect of Ti on the microstructure, hydrogen absorption and diffusivity of V–Ni alloy membranes” *J. Membr. Sci.* **2012**, 415–416, 320.

7. Y. Nakamura, H. Yukawa, A. Suzuki, T. Nambu, Y. Matsumoto and Y. Murata, “Alloying effects on hydrogen permeability of V without catalytic Pd overlayer” *J. Alloys Compd.* **2015**, 645, S275.

8. Y. S. Lee, C. Ouyang, J. Y. Suh, E. Fleury, Y. W. Cho and J. H. Shim, “Role of alloying elements in vanadium-based binary alloy membranes for hydrogen separation” *J. Membr. Sci.* **2012**, 423–424, 332.

9. V. N. Alimov, A. O. Busnyuk, M. E. Notkin, E. Y. Peredistov and A. I. Livshits, “Hydrogen transport through V–Pd alloy membranes: Hydrogen solution, permeation and diffusion” *J. Membr. Sci.* **2015**, 481, 54.

10. J. Y. Oh, W. S. Ko, J. Y. Suh, Y. S. Lee, B. J. Lee, W. Y. Yoon and J. H. Shim, “Enhanced high temperature hydrogen permeation characteristics of V–Ni alloy membranes containing a trace amount of yttrium” *Scr. Mater.* **2016**, 116, 122.

11. C. Nishimura, M. Komaki, S. Hwang and M. Amano, “V–Ni alloy membranes for hydrogen purification” *J. Alloys Compd.* **2002**, 330–332, 902.

Chapter 6

General Conclusion

In this thesis, thin film protonic ceramic fuel cells were studied for low-temperature solid oxide fuel cells (LT-SOFCs) and the following three themes were approached: (1) porous-anode-support-type fuel cells (PAFCs) were fabricated with chemically stable Zr-rich side $BaZr_xCe_{0.8-x}Y_{0.2}O_{3-\delta}$ (BZCY) electrolyte; (2) the power generation mechanism was clarified for the hydrogen-permeable metal-support-type fuel cells (HMFCs), which show the highest power generation efficiency in the LT-SOFCs community, to give insights into fuel cell device engineering; (3) prototype HMFCs with transition metal base hydrogen-permeable anode were developed. The primary achievements of this thesis were summarized as follows.

In Chapter 1, the backgrounds such as the urgency of climate change and hydrogen economy are introduced, and fuel cell technologies and their markets are briefly reviewed. This showed that we require a novel fuel cell technology bridging the gap between conventional proton-exchange membrane fuel cells and solid oxide fuel cells. Thus, the importance of solid oxide fuel cells operating as low at temperatures of 300–500 °C is highlighted with describing the recent advances in solid-state fuel cell communities, and protonic ceramic fuel cells are suggested as a key solution for operation at such low temperatures. Finally, the objectives of this thesis are stated with its motivations.

In Chapter 2, porous-anode-support-type fuel cells based on Zr-rich $BaZr_xCe_{0.8-x}Y_{0.2}O_{3-\delta}$ ($x \geq$

0.4) electrolyte thin films were fabricated by single firing step at relatively low temperature of 1400 °C through the solid-state reactive sintering method with $Zn(NO_3)_2$ additives. With the aid of Zn additives, the electrolyte films with x = 0.4 and 0.6 showed excellent sinterability along with significant grain growth and thus are densely packed with mm-sized grains, which allows decreasing the detrimental effect of grain-boundary. Accordingly, these electrolyte films with x = 0.4 and 0.6 have higher film conductivity than that reported for the analogous thin film fabricated via wet chemical processes. Thus, the cells exhibited comparatively efficient power generation, yielding peak power densities of about 0.28 and 0.34 W cm^{-2} at 600 °C, respectively. In addition, it was found that the $BaZr_{0.6}Ce_{0.2}Y_{0.2}O_{3-\delta}$ (x = 0.6) film has higher proton conductivity than $BaZr_{0.4}Ce_{0.4}Y_{0.2}O_{3-\delta}$ (x = 0.4) one at temperatures above 500 °C and shows excellent durability under CO_2-containing atmosphere, which enables their use with carbon containing fuels. These findings suggest that $BaZr_{0.6}Ce_{0.2}Y_{0.2}O_{3-\delta}$ is suitable for practical electrolyte and thus encourage the development of high-power fuel cells with $BaZr_{0.6}Ce_{0.2}Y_{0.2}O_{3-\delta}$ electrolyte.

In Chapter 3, the power generation mechanism of HMFC was evident through numerical simulation and electrochemical analysis. Simulation results showed that HMFC and PAFC exhibit completely opposite $[V_O^{\bullet\bullet}]$ distributions with respect to the depth from the anode side. $V_O^{\bullet\bullet}$ defects are redistributed so as to cancel the diffusion driven by oxygen chemical potential because minor oxide ion carriers in BZCY is blocked at Pd/BZCY heterointerface. Hence oxide ions accumulate near the anodic metal/oxide heterointerfaces in HMFC. This redistribution of the $V_O^{\bullet\bullet}$ defects triggers

significant modifications of the $[OH_O^{\bullet}]$ profile: Excess proton carriers are pumped into electrolyte membranes through oxygen chemical potential to compensate for negative charge of the oxide ions accumulated near the heterointerface, which results in overhydrated electrolyte membrane. This phenomenon is herein named *proton pumping*. Moreover, the *proton pumping* is amplified with an increase in the DC output so as to cancel enhanced flux of $V_O^{\bullet\bullet}$ defects by the applied field ($\nabla\phi$). These simulation results were deliberately verified by comparison of electrochemical behavior between PAFC and HMFC comprising the same electrolyte and cathode materials. The DC-enhancement of electrolyte resistances in HMFC was clearly observed by electrochemical impedance spectroscopy, providing clear evidence for the *proton pumping* in HMFCs. Numerical simulations also predicted that the *proton pumping* develops noticeably enlarged concentration gradient of proton in the vicinity of cathode interfaces, facilitating proton interfacial diffusion. In fact, HMFC and PAFC different polarization behavior: The polarization resistances of HMFC exponentially decrease with an increase in the DC output while those of PAFC gradually increase, which implies that charge-transfer steps and mass-transfer steps are rate controlling ones in HMFC and PAFC, respectively. These results confirmed that proton interfacial diffusion, one of the rate-controlling steps for cathode reaction on protonic fuel cells, is significantly fast and thus does not limit the cathode reaction rates in HMFC. Consequently, the HMFCs showed higher power density than PAFCs despite using a conventional O^{2-}/e^{-} conducting $La_{0.6}Sr_{0.4}Co_{0.2}Fe_{0.8}O_{3-\delta}$ (LSCF) cathode. The former showcased peak power densities of 0.95 and 1.3 W cm^{-2} at 500 °C with 1.2-μm- and 2.0-μm-thick

$BaZr_{0.1}Ce_{0.7}Y_{0.2}O_{3-\delta}$ electrolyte films, respectively, which are higher than any other PAFC previously reported. These findings clearly show that the *proton pumping* is crucial to the efficient power generation in HMFC.

In Chapter 4, HMFCs comprising oxygen-nonstoichiometric $BaZr_{1-x}Sc_xO_{3-x/2}$ electrolytes (x = 0.2 and 0.5) were examined in order to demonstrate enhancement of *proton pumping* by oxygen deficiency and design more efficient fuel cells. The thermogravimetry (TG) results confirmed that $BaZr_{1-x}Sc_xO_{3-x/2}$ phase of x = 0.5 (Sc50) has more $V_O^{\bullet\bullet}$ defects than phase of x = 0.2 (Sc20) at around 500 °C under wet atmosphere, which revealed that the Sc50 undergoes more pronounced proton pumping than the Sc20 due to its relatively high $[V_O^{\bullet\bullet}]$. Combined results of numerical and electrochemical analysis demonstrated that *proton pumping* promotes proton transfers toward triple-phase boundaries (TPBs) at cathode interfaces and thereby involve the switching of the reaction pathway. The rate-controlling step of the cathode reaction in conventional PAFCs has been attributed to the surface diffusion of O adatoms in addition to interfacial proton transfer. However, the enhanced proton transfer accelerated the associative desorption of water vapor with the regeneration of catalytic sites near TPBs, thereby enabling the fast cathode reaction cycle progressing at TPB without long-range surface diffusion of O adatoms in HMFC. Hence the cathode reaction of HMFCs tend to be rate-controlled by charge transfer steps rather than diffusion steps, and thus the polarization resistances of the HMFC decreased significantly with bias, leading to their excellent electrochemical performance. The cell with Sc50 underwent more pronounced proton pumping and thus achieved and

the total area-specific resistance of 0.54 Ω cm^2 at 400 °C under a DC condition of −0.4 V vs. OCV with the LSCF material, which is one order of magnitude lower than that of recently reported triple-conducting cathode materials. Consequently, the cell with Sc50 exhibited a peak power density of about 0.43 W cm^{-2} at 400 °C and could yield a stable current density of approximately 0.36 A cm^{-2} for 50 h at 0.7 V and 400 °C. These findings strongly suggest that *proton pumping* modifies the nature of cathodic TPBs to increase oxygen surface exchange at low temperatures. Therefore, the HMFC configuration may offer an alternative solution for the inherent technological challenge of low-temperature protonic ceramic fuel cell, i.e., design of the cathode material without relying on the ion conductivity of electrode materials. The discriminative features of bias-dependent polarization resistance in HMFCs will open a new route to design of electrochemical devices achieving close-to-zero polarization even at low temperature below 400 °C.

In Chapter 5, the prototype of HMFCs based on transition metal base hydrogen-permeable anode, i.e., V–Ni alloy foils, were demonstrated. Their power generation properties were improved with successive polarization and thus the peak power density reached 34 mW cm^{-2} at 300 °C. In addition, they exhibited excellent stability under OCV and biased conditions. Proton pumping was also demonstrated with the V–Ni alloy anode, which confirms robustness of the HMFC mathematical model. Further, they showcased noticeable peak power density of 137 mW cm^{-2} at 350 °C. However, they suffered severe performance degradations due to the prominent deteriorations of R_{ele} and R_p at temperatures above 350 °C. These results demonstrate the possibility of high-power Pd-free HMFCs

operating in low temperature region. These findings marked a milestone in the HMFC technologies and will pave the way for the development of technologically feasible HMFCs.

In conclusion, thin film protonic ceramic fuel cells were demonstrated for LT-SOFCs that bridge the gap between conventional proton-exchange membrane fuel cells and solid oxide fuel cells. The author believes that the findings in this thesis will stimulate academic and industrial interest by giving hints for future advanced LT-SOFC device engineering, and aid broadening the application fields of SOFCs. The author hopes that next-generation HMFC will be a game changing technology in the fuel cell market and thus play a key role in building up hydrogen economy.

List of Publications

1. SeongWoo Jeong, Taisei Kobayashi, Kosuke Kuroda, Hyuna Kwon, Chunyu Zhu, Hiroki Habazaki and Yoshitaka Aoki, "Evaluation of Thin Film Fuel Cells with Zr-rich $BaZr_xCe_{0.8-x}Y_{0.2}O_{3-\delta}$ Electrolyte ($x \geq 0.4$) Fabricated by a Single-Step Reactive Sintering Method" *RSC Adv.* **2018**, *8*, 26309.

2. Seongwoo Jeong, Tomoyuki Yamaguchi, Mamoru Okamoto, Chunyu Zhu, Hiroki Habazaki, Masaharu Nagayama and Yoshitaka Aoki, "Proton Pumping Boosts Energy Conversion in Hydrogen-Permeable Metal-Supported Protonic Fuel Cells" *ACS Appl. Energy Mater.* **2020**, *3*, 1222.

3. SeongWoo Jeong, Ning Wang, Sho Kitano, Hiroki Habazaki and Yoshitaka Aoki, "Metal/Oxide Heterojunction Boosts Fuel Cell Cathode Reaction at Low Temperatures" *Adv. Energy Mater.* **2021**, 11, 2102025.

Other Publications

1. Taisei Kobayashi, Kosuke Kuroda, SeongWoo Jeong, Hyuna Kwon, Chunyu Zhu, Hiroki Habazaki and Yoshitaka Aoki, “Analysis of the Anode Reaction of Solid Oxide Electrolyzer Cells with $BaZr_{0.4}Ce_{0.4}Y_{0.2}O_{3-\delta}$ Electrolytes and $Sm_{0.5}Sr_{0.5}CoO_{3-\delta}$ Anodes” *J. Electrochem. Soc.* **2018**, *165*, F342.

2. Yoshitaka Aoki, SeongWoo Jeong, Chunyu Zhu and Hiroki Habazaki, “Origins of High Power Outputs in Hydrogen Permeable Metal-Support Fuel Cells” *ECS Transactions* **2019**, *91*, 917.

3. Yoshitaka Aoki, Shinichi Nishimura, SeongWoo Jeong, Sho Kitano and Hiroki Habazaki, “Development of Hydrogen-Permeable Metal Support Electrolysis Cells” *ACS Appl. Energy Mater.* accepted.

Awards

1. 平成 29 年 3 月：電気化学会第 84 回大会，ポスター賞

2. 平成 31 年 3 月：北海道大学物質化学部門，大塚博先生記念賞

3. 令和 元年 6 月：The 22nd International Conference on Solid State Ionics, BEST POSTER AWARD

Acknowledgements

Foremost, I would like to express my sincere gratitude to my supervisor: Associate Professor Yoshitaka Aoki. I have received the opportunity to carry out research with him for six years in the Laboratory of Interfacial Electrochemistry. Thanks to his continuous supervision, fruitful discussion, and hearty encouragement, I could accomplish several works and finalize this thesis.

I also gratefully acknowledge my dissertation committees: Professor Hiroki Habazaki, Professor Kazuhisa Azumi and Professor Kei Murakoshi for their thoughtful reviews on this thesis and valuable discussion, which definitely helped improve the quality of the thesis.

I sincerely appreciate Professor Hiroki Habazaki, Professor Emeritus Masahiro Seo, Professor Chunyu Zhu, Professor Soo-Gil Park, and Assistant Professor Sho Kitano. Thanks to their kind help, useful advice and discussion, the present research could be accomplished.

I am genuinely grateful to Prof. Masaharu Nagayama (Research Institute for Electronic Science, Hokkaido University) and Dr. Mamoru Okamoto (Department of Mathematics), Professor Manfred Martin (RWTH Aachen University) and Mr. Fabian Draber (RWTH Aachen University) for their kind teaching of simulation and valuable discussion.

My thanks are also extended to all the members of Laboratory of Interfacial Electrochemistry who helped me and made my research life so enjoyable; Dr. Khurram Rao Shahzad, Dr. Damian Kowalski, Dr. Aikira Koyama, Dr. Katsutoshi Nakayama, Dr. Chiharu Kura, Kazumasa Kikutani, Shiki Matsuura, Kosuke Kuroda, Taisei Kobayashi, Yuto Okazaki, Ryosuke Sakashita, Ryosuke

Tomizawa, Tomoyuki Yamaguchi, Atsushi Kasuga, Yuki Sato, Kentaro Takase, Keisuke Wada, Tomohiro Inoue, Hyuna Kwon, Xiangjun Shen, Hajime Toriumi, Miku Saito, Manami Takata, Hikaru Kobayashi, Naofumi Yamada, Cheong Kim, Laras Fadillah, Ning Wang, Chunmei Tang, Ruijie Zhu, Shinichi Nishimura, Naohiro Hasuo, Tatsuyuki Takano, Junpei Ikeura, Kensuke Sakuraba, Katsuya Akimoto, Randrianasolo Falitiana, Masahiro Nishimoto, Ryota Yamamoto, Takahiro Mori, Yuta Yato, Daisuke Endo, Naoki Kamitani, Reiko Takusari, Shuya Fujita, Xiong Zetao, JaeWon Jeon, Kai Shuto, Takuya Takahashi, Mikio Nagae, Hiroya Motohashi, Hisato Matsuya, Kanae Inoue, Yoko Iwata, Yukako Yamashita, Mariko Tone and all intern students. All students and professors who met at conferences discussed my research sincerely. All members of Ambitious Leader's Program and technical staffs supported my experiments.

Special thanks are expressed to my seniors; Chiharu Kura, Kosuke Kuroda, Taisei Kobayashi, Tomoyuki Yamaguchi, Dr. Khurram Rao Shahzad, Dr. Akira Koyama and my doctoral colleagues; Yuki Sato, Hajime Toriumi, Cheong Kim, Ning Wang, Chunmei Tang, Ruijie Zhu for their kind help and useful discussion.

I would like to deeply acknowledgement the financial supports by Ambitious Leader's Program (ALP) and Japan Society for the Promotion of Science for young scientists (Grant-in-Aid for JSPS fellow) and Mistry of Education, Culture, Sports, Science and Technology (MEXT).

I would like to spend the last section on my personal gratitude to my family for their constant support.